MILLIMETER/SUBMILLIMETRE-WAVE COSMOLOGY: MM-WAVE TEST CRYOSTAT DESIGN, DEPLOYMENT AND SCUBA-2/SMA OBSERVATIONS OF THE H1549 OVERDENSE GALAXY PROTOCLUSTER

by

Colin Gordon Adam Ross

Submitted in partial fulfillment of the
requirements for the degree of
Master of Science

at

Dalhousie University
Halifax, Nova Scotia
August 2014

I dedicate this thesis to my parents Laurel and Ian, and my sisters, Molly and Heather-Anne.

Table of Contents

List of Tables

List of Figures

Abstract

This thesis is divided into four main sections. I begin by providing the reader with some context for the significance of this work by introducing the concept of millimeter/submillimetre cosmology. This is followed by an introduction to the instrumentation used at these wavelengths and the design of a laboratory based system I developed to test sensitive broadband detectors operating at 0.25K. Next I will discuss a promising experiment in this field that is currently observing the cosmic microwave background in the Chilean Andes in search of a unique polarization pattern predicted by inflationary theories. In this section I will outline my contributions to the project and explain how it initiated the development of the system discussed in the previous section. I will conclude with a high-level data analysis project I worked on to gain some experience dealing with data sets from millimeter/submillimetre wavelengths.

List of Abbreviations and Symbols Used

CMB: Cosmic Microwave Background

SMG: Submillimetre Galaxy

ISM: Interstellar Medium

SFR: Star Formation Rate

TES: Transition Edge Sensor

MKID: Microwave kinetic inductance array

FIRAS: Far-infrared Spectrometer

DMR: Differential Microwave Radiometer

COBE: Cosmic Background Explorer

WMAP: Wilkinson Microwave Anisotropy Probe

ACT: Atacama Cosmology Telescope

SPT: South Pole Telescope

SCUBA: Submillimetre Common-User Bolometer Array

JCMT: James Clerk Maxwell Telescope

LRIS: Low Resolution Imaging Spectrograph

PdBI: Plateau de Bure Interferometer

ALMA: Atacama Large Millimeter Array

SQUID: Superconducting Quantum Interference Device

POLARBEAR: The Polarbear Experiment

OFHC: Oxygen-Free High Thermal Conductivity Copper

PTC: Pusle Tube Cooler

MLI: Multi-layer Insulation

RRR: Residual Resistance Ratio

RTD: Resistance Temperature Detector

PWV: Perceptible Water Vapor

HWP: Half-Wave Plate

FWHM: full-width half maximum

FOV: Field-Of-View

HTT: Huan Tran Telescope

ΛCDM: Lambda Cold Dark Matter

SMA: The Submillimetre Array

SED: Spectral Energy Distribution

CO: Carbon monoxide

H_2: Hydrogen

$^4\mathrm{He}$: Helium-4

$L_\odot$: Luminosity of the sun

$M_\odot$: Mass of the sun

σ: Stefan-Boltzmann constant

Acknowledgements

I would like to begin by thanking my supervisor, Dr. Scott Chapman, for welcoming me as the first member of his group at Dalhousie University and introducing me to the field of experimental cosmology. The support and knowledge you have provided me with over the past few years are invaluable.

I also want to acknowledge all of the support provided by other members of the group, including fellow graduate students, postdoctoral fellows and summer students. Alexey Tikhomirov, you taught me many essential skills and how to be resourceful in the lab. Kevin Lacaille, your willingness to lend a helping hand and advice whenever it was needed with the cryostat is greatly appreciated.

A lot of this work was carried out in response to our involvement in the Polarbear experiment. The resources and support provided by the members of this project have enabled our group at Dalhousie to grow and become part of a very exciting and promising international collaboration. I would like to especially thank our collaborators at the University of California Berkeley (UBC) who have gone above and beyond to welcome me into this project and for the knowledge they continue to provide me with. Michael Myers, Zigmund Kermish, Kam Arnold, Bryan Steinbach and Toki Suzuki , one of you always manage to answer one of my many questions and I cant thank you enough for this.

Lastly, I would like to thank my family, without whom, none of this would have been possible. Their continual support and encouragement enabled me to accomplish this thesis.

Chapter 1

Introduction

1.1 Millimetre and Submillimetre Radiation

Observations taken at submillimetre/millimetre (submm) wavelengths allowed scientists to begin probing the origin of our universe. This portion of the electromagnetic spectrum, ranging from 200 um to 10 mm, lies between the radio and infrared (IR) frequency bands. The two primary sources of emissions with a cosmic origin at these wavelengths are the cosmic microwave background (CMB) and submillimetre galaxies (SMGs).

Emissions from these sources can be categorized as continuum emission or spectral line emission. Each one provides unique, but complimentary information. The two most prominent sources of continuum emission are thermal emission from dust residing in the interstellar medium (ISM) and from the CMB.

Dust emission is important as a tracer of interstellar dust mass and serves as an indicator of star formation. The temperature of dust particles in the ISM increases as heat sources, in close proximity, cause them to emit thermal radiation. The wavelength at which the particles emit radiation is sufficiently long that it is optically thin. Thus, the observed signal strength is a function of both the column density and temperature of the dust, making it an ideal tracer of mass in the ISM. Furthermore, regions of intense star formation typically occur in dust-rich environments. As a result, the ultraviolet and optical emissions given off during the star formation process are absorbed and re-emitted as thermal emission by the dust at submm wavelengths. These dense regions represent the earliest signs of galaxy formation and are the high-redshift predecessors to the galaxies in our local universe. The thermal dust emission in this case acts as a measure of the star formation rate (SFR) in the galaxies. In addition to thermal dust emission, continuum emission produced by the CMB traces the conditions in the early universe through small-scale fluctuations in the primordial photon-baryon fluid.

Spectral line emission results from the transition of molecular or atomic gas between energy states. Observing the transitions with rest frame wavelengths in the submm band

provides information about the environment in which vigorous star formation is occurring. Interstellar dust does not absorb the spectral line emission and thus provides a unique window into the core of these heavily enshrouded regions. A strong relationship between the gas content of a galaxy and its star formation rate exists, and since the gas content does not evolve with time, information regarding galaxy formation and evolution at high redshift can be gathered [116, 14, 63, 20]. A key benefit of using this type of emission over continuum emission is that the spectral resolution of line measurements precisely maps the distribution of velocities along a given line of sight. This information is then used to probe both the dynamics and kinematics of the gas contained within the galaxy or galaxy cluster.

Observations at these frequencies were historically limited by a combination of instrument sensitivity and the presence of atmospheric water vapor. However, recent advances in detector technology and the use of high-altitude observation sites have enabled data collection with a quality approaching that of measurements made in the optical range. Radiation at these wavelengths originated from some of the coldest and distant regions of our universe. Measuring this radiation required a new type of specialized receiver to be designed. The main technical challenge for the new measurement instrument was to develop a hybrid sensor (or detector) that incorporated both coherent optical detector technology and incoherent radio-wave detector technology. Current advancements include the use of large arrays of cryogenically cooled transition edge sensor (TES) bolometers and microwave kinetic inductance arrays (MKIDs) (e.g. [79, 27, 58]).

1.2 The Cosmic Microwave Background

1.2.1 Introduction

The CMB is an isotropic bath of thermal radiation believed to have originated in the hot, dense early universe. Often referred to as a relic of the Big Bang, the CMB is the most distant source of observable radiation. Given that light travels with a finite speed, the light we view from distant objects must have originated from an earlier epoch. Therefore, the CMB contains many details pertaining to the origin of the universe and its evolution. For this reason, scientists have devoted much time and resources developing a detailed characterization of the CMB.

In 1965, Arno Penzias and Robert Wilson unintentionally discovered the CMB using a

radio antenna at Bell Laboratories. Following this initial discovery, the CMB was studied using the far-infrared spectrometer (FIRAS) [39] and differential microwave radiometer (DMR) [11] on the Cosmic Background Explorer (COBE) satellite. Measurements from these instruments confirmed the blackbody nature of the CMB, with a peak temperature of 2.725K, and demonstrated the first signs of a deviation from isotropy. This work was then expanded on with the Wilkinson Microwave Anisotropy Probe (WMAP), which produced the first high-resolution map of the microwave sky.

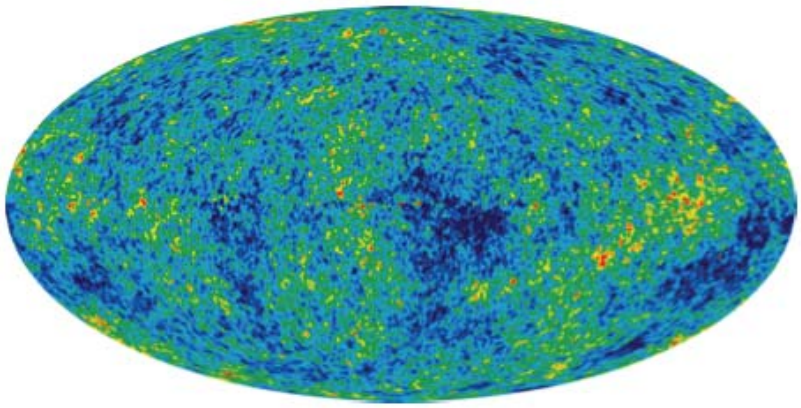

Figure 1.1: Map of anisotropies in the microwave sky taken with WMAP. Image from NASA / The WMAP Science Team

1.2.2 Brief History of the Universe

Standard Model of Cosmology

Currently, the most widely accepted framework used to explain the origin and evolution of the universe is the ”Big Bang” theory [90]. This theory states that the universe evolved from an initially hot and dense state, approximately 13.7 billion years ago. Mathematically it is represented as a singularity in which both the energy density and temperature of the universe were infinitely large, while its spatial extent was infinitely small. This initial state was followed by a subsequent period of expansion and cooling.

Although there are several theories that explain the origin and evolution of the universe, the Big Bang is the one most consistent with observation. Specifically, the following fundamental observations support the idea of a hot Big Bang:

- On large scales the universe is both isotropic and homogenous. In this context,

isotropic refers to the fact that there are no preferred directions in the universe, while homogenous refers to the fact that there are no preferred locations. This is true for scales of approximately 100 megaparsecs (MPc = $3.08 \times 10^{22} m$) and greater.

- Galaxies show a redshift proportional to their distance from the observer. This becomes evident when comparing a particular absorption line from a galaxys spectrum with a similar measurement done in a laboratory. In general, the absorption line of the galaxy shifts to a longer wavelength (i.e. it is redshifted). This result is expected in an expanding universe.

- There is a diversity of particles and an abundance of elements in the universe. To differentiate among the various components that make up the universe, it is necessary to study the elementary particles of which they are composed. The most important particles and elements are protons, neutrons, electrons, neutrinos, photons and dark matter. Since the mass of a proton is significantly higher than that of an electron, the collection of ions, atoms and molecules are commonly referred to as the universes baryonic matter.

- There exists a uniform background radiation, which theory predicts is a result of the universe being in an initially hot and dense state. This enables the Big Bang theory to supersede the idea of a steady state or static universe.

As with many theories, observations do exist that cannot be explained using a single solution. Specific to the Big Bang theory are the flatness and horizon problems. The flatness problem reflects the fact that observations suggest the universe has a flat geometry. For this to be true, the density of matter in the universe must be at a critical value to balance the ongoing expansion. Since current observations suggest a matter density in close proximity to the critical value, the value must have been even closer in the past. However, the Big Bang theory lacks an explanation as to why this should be true.

The horizon problem results from the finite speed at which photons can travel. Imagine two regions in opposite positions in the sky, each located at the maximum viewing distance (i.e. the horizon) from a central observer. In this case, the different regions cannot exchange information since the distance between them will be too large (i.e. there is no overlap between the respective horizons). However, all evidence indicates that the CMB

is homogeneous and isotropic to 1 part in 10^5, suggesting all regions of the universe were once in causal contact. Given the current age of the universe, this should not be the case.

Inflation

Inflationary theory addressed the fundamental problems of the Big Bang theory by proposing that the universe underwent a brief period of exponential growth 10^{-36} seconds after the Big Bang. This rapid expansion, which caused the universe to grow by a factor of 10^6, solved the horizon problem by allowing all regions of the universe to originate in a state of causal contact. Inflation drove these regions to sufficiently large scales such that they can no longer interact and in the process, forced any curvature in space-time to zero.

Inflation also plays a key role in structure formation by taking the primordial quantum-scale fluctuations in the universe and stretching them to cosmic scales capable of growing through gravitational instability. Today, these fluctuations are referred to as anisotropies, and can be observed as variations in the intensity (or temperature) of the CMB at a level of 1 part in 10^5. This will be discussed further in section 1.2.3.

Recombination and Decoupling

As the universe expanded and cooled, it was subjected to many transitions. Those which significantly affected the CMB occurred over a relatively short period of time after the proposed Big Bang. The important events can be summarized by three distinct historical epochs. In its initial hot and dense state, the thermal energy of the universe was such that electrons could not bind to nuclei to form neutral atoms. During this highly ionized state, electrons and photons interacted through Thomson scattering, creating a thermal equilibrium between the baryonic matter and radiation component of the universe. The effect of this interaction was to smooth any inhomogeneities in the density distribution, thus inhibiting the growth of structure through gravitational instability.

Approximately 240000 years after the Big Bang, the temperature of the universe cooled to 3740 K. This time is referred to as ”recombination” and signifies a transition in the photon-baryon fluid from an ionized state to neutral state. As the universe continued to expand and cool, the distance that a photon could travel before interacting with an electron increased. Eventually the expansion rate of the universe exceeded the interaction rate and the photons decoupled from matter, a process referred to as ”photon decoupling.” When this

happened, the universe transitioned from being opaque to transparent for photons, and the CMB was produced. Shortly after, the average photon underwent its final interaction with the remaining free electrons and was able to stream unimpeded through space, forming the last scattering surface.

1.2.3 Temperature Fluctuations (Anisotropies)

The universe we observe today appears to be homogeneous and isotropic on large scales. However, given that matter has organized into structures, such as galaxies and galaxy clusters, proves that inhomogeneities do exist. Measurements from COBE were the first to show this, detecting small fluctuations in the temperature of the CMB at a level of 1 part in 10^5. These fluctuations in temperature, or anisotropies, are believed to be the seeds for the large-scale structures observed today.

Anisotropies in the CMB occur on both large (i.e. greater than the horizon distance) and small (i.e. less than the horizon distance) scales. The large-scale anisotropies are characteristic of the primordial fluctuations themselves since there has not been sufficient time for the process of structure formation to take place. In contrast, the physical scale of the smaller fluctuations appears to correspond well with the structure we see today.

These small-scale variations in the temperature of the CMB are believed to be a result of quantum fluctuations in the primordial photon-baryon fluid that were projected onto the CMB at recombination. At this point, perturbations in the density of matter would acted to modify the gravitational potential, causing photons originating from higher density regions to lose energy as they attempted to overcome the associated potential well. This effect gives rise to relatively warmer and colder spots on the CMB, corresponding to lower and higher density regions respectively.

1.2.4 Gravitational Lensing

While precise measurements of the CMB anisotropies with the Wilkinson Microwave Anisotropy Probe (WMAP), Atacama Cosmology Telescope (ACT), South Pole Telescope (SPT) and Plank ([98, 62, 86, 106]) have provided great insight into the evolution and composition of the Universe, a wealth of information remains undiscovered in the CMB. By studying the primordial fluctuations in both temperature and polarization it is possible to gain information about the properties of the Universe from the initial Big Bang until the photons

decoupled from matter. However, these photons do not simply stream through the Universe unaffected by their surroundings. Instead, they are subjected to the gravitational influence of objects (e.g. galaxies, galaxy clusters, and dark matter) that they pass in proximity to - a process called gravitational lensing.

Gravitational lensing is the process whereby the trajectory of light from a background source will be perturbed by the presence of a massive object. The light emitted from a background source, for example a bright quasar or the CMB, can be used to illuminate objects such as galaxies and galaxy clusters between the source and the observer. Einstein's theory of general relativity predicts that mass will bend light, a process that is analogous to the refraction of light by an optical lens. However, rather than using a piece of glass to re-focus the light, gravitational lensing occurs through an interaction of light with the gravitational field produced by a massive object. Light passing by the object will be deflected by the gravitational potential of the mass and can be bent into the field of view of the observer, allowing for detections that would otherwise be impossible. Structures of all scales can be subject to this process, ranging from individual galaxies at the small scale to clusters of galaxies at the large-scale. The degree of lensing is a function of the relative position of the source, lens and observer, as well as the total mass and shape of the effective lens. The effect is typically categorized as either strong, weak or microlensing depending on the geometry of the situation.

As a result of being sensitive to interactions with the intervening mass, gravitational lensing provides a useful tool for studying the properties of structure on different scales. It has enabled cosmologists, who are interested in studying the large-scale structure, to gain insight into the distribution of mass in the universe, including dark matter. This is because dark matter makes up the vast majority of the total mass of the universe, causing it to be the dominant contributor to lensing on the largest scales. An example of this effect can be observed in the famous image of the Abell 2218 cluster taken by the Hubble Space Telescope. The distortions in this optical image are evident for individual galaxies, manifesting themselves as pronounced arcs that represent the influence of strong gravitational lensing. Unfortunately the Abell cluster represents a rare find and cosmologists seek to map the mass distribution over the entire sky, the majority of which experiences weak gravitational lensing. In this regime, the overall effect on the source image will be a stretching (shearing) and magnification (convergence). Since the lensing will not be strong enough to produce a

characteristic signature that is visible by eye, it is necessary to use source statistics to gain information about the intervening structure.

Studies of weak gravitational lensing that use the CMB as a background source provide a unique window into the universe. The CMB is well characterized and is advantageous when focusing on the statistical reconstruction (estimation) of the average properties of the large scale structure. Furthermore, it is the most distant background source available, enabling the opportunity to probe the large-scale mass distribution out to high redshift. As a result, the deflection signal will be from the interaction with structures that span a variety of cosmic epochs and contain insight into the growth of structure and geometry of the Universe. These measurements are highly desirable since they will provide constraints on the properties of dark matter, neutrino masses and through cross-correlations, the relationship between dark matter and its luminous tracers.

Gravitational lensing measurements of the CMB temperature anisotropies have been well characterized through initial detections in cross-correlations with tracers of the large-scale matter distribution and through auto-correlations of the temperature maps [1, 46]. However, the CMB is approximated by a Gaussian random field and therefore lacks the presence of any distinct features. Fortunately, there exist several statistical methods to extract the intervening mass distribution from the lensed CMB power spectrum. The effect of lensing is to re-map the intrinsic temperature fluctuations (i.e. cause a distortion) in the CMB. This process will conserve the total surface brightness, but redistribute the power in a way that smoothes the peaks in the temperature spectrum on small spatial scales. Although these measurements provide a basis for constraining cosmological models, lensing of the CMB polarization can provide a more precise, higher resolution mapping of the mass distribution. This is because polarization measurements do not suffer from the effect of random primordial fluctuations (i.e. cosmic variance), which can appear as gravitational lensing in the temperature anisotropies.

The effect of gravitational lensing on the unlensed CMB polarization spectrum is the conversion of power due to the E-mode polarization into a non-zero B-mode component. It is important to note that this process will occur in the absence of the tensor-generated B-mode signal predicted to have resulted from gravitational waves and is purely the result of converting the scalar-generated modes.

Consider a photon that travels in a direction defined by the vector $\hat{\mathbf{n}} + d(\hat{\mathbf{n}})$ in the

absence of gravitational lensing. The effect of interactions with the intervening matter density will perturb the photon from this initial trajectory , causing it to have a new position on the sky defined by $\hat{\mathbf{n}}$. The result will be a remapping of the primordial temperature and polarization fields. Therefore, given an unlensed Gaussian temperature field $\tilde{T}(\hat{\mathbf{n}})$ and polarization field with Stokes parameters $\tilde{Q}(\hat{\mathbf{n}})$ and $\tilde{U}(\hat{\mathbf{n}})$, the lensed fields will be:

$$T(\hat{\mathbf{n}}) = \tilde{T}(\hat{\mathbf{n}} + d(\hat{\mathbf{n}})) \tag{1.1}$$

$$(Q \pm iU)(\hat{\mathbf{n}}) = (\tilde{Q} \pm i\tilde{U})(\hat{\mathbf{n}} + d(\hat{\mathbf{n}})) \tag{1.2}$$

where $T(\hat{\mathbf{n}})$, $Q(\hat{\mathbf{n}})$, and $U(\hat{\mathbf{n}})$ are the observed fields and $d(\hat{\mathbf{n}})$ is the lensing deflection field. Note that these observed fields will contain all sources of error including detector noise and foreground contamination.The CMB polarization defined in equation 1.2 can be decomposed in the scalar E-mode and tensor B-mode components. Similarly, it is possible to express the fields in terms of the deflection angle as follows:

$$T(\hat{\mathbf{n}}) = \tilde{T}(\hat{\mathbf{n}} + \nabla\phi) \tag{1.3}$$

$$Q(\hat{\mathbf{n}}) = \tilde{Q}(\hat{\mathbf{n}} + \nabla\phi) \tag{1.4}$$

$$U(\hat{\mathbf{n}}) = \tilde{U}(\hat{\mathbf{n}} + \nabla\phi) \tag{1.5}$$

where $\nabla\phi$ is the deflection potential and $\hat{\mathbf{n}}$ denotes the angular position of the photon on the sky. Both implementations assume the flat sky approximation and are therefore only valid for small angular scales.

A common technique used to characterize the effect of gravitational lensing is to begin by Taylor expanding equation 1.2 to first order in the deflection angle to approximate the polarization field. Data then undergo a Fourier transform to be represented in a more convenient coordinate system. The effect of re-mapping the polarization field can then be seen in Fourier space as an induced correlation between the E and B modes.

The Taylor expansion reveals that the off-diagonal elements of the two-point correlation functions of E- and B-modes are proportional to the lensing deflection field, $d(\hat{\mathbf{n}})$. Quadratic estimators take advantage of this feature to measure CMB lensing [2]. The two lensing quadratic estimators for CMB polarization are:

$$d_{EE}(\mathbf{L}) = \frac{A_{EE}(L)}{L} \int \frac{d^2\mathbf{l}}{(2\pi)^2} E(\mathbf{l}) E(\mathbf{l}') \frac{\tilde{C}_l^{EE} \mathbf{L} \cdot \mathbf{l}}{C_l^{EE} C_{l'}^{EE}} \cos 2\phi_{\mathbf{ll}'} \tag{1.6}$$

$$d_{EB}(\mathbf{L}) = \frac{A_{EB}(L)}{L} \int \frac{d^2\mathbf{l}}{(2\pi)^2} E(\mathbf{l}) B(\mathbf{l}') \frac{\tilde{C}_l^{EE} \mathbf{L} \cdot \mathbf{l}}{C_l^{EE} C_{l'}^{BB}} \sin 2\phi_{\mathbf{ll}'} \tag{1.7}$$

In equations 1.6 and 1.7, $\mathbf{l}$,$\mathbf{l}'$, and $\mathbf{L}$ are coordinates in Fourier space with $\mathbf{L} = \mathbf{l} + \mathbf{l}'$. The angular separation between $\mathbf{l}$ and $\mathbf{l}'$ is $\phi_{\mathbf{ll}'}$, $\tilde{C}_l^{EE}$ is the theoretical primordial power spectrum, C_l^{EE} and C_l^{BB} are theoretical lensed power spectra. The estimators are normalized by $A_{EE}(L)$ and $A_{EB}(L)$ so that they recover the input deflection power spectrum [2].

1.3 Submillimetre Galaxies

1.3.1 Introduction

The advent of sensitive mm-wave detector technology has facilitated the discovery of a population of ultra-luminous, dust obscured, star forming galaxies at high-redshift (e.g., [95, 51, 7]). The bulk of the energetic output from these galaxies is emitted at observed frame sub-mm wavelengths, and therefore the galaxies are referred to as sub-millimeter galaxies. Due to the dust obscuration, detection of these galaxies in wavebands other than the mm/submm region has proven to be difficult. Follow-up studies using optical and UV emission suffer from a significant loss in signal strength due to attenuation by the dust. For this reason, it has been necessary to study SMGs directly at mm/sub-mm wavelengths where molecular emission features are emitted. Information gathered at these wavelengths will enable us to gain a detailed understanding of SMG properties, and begin to assemble an unbiased view of the population over their entire redshift range.

The redshift distribution of these galaxies appears to peak at $z \sim 2.2$ [23, 115], however, these estimates were based on a sub-population of SMGs that were clearly identified at radio and mid-infrared wavelengths. The intermediate step of identifying the SMGs at other wavelengths was necessary for these studies to pinpoint the specific location of the emission and to search for redshifts. This step resulted in uncertainty in the measurement, with a substantial ($\sim 35\%$) fraction of the population having to be removed from the sample (and, regrettably, the fraction likely to be at higher redshifts). These authors attempted to

estimate the redshifts of this missing 35% of the SMGs through various indirect means, and concluded the SMG population, in total, likely peaked at $z \sim 2.5$. [23, 115]

The most recent studies using gravitational lensing to boost signals, and for the first time obtaining complete identifications of the SMGs directly at sub-mm wavelengths, have revealed a high redshift tail extending out to $z = 6.34$ [83], and a peak redshift $z \sim 3.3$ ([96, 112], significantly higher than previously suggested. The strong molecular line transitions have enabled redshifts to be measured with close to 100% completeness in these studies.

SMGs have extreme far-infrared luminosities, 10^{12}-10^{13} the luminosity of the sun ($L_\odot$) integrated from $8 - 1100\ \mu m$, translating to SFRs on the order of $\sim 10^3$ solar masses ($M_\odot$) per year [18]. Since their stellar masses are not particularly large ($\sim 7 \times 10^{10} M_\odot$, [45]), this implies that they generally lie significantly above the main sequence of star forming galaxies, which have SFRs of $\sim 100 M_\odot/yr$ at similar stellar masses to the SMGs. The high SFRs of SMGs are most naturally explained as a result of merger-driven bursts in the early universe ([75]), and account for a significant portion of the integrated extragalactic background energy.

The relationship between high SFRs and large molecular gas reservoirs [18] are consistent with the findings that these galaxies reside in the most massive dark matter halos in the early Universe [15, 47], and are likely the progenitors of massive elliptical-galaxies in our local Universe. Characterization of this luminous sub-millimeter galaxy population has revolutionized our understanding of galaxy formation and evolution and has led to tight constraints on the models that attempt to simulate these processes (e.g., [9]).

1.3.2 Survey Logistics

Until recently, surveys conducted to measure the molecular line emission properties of the ISM have been both time intensive and biased towards lower redshift galaxies. This is a result of the three-step process by which the spectra were obtained. First, the sky needed to be mapped in the mm waveband using instruments such as the Submillimetre Common-User Bolometer Array (SCUBA) camera on the James Clerk Maxwell Telescope (JCMT) [49], or the South Pole Telescope (SPT) [86] to detect potential sources of high luminosity. Second, the redshift was obtained from optical data (e.g. from the low resolution imaging spectrograph LRIS on the Keck-1 telescope [78]). However, the optical data suffered from

extinction due to the enshrouding dust intrinsic to star-forming regions and cosmological dimming, making the sampled redshift distribution biased towards lower redshift objects. Third, spectroscopic follow-up was performed on the sources using an interferometer such as the Plateau de Bure Interferometer (PdBI) in France [44] or the Atacama Large Millimeter Array (ALMA) [117].

1.3.3 Importance of the submillimetre galaxies

Since star formation is driven by the collapse of cold molecular dust clouds, it is possible to gain insight into active star-forming regions by observing of the physical and chemical state of the ISM. The detection of molecular gas properties at high redshift provides an excellent probe of the stellar processes occurring within a galaxy, revealing information about the metallicity, temperature and density distribution and the dynamic processes occurring within the ISM. These properties can be combined with other observations as an indirect means to infer the SFR and, therefore further constrain models of galaxy formation and evolution.

Of particular interest is the rotational transition of certain molecules in the ISM, since the resulting spectral line features provide the most direct diagnostic tool to gain insight into molecular gas properties and hence star formation. They are the most direct, in that they do not suffer from dust obscuration, cosmological dimming and source confusion problems that are intrinsic to UV/optical observations. Spectral line features from molecules also provide a more direct probe of galactic dynamics, since kinematic line profiles vary between different galaxies.

The most commonly studied rotational transition is that of carbon monoxide since it manifests as a prominent spectral feature in the mm waveband. Carbon monoxide (CO) is important because it is produced under similar conditions to molecular hydrogen and is thermally equilibrated with it through collisions, making it an excellent tracer of star formation. Since molecular hydrogen lacks a permanent electric dipole moment and therefore does not produce a spectral line feature, it is necessary to use an alternate tracer.

The most important feature in rotational transition diagnostics is the emission line intensity, defined as the integral over the spectral line width in a preferred coordinate space. The line intensity is a measure of how many molecules are in a given rotational state. Therefore the summation of intensity over all observable transitions will provide a measure of the

total number of molecules along the line of sight. Thus, when combined with optical data (i.e. how optically thick the cloud is), it is possible to infer the total molecular gas mass based on an excitation model describing the distribution of molecules amongst different rotational states. In the case of CO, it is possible to deduce the mass of the underlying molecular hydrogen reservoir and hence the amount of fuel available for star formation, when the relative amount of CO to H_2 is known. The combination of this gas information coupled with far-IR luminosities allows the star formation efficiency to be calculated and facilitates comparisons of these high SFR rate galaxies with normal galaxies at similar redshifts.

Since the emission line intensity provides an estimate of the distribution of molecules throughout the different rotational states, it also provides information about the temperature and density distribution of the molecular gas.

The density of a gas can be inferred from a comparison of a molecules half-life (the characteristic timescale for spontaneous decay from an excited state to the next lowest energy state) with the inter-molecular interaction timescale. For a dense gas, the timescale on which molecules interact will be much faster than in a cold gas, making the relative number of collisional excitations to spontaneous decay events larger. This means that molecules in a cold gas will tend to occupy only lower energy states, while the molecules in a warm gas will tend to occupy a higher number of states.

The temperature of gas is a measure of the random motions of the molecules that constitute the gas. Warm gas will tend to have molecules that move around and interact at a greater rate than colder gas, thus making excitation by collisions between the molecules much more likely. Therefore, warmer gases will tend to occupy higher energy states than the colder gas. By examining the intensity ratio of two unique spectral lines, it is possible to infer a measurement of the related gas temperature. More specifically, we are measuring an apparent temperature referred to as the excitation temperature, which was previously discussed.

However, confusion can result from this process since it is not immediately evident whether a low number of molecules populating higher energy states can be attributed to a low gas temperature or low density. This can be partially resolved by considering excitation temperature as a function of rotational transition. For a given density, measuring various transitions will result in multiple excitation temperatures.

In order to obtain a complete understanding of the temperature and density distribution in a molecular gas cloud, it is necessary to analyze multiple transitional excitations. Fortunately, CO has many observable transitions over different excitation temperatures. The most commonly studied of these transitions are the $J = 2 \rightarrow 1$ and $J = 1 \rightarrow 0$ transitions with excitation temperatures of 5.5K and 16.6K, respectively [10]. However, these transitions only probe the colder outer regions of the molecular dust cloud, making it necessary to move to higher transitions to probe the warmer/denser central regions where active star formation is occurring. These higher transition observations were historically limited by receiver technology, the most important of which was the limited receiver bandwidth. With the advent of higher bandwidth receivers that use a bandwidth synthesis strategy, observations of the $J = 3 \rightarrow 2$, $J = 4 \rightarrow 3$ and $J = 5 \rightarrow 6$ transition, with corresponding excitation temperatures of 33K, 55K and 116K have been possible [10].

The linewidth of a spectral feature, usually taken to be the full width at half maximum (FWHM) provides an excellent estimate of the dynamical mass of galaxies, free from the uncertainties present in the optical and UV wavebands. These uncertainties include dust obscuration and non-gravitational effects. For example, consider imaging a galaxy in the optical waveband. In the areas where significant molecular dust clouds are present (and likely the regions of highest star formation) the signal is greatly attenuated and this region appears dark. However, star-forming regions with lower molecular gas concentrations will still be present and may be interpreted as the entire population. This can lead to a false representation of the total SFR and motion of the galaxy. Also, although highly unlikely, it is possible to observe two line profiles with the same intensity (i.e. same area under the line), but with significantly different line widths. Therefore it is necessary to analyze both line intensity and width to understand the system's properties.

Another important feature that arises when probing the submm region of the spectrum is the negative k-correction as the source redshift increases [**?**]. As a result, the cosmological dimming is compensated by the rising dust spectrum as the source redshift increases (Figure 1.2).

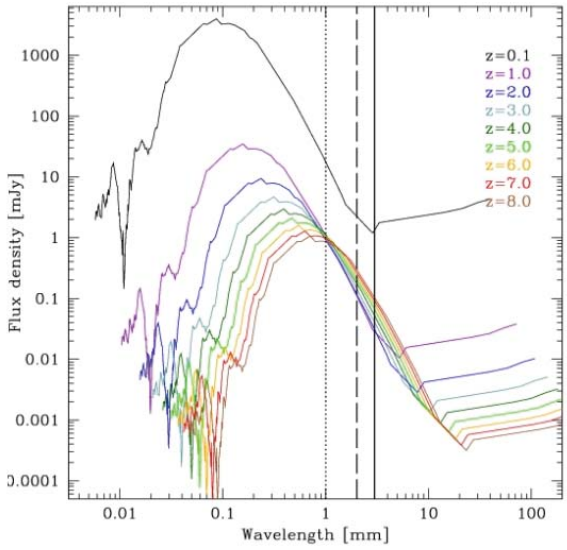

Figure 1.2: This figure shows a plot of flux density versus wavelength for a single source (Arp220), as it would appear at different redshifts. The negative k-correction is a result of the positive slope in the mm-waveband and results in a higher observed flux as redshift increases. Cosmological dimming results from both geometric and surface brightness dimming effects, the latter of which can be ignored due to the increase in observed flux. Therefore as redshift increases, shifting the entire spectrum to the right, the geometrical component of cosmological dimming, which is inversely proportional to luminosity distance squared, will tend to shift the spectrum down. The result is a region of the spectrum located in the mm-waveband that remains unaffected by redshift over a certain range ($z \sim 2-8$). This allows the elimination of the intermediate step of determining redshift based on optical observations and is free from the bias towards lower redshift objects that is intrinsic to optical data.

Chapter 2

Millimeter Wave Instrumentation and Test Cryostat Design

2.1 Introduction

Observational astronomy and cosmology requires specialized imaging technology, used in the world's most remote locations, to detect signals that range over several orders of magnitude in energy. Researchers in these fields are continually developing sensor technology in order to detect the faintest of signals. To achieve the unprecedented sensitivity that is necessary in current experiments, the sensor and associated low-level signal-processing electronics must be cryogenically cooled to well below room temperature. This practice has long been used for infrared (IR) sensors, which detect the heat radiated from objects, so that the heat from the instrument itself does not overload the detector. Examples of this technology include military applications such as night-vision goggles, IR sensors for atmospheric science and IR telescopes. Recent experiments attempt to detect the extremely faint gravitational wave signal that is expected to reside within the polarization pattern of the CMB by using cryogenically cooled receivers to achieve a background-noise-limited instrument (i.e. for ground-based experiments, the statistical fluctuation in the arrival rate of photons due to the atmospheric foreground dominates the instrument noise) [86, 6, 61, 80, 87, 59].

The receivers used in these types of experiments operate over two distinct temperature ranges, above and below 4K. Large arrays of superconducting transition edge sensor (TES) bolometers are lowered to their transition temperature of sub-Kelvin magnitude using a closed-cycle three-stage helium sorption refrigerator [13]. At this point a small change in temperature will result in a large change in electrical resistance and the detector sensitivity will be maximized. The readout electronics operate at slightly warmer temperatures and use superconducting quantum interference devices (SQUIDs) above 4 K to amplify the faint electrical signal. This thesis presents the initial design and testing of a laboratory-based cryostat that uses commercially available closed-cycle mechanical cryocoolers to achieve the cryogenic environment necessary to test TES bolometers for the Polarbear experiment.

2.2 Background

As a context for this project, it is useful to briefly review cryogenic technology and the techniques commonly employed at low temperatures. The term cryogenics refers to the study of low-temperature physics. In particular, it is the study of how to produce low temperatures and how materials and systems behave when they are cooled to a certain temperature regime. The temperature range can vary depending on the study objectives; however, for the purposes of this work, it refers to systems operating at 77 K and below, with a specific emphasis on the temperature regime of 4.2 K and below.

As the base temperature at which an experiment is conducted decreases, the complexity of the system and the physics involved increases, rendering even the simplest experiments difficult. The aforementioned temperatures of 77 K and 4.2 K refer to the boiling point of nitrogen and helium, respectively. Nitrogen and helium are the most widely used cryogens in low temperature experiments. Although nitrogen is commonly used, the focus in this work is on helium, as it is the primary cryogen used in systems operating at 4.2 K and below. Helium is available in two isotopes, $^4\mathrm{He}$ and $^3\mathrm{He}$, and when used in conjunction with each other can provide base temperatures below 1 K. $^4\mathrm{He}$ is the more commonly used of the two isotopes, since it occurs naturally through the decay of alpha particles. $^3\mathrm{He}$ is required to achieve sub-Kelvin temperatures, but unfortunately, it does not occur in nature and is a by-product of tritium decay, making it expensive to purchase. For this reason, $^3\mathrm{He}$ is much less common and care must be taken to maximize its use by recycling it in an experiment.

The first step in any low-temperature experiment is to provide a physical environment in which the necessary temperature range can be achieved and maintained for a given period of time. Reaching this objective requires managing the transfer of heat at cryogenic temperatures. This includes an efficient supply of cooling power via thermal links and mitigation of heat loading from warmer components. Heat transfer can occur by means of conduction, convection and radiation. Each method of heat transfer can play a unique role in developing a cryogenic experiment and the relative contributions will depend on the nature of the experiment. For example, heat by conduction can be reduced between different temperature elements by evacuating the space between them. In this case, the dominant transfer of heat is by thermal radiation. Conversely, one can increase the thermal conductivity by introducing a conductive gas and reestablish this as the primary means of

heat transfer.

Physically, heat transfer by conduction is accomplished by molecular agitation of a material subject to a temperature gradient. It requires a medium for the energy to flow through and thus can only occur through a solid, liquid or gas, or between two materials in contact with each other. In each case, energy is transferred from the warmer (higher energy) region to the cooler (lower energy) region. The conductive heat flow through a solid element is defined as follows and can be found in any heat transfer textbook (e.g. [54]:

$$\frac{dq}{dt}_{cond} = \frac{A}{L}\int_{T_1}^{T_2} k(T)dT \tag{2.1}$$

Where A is the cross-sectional area, dT/dX is the temperature gradient along the element, L is the length of the element and $k(T)$ is the temperature dependent thermal conductivity intrinsic to the material. Values of thermal conductivity vary greatly between different materials. Materials with high thermal conductivity values are an appropriate choice for creating a thermal pathway, while materials with a low value are used as thermal insulators. There is generally a predictable relationship between the thermal conductivity of a particular material and temperature. However, this relationship is affected by the grade of the material. It is not until a high-purity metal is at a low-temperature that this effect is evident, resulting in conductivity values that vary significantly depending on the amount of impurities in the metal. Since it is quite difficult to measure the thermal conductivity directly under such conditions, the electrical resistivity is measured instead and converted into a thermal conductivity estimate. This is discussed further in 2.3.

Heat conduction across an interface between two solid surfaces is also a critical measurement since the thermal resistance at this boundary can be a significant factor in heat transfer at low-temperatures. This has implications for the design of thermal connections and integration between the cooling system and the object being cooled, as well as thermometry installation and the necessary heat sinking of readout wiring. Since measuring the electrical resistance across this type of interface does not yield an accurate reading [**?**], it is necessary to use precision thermometry. The approach taken in this work is discussed further in 2.5.2.

The interface between two solid surfaces can be permanent or temporary. Common

choices for permanently joining two surfaces include solder, epoxy, welding or brazing. Solder joints can be accomplished using an indium solder and can yield the highest thermal conductivity among these choices. Varnish and glue joints can also result in a connection with high thermal conductivity; however, as in the case with solder joints, they represent a permanent connection and, depending on the application, may not be suitable. Temporary joining can be achieved using pressed contact joints; for example, bolting two surfaces together, and/or using a cryogenic grease or varnish.

Although pressed contact joints are more flexible, they often result in a higher thermal resistance across the interface between the two surfaces. For this reason, care must be taken when preparing the surfaces to maximize the heat transfer. Unlike the permanent solutions discussed above, where the thermal conductivity scales with the area of the interface, pressed contact joints scale linearly with the applied force between the two surfaces. There are typically three applied force regimes that are defined with respect to pure indium foil [33], which is commonly used to increase the thermal conductivity across interfacing surfaces.

The first applied force regime, defined as low-pressure contact (i.e. less than the yield strength of indium), is typically used when fastening sensitive thermometry to the test apparatus. In this case, the application of a thin coat of low-temperature grease (e.g. Apiezon Type-N [1].) on the respective surfaces can result in improved thermal conductivity across the interface. This type of grease is typically only useful above 50K and can have an opposite effect below this temperature by acting as an insulator.

The second applied force regime, defined as moderate pressure contact (i.e. greater than the yield strength of pure indium) is common when a thermal strap is attached or a radiation shield is joined to a cold plate. Improved thermal conductivity may be realized under these instances if a thin sheet ($> 0.1mm$) of pure indium foil is placed between the mating surfaces. In both the low and moderate pressure cases, the thermal conductivity is altered from its tendency to scale with applied force, to increase linearly with the surface area of the interface.

The third applied force regime, defined as high-pressure contact is achieved when sufficient pressure is applied between the surfaces, causing the thermal conductivity to once again scale with the applied force. In this case, gold plating the surface will helps prevent

[1] `http://www.apiezon.com`

the thermal conductivity from deteriorating due to oxidation and makes for a softer surface, thus improving thermal conductivity

While heat transfer by conduction and convection requires a medium to occur, heat transfer by radiation does not; it can occur in vacuum. Energy transfer by thermal radiation is accomplished through the emission of electromagnetic radiation from one body to another and is the dominant source of thermal loading in most cryostat systems that implement a multi-stage "cryogen free" approach. To mitigate this effect, these type of systems place radiation shields between the various temperature stages to intercept the heat flow. The net heat flow of thermal radiation from a warm surface to a cooler one is governed by the Stefan-Boltzmann law as follows, which can be found in any thermodynamics text book (e.g. [70]):

$$\frac{dq}{dt}_{rad} = \sigma \epsilon A (T_2^4 - T_1^4) \tag{2.2}$$

where, ϵ is the emissivity of the surface at temperature T, A is the surface area of the emitting object, and σ is the Stefan-Boltzmann constant [5.67×10^{-8} $\frac{W}{(m^2 K^4)}$]. The emissivity of a surface is directly related to its reflectivity and it is necessary to consider this when choosing the appropriate material and surface finish for a radiation shield. Commonly used materials include either stainless steel, aluminum with a polished surface, or an aluminum-coated Mylar wrap for increased reflectivity (i.e. a lower emissivity).

A cryostat is a device that experts use to create an environment in which experiments can be carried out under stable cryogenic temperatures. Due to the variation in design and application, their appearance and operation can be quite diverse. The device can range from something as simple as a conductive enclosure submersed in a liquid cryogen, to a much more complex cryogen-free system with variably cooled stages. In the latter instance, the system must be contained within a vacuum chamber to minimize conductive heat loads between the different stages. In applications where a signal must be sent into the cryostat, optical components such as windows and lenses may be necessary which will introduce further design complications. In general, cryostats can be classified as either continuous flow or closed-cycle. In a continuous flow cryostat the cryogen supply needs to be constantly replenished - a result of boiling under operational conditions. This can be quite costly and pose several constraints, especially when operating in remote environments where an accessible source may not be readily available. In contrast, a closed-cycle cryostat captures

the evaporating cryogen and recycles it back through the system.

As was previously noted, refrigeration typically occurs by either directly immersing an object into a liquid cryogen bath, or by attaching it to the cold stages of a mechanical cryocooler. Although not capable of providing as much cooling power as the direct immersion technique, mechanical cryocoolers are becoming more popular for applications in remote locations. This is due to the fact that a steady supply of liquid cryogens is not always readily available. Drawbacks still exist, however, as these systems are prone to fluctuations in base temperature and can generate both mechanical vibrations and electromagnetic interference (EMI).

In its simplest form, a mechanical cryocooler consists of an expansion chamber, a high-purity cryogen gas, a compressor, and a porous material with a high heat capacity. Cooling in this type of system occurs by continuously cycling the high-purity gas through a series of high- and low-pressure states. The cycle begins at room temperature where a gas, typically $^4\mathrm{He}$, is compressed using a piston. This causes the gas to flow through a porous material, called a regenerator. The role of the regenerator is to remove heat from the compressed (heated) gas as it flows into the expansion chamber and to maintain the temperature gradient between the warm and cold components. After the regenerator removes the heat, the piston returns to its original position, causing the gas to expand and adiabatically cool into a chamber located within the cryostat. The expansion chamber is often referred to as the system's 'cold head and serves as a thermal anchor point to remove heat from a given object. A classic example of a system that uses a piston to achieve expansion and contraction is the Gifford-McMahon type cryocooler [36]. However, this can lead to mechanical vibrations that compromise certain experiments. If this is the case, an alternative solution that uses no moving parts at the cold stage is available, namely the pulse-tube cryocooler. In the pulse-tube system the moving piston is replaced with a series of acoustic pulses that achieve the same result.

Cryogenic temperatures below 4 K (i.e. the condensation point of $^4\mathrm{He}$) are often necessary for the operation of instruments intended for astronomical applications. In some cases, sub-Kelvin temperatures are desirable. The methods by which sub-Kelvin temperatures are achieved vary depending on the required base temperature. Commonly used refrigeration techniques include adiabatic demagnetization of a paramagnetic salt [94], adiabatic nuclear demagnetization [81], $^3\mathrm{He}$-$^4\mathrm{He}$ dilution [12] and helium sorption (also referred to as

evaporative cooling) [13]. While the latter is only capable of reaching base temperatures of approximately 0.3 K, this is sufficient for most ground-based astronomy experiments. Temperatures below this are not advantageous since the experiment is limited by background radiative loading. Although more complicated, the rest of the aforementioned techniques can be used to reach base temperatures of 0.1 K [107].

2.3 Cryostat Design Goals, Challenges and Materials Selection

The main goal of this work was to create a laboratory-based system at Dalhousie University that mimics the cryogenic environment being used in the receiver on the Huan Tran Telescope (HTT) for the POLARBEAR project [The Polarbear Experiment]. This system was designed to be one of several test cryostats for TES bolometers fabricated at the University of California, Berkeley (UCB). Testing of the TES bolometers will be done post-fabrication before they are integrated into the telescope for science-grade observations. Therefore, a strict set of requirements must be followed to ensure uniform testing across the various institutions [61]. These requirements state that the system must first be able to provide a cryogenic environment capable of cooling the detectors down to a base temperature of 0.25 K for at least a 36 hour hold time. This ensures that the detectors are operational and that the thermal carrier noise is less than the expected thermal background loading noise from the atmosphere, for a duration that is sufficient to carry out useful observations. Secondly, the cryostat must be sufficiently cooled that its contribution to the overall thermal background noise, along with all of the enclosed components, remains subdominant. Under these conditions the receiver will contribute only a small portion to the overall thermal loading on the detector. Thirdly, the SQUIDs used in the amplification stage of the readout electronics must be cooled below their transition temperature of approximately 6 K. This serves to not only make the SQUIDs operational, but increases the transimpedance and gain of this component. All of these requirements are designed to minimize the noise of the instrument and to create an experiment that is background noise limited.

When designing a cryostat, it is best to begin with the internal structure used to mount the detector, and design the external components accordingly. The 6” silicon test wafer, containing approximately 1100 individual TES bolometers, currently being fabricated at UCB for the next generation of the Polarbear experiment, served as the starting point for

this work. Its relatively large size and accompanying readout electronics, dictated the overall dimensions and cryogenic cooling requirements.

Due to the continually changing and highly specialized nature of such an experiment, a commercial cryostat was not available. Therefore, it was necessary to fabricate a custom system that met the desired specifications. This involved an iterative process that began with a review of existing designs for similar systems within the collaborative network. Although similar, the existing cryostats were subject to different constraints. They did not meet the increased sizing and cooling requirements established by the next generation of test wafers, which contained an order of magnitude more detectors and readout wires than their predecessors. To incorporate these new requirements, an initial cryostat design checklist, as outlined in [33], was applied to the pre-existing design files.

The process began with four initial design considerations: (i) the operational temperature range and necessary cooling power, (ii) the amount of sensor current needed to enable the measurement, (iii) the required mechanical properties, and (iv) the sensitivity of the experiment to a given magnetic field. The most crucial experimental parameter to address was the desired base temperature. This dictated the method by which the cryostat was to be cooled and, therefore, the overall configuration. If it were possible for the experiment to be carried out using a liquid cryogen (i.e. at a fixed boiling point), the set-up could have been be greatly simplified. However, since it was necessary for the cryostat to operate over a range of temperatures in a remote environment, a mechanical cryocooler was necessary. An additional factor that required consideration was the allowable drift tolerance about the target temperature and the necessary hold time. Both of these items were determined based on the cooling power of the refrigerators in relation to the expected heat load. When calculating the required cooling power, it was important to consider the magnitude of the signal processing current. If not properly addressed in such a temperature-sensitive experiment, heat carried along the wires could have easily exceeded the cooling power of the refrigerators. This imposed strict design constraints on how to send the signal to and from the detector, requiring cryogenic wiring to be placed in thermal contact with a series of progressively cooler stages. The design solution also needed to ensure the system was portable and had easy access to the bolometer array.

Similarly, optimization of the mechanical properties of the cryostat was essential to create a balance between mechanical strength and heat transfer at low temperatures. Like

most applications, materials with dissimilar properties were used to accomplish this goal. When using materials with different properties, great care was taken to minimize the differential thermal contraction, which could have resulted in structural failure. Lastly, it was necessary to consider the magnetic field in the experimental environment and the effect of it on any critical measurements. Since this work was carried out under low-magnetic field conditions (i.e. only subjected to the earth's magnetic field), this did not influence material selection or shielding requirements. All other factors were carefully considered in the design of the system described in this work.

The general design process is outlined here, with further details presented in the following sections. Initial concepts drew from previous designs that were successfully implemented by collaborators at McGill University, UCSD and UCB, as well as KEK, the High Energy Accelerator Research Organization in Japan (e.g. [8]). Each design was unique to the requirements of the respective institutions, and reflected the years of research it took to create an environment in which the detectors, which would be implemented on the Huan Tran Telescope as part of the POLARBEAR experiment, could be tested. Although not directly applicable to the new generation of detectors for POLARBEAR-2, the designs contained many useful aspects that could be scaled to the new requirements. These included the vacuum chamber design, internal mechanical support structure, electrical feed-through harness, thermal anchoring, and optimal thermometer locations. Following conceptual design, materials were selected on the basis of their thermal and mechanical properties. Relevant thermal properties included the thermal conductivity of the material, thermal contraction/expansion coefficient, and heat capacity. Thermal conductivity was discussed in the previous section and tabulated values are readily available for most materials. However, when certain materials are subject to temperatures below 77 K their thermal conductivity can vary significantly, depending on the level of impurities in the material. In general, the more pure a material is the higher thermal conductivity it will have at cryogenic temperatures.

In order to characterize the thermal conductivity of pure materials in a cryogenic temperature regime, a measure of electrical resistance is used to provide a relatively simple solution to a potentially difficult measurement. Typically the residual resistance ratio (RRR) [33] of the material is measured. This is defined as the electrical resistivity of a material

at room temperature divided by the same measurement carried out at the cryogenic temperature of interest. The resultant value is given as a percentage and is independent of the length or cross-sectional area of the object. Materials with a high thermal conductivity are used when heat transport from one location to another is desired, for example, when making a thermal connection between the pulse-tube and the radiation shields. When this is the case it is beneficial to use a material such as oxygen-free, high thermal conductivity copper (OFHC), due to the efficiency with which it conducts heat. Purities of OFHC copper typically range from 99.95% (i.e. 0.05% oxygen content) on the lower end to 99.999% ("five-nines") at the higher end. When thermal isolation is desired, such as the support structure between the different temperature stages of the cryostat, materials with a low thermal conductivity should be used. While various grades of stainless steel are commonly used in fabricating cryostat support structures due to its low thermal conductivity and high mechanical strength, superior isolation is achieved using non-metallic materials. Examples of this include fiberglass reinforced epoxy composites (e.g. G-10), polymides (e.g. Kapton), Mylar and Nylon. A complete list of material properties are available in [33].

Another important property to consider is the degree to which the material will expand or contract when cycling through a range of temperatures. When a material is subject to cooling it tends to contract. This can cause stresses to develop between materials of different compositions, dimensional tolerances to be exceeded, and vacuum leaks and/or thermal shorts to develop. Therefore, materials must be carefully matched in order to avoid these potential problems. Finally, the heat capacity of the material needs to be considered, which is defined as the amount of energy that must be extracted from a material in the form of heat to lower its temperature by one degree. Heat capacity scales as the temperature cubed and provides insight into the timescales over which different materials cool. It should be noted that this property decreases significantly at cryogenic temperatures, explaining why the majority of the cool down time for a given system is spent above 77 K.

The mechanical properties of materials used in cryogenic construction are ultimately the most important consideration, since structural failure would ruin an experiment and possibly result in personal injury. It is therefore imperative to choose the appropriate materials for critical sections of the cryostat. The primary mechanical properties of concern are fracture roughness and yield strength. Fracture toughness is measured by how much stress must be applied to a defected region of a material (e.g. a crack) to cause it to grow. This

is important since a material's resistance to deformation, to the point that structural failure may occur under tensile stress, is often compromised when it is cooled. As a result the material can become brittle and cracks can develop. When possible, materials that are not subject to this effect should be used, such as stainless steel, aluminum and copper. These materials, and other similar ones with a face centered cubic (f.c.c.) crystal lattice structure, are proven to be less susceptible to this effect over a wide range of cryogenic temperatures. The yield strength, defined as the stress at which materials will no longer behave elastically, was also considered. A material subject to a stress exceeding this limit will deform plastically (i.e. the effect will be irreversible) and its behavior will no longer be predicable.

After all the materials were selected, individual cryostat parts were sized to accommodate the 6" detector wafer. Since there was a dimensional change from the existing configurations, it was necessary to perform the appropriate calculations to ensure the cryostat supports were structurally sound. It was necessary to size the supports, to minimize the amount of heat being transferred between the different stages, while still providing the support necessary to accommodate the mechanical load.

2.4 Cryostat Architecture and Thermal Loading

2.4.1 Overview

A view of the cryostat system is shown in 2.1, with all of the important features labeled. From this figure it is evident that the cryostat consists of two distinct temperature regions. Since both the mechanical and thermal design processes are highly dependent on the operational temperature range, each section is discussed separately.

The first section of the cryostat is operated from room temperature to approximately 4 K, and is composed of a cylindrical vacuum chamber and two actively cooled shells that act as radiation-shields. Each shell is terminated at either end by a circular plate. Collectively, we refer to the actively cooled components by their nominal operating temperature (i.e. the 50 K shell and plates will be referred to as the 50 K stage.) These components are configured in a nested manner, beginning with the vacuum shell on the outside and the progressively colder stages mounted concentrically inward using thermally isolating supports. The vacuum chamber provides an environment in which the majority of the potentially heat conducting air molecules have been removed. The second and third shells are cooled to

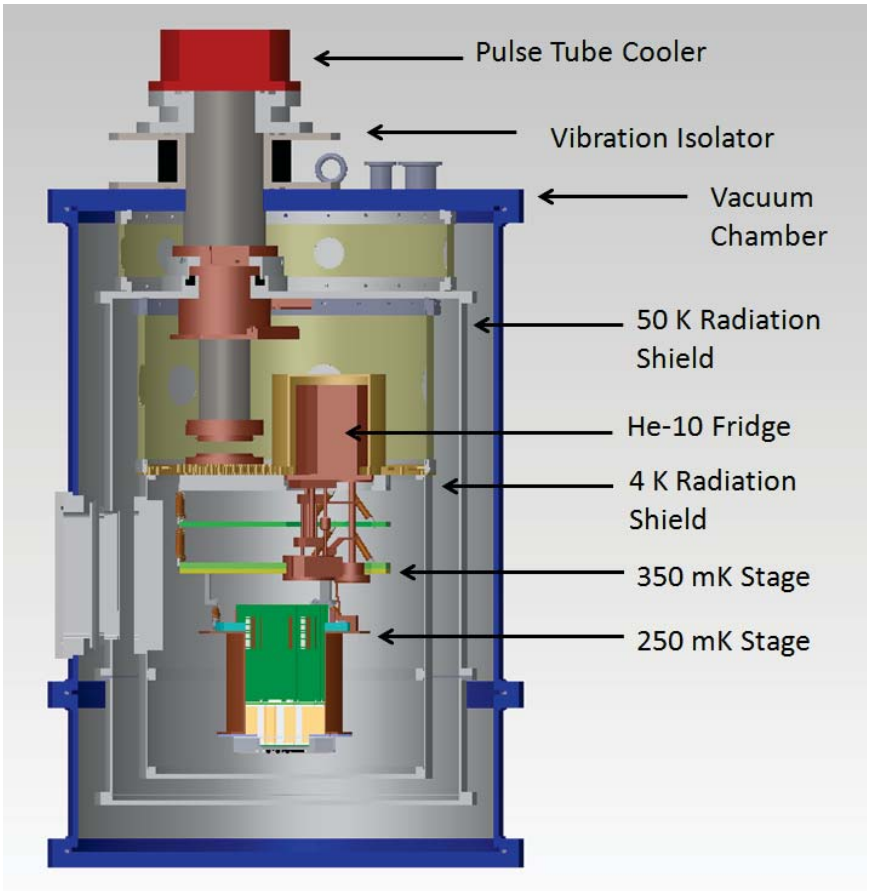

Figure 2.1: Solidworks model of cryostat with components labelled.

temperatures of 50 K and 4 K, respectively, using the Cryomech PT-415 pulse-tube cooler. While both shells function to intercept the radiation heat load from the warmer adjacent shell, it is the 50 K stage that buffers the bulk of the load. This is a result of its physical position, being directly subjected to radiation from the much warmer vacuum shell, which is at room temperature (approx. 300 K). This leaves the 4 K stage to intercept the smaller heat load from the 50 K stage. The role of the 4K section is to provide an environment within which the sub-Kelvin components can reside and perform as desired.

The section of the cryostat that is operated at sub-Kelvin temperatures is more complex than the warmer sections. Materials act much differently at these low temperatures and the availability of cooling power is significantly reduced. As a result, the choice of materials and degree of thermal loading become much more constrained. It is for this reason that the warmer section must perform optimally to mitigate the presence of significant thermal loads on the sub-Kelvin components.

2.4.2 Cryogenic Refrigeration

The test cryostat developed at Dalhousie University uses two types of refrigeration systems operating in parallel. A commercially available pulse-tube cryocooler (PTC) from Cryomech Inc [2] is used as the primary source of cooling power, while a three-stage helium sorption refrigerator from Chase Research [3] is used to achieve sub-Kelvin temperatures.

The PTC used in this work, namely the Cryomech PT-415, has two stages that are capable of providing 40 W of cooling power at 45 K, and 1.5 W of cooling power at 4.2K. When no thermal loading is present, it is possible to achieve a base temperature of 32 K and 2.8 K at the first and second stage, respectively; after a cool-down time of only sixty minutes. To provide further vibration isolation, the system is equipped with a remote motor option where the pulse-tube motor is mounted adjacent to the cryostat and connected via a bellows assembly to the system head.

The three-stage sorption refrigerator is not commonly employed outside of observational cosmology; therefore some background information on its operation is appropriate. As will become more apparent later, pumping on condensed helium gas provides the cooling power in this type of system. While single and two-stage options are available, a three-stage design can be advantageous when large thermal loading is expected. Since this application involves attaching a significant amount of readout wiring to the sub-Kelvin stages, additional heat buffering was necessary. The result is a system that is capable of sustaining a base temperature for extended hold times. Even though there are three stages present, visual inspection would suggest only two. This is an effect of the nested design in which the second stage, containing 3He, resides within the first stage, containing $^4\mathrm{He}$. Collectively, the first and second stages are referred to as the intercooler (IC) stage and act as a heat buffer for the third stage. The final stage is referred to as the ultracooler (UC) stage and once again, contains $^3\mathrm{He}$. The intercooler stage is capable of reaching a base temperature of 500 mK for a hold time of approximately 24 hours when subject to a heat load of 115 μW. An even lower base temperature of 240 mK is possible at the ultracooler stage. However, to achieve the same hold time, the stage may only be subjected to a maximum heat load of 3 μW.

The device itself is quite simple. It is composed of a vessel that is charged with $^4\mathrm{He}$

[2] http://www.cryomech.com
[3] http://www.chasecryogenics.com

or ^{3}He gas, a heatable material with a high surface area, and a reservoir to collect the condensed helium gas referred to as a still. Figure 2.2 shows a schematic of the three-stage sorption refrigerator developed at Chase cryogenics with the important components labeled. The high-surface-area material used in this refrigerator is a small quantity of activated charcoal located in each of the three stages. By supplying an electric current to a metal film resistor embedded within the charcoal, it is possible to control the heating of the material.

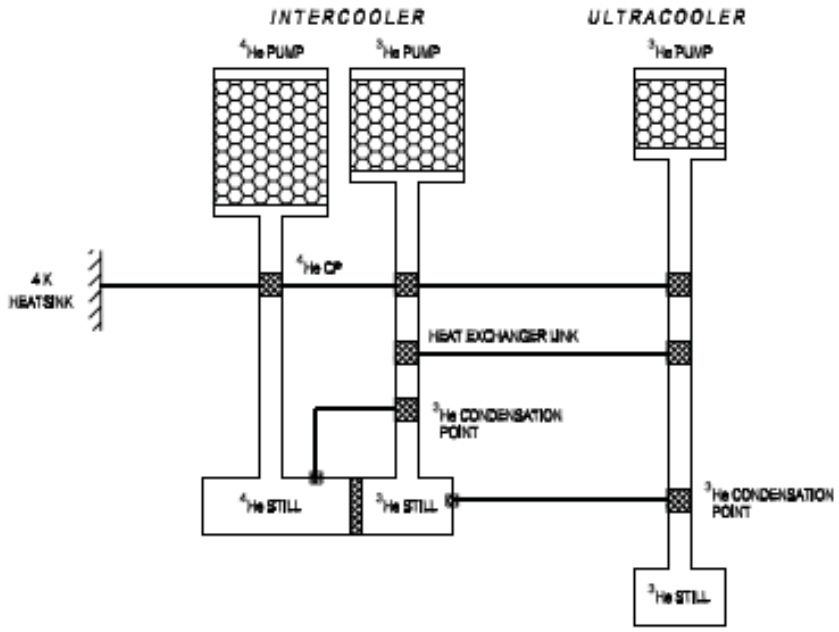

Figure 2.2: Schematic of the sorption refrigerator [13].

To operate the refrigerator it is mounted to the 4K cold plate of the cryostat so that it initially cools down from room temperature with the rest of the system. Since the pump is connected to the still by a stainless steel tube that is essentially thermally isolated, the pumps cool at a much faster rate than the stills. As a consequence, the helium gas is adsorbed onto the surface of the charcoal, further impeding the transfer of heat to the stills. Therefore, it is necessary to apply a small current to the resistor to heat the pumps sufficiently so that some gas is desorbed. The desorbed gas then acts as a conductive pathway by which the rest of the system is cooled more efficiently.

The cooling cycle continues by further heating the charcoal, in the first stage of the refrigerator, to above 45 K to expel the remaining 4He gas from its surface. Once all of the gas has been desorbed into the vessel, a thermal link is created between the 4.2 K main plate

of the cryostat and the first stage of the sorption refrigerator. The link acts in combination with the increased vapor pressure to cool the gas below its critical temperature and causes it to begin to condense into the reservoir. During this process the charcoal must remain heated so that the gas does not adsorb back onto its surface. Allowing the charcoal to cool via a gas gap heat switch reduces the temperature of the liquid by causing the gas that boils off of the reservoir to be re-adsorbed. Repeated ”pumping” on the liquid helium in this way causes it to reach a temperature of 0.9 K by lowering the vapor pressure in the still. Just as the main plate acted as the condensation point for the $^4\mathrm{He}$ in the first stage, the first stage acts as the condensation point for the $^3\mathrm{He}$ in the second stage. This in turn acts as the condensation point of the $^3\mathrm{He}$ in the ultracooler stage.

When cycling in this way it is important to wait for all of the $^4\mathrm{He}$ charge to evaporate before pumping on the $^3\mathrm{He}$ in the second stage. If not, the $^4\mathrm{He}$ will become a superfluid and create a thermal short. This issue is mitigated in the new Chase gas light refrigerator, which is used in this work. The main difference between this system and the one explained above is that a larger $^4\mathrm{He}$ charge is used in the first stage to buffer more of the parasitic heat load. This provides a more economical solution since the amount of $^3\mathrm{He}$ that is necessary in the second and third stages is reduced. A heat exchanger located between the intercooler still and the base plate provides additional buffering of parasitic loading.

For a more in depth discussion of the thee-stage Chase cryocooler see [13].

2.4.3 Vacuum Chamber

The vacuum chamber was designed to be bi-sectional, consisting of two separate sections bolted end-to-end. This was done to ease the process of mounting and dismounting the detector wafer, and to accommodate future optical testing. The chamber was fabricated from 6061 grade Aluminum that was rolled and welded into a cylindrical tube with an internal diameter of 0.525 m. Flanges containing o-ring sealing grooves were then welded on either end for bolting the different sections together. The top plate of the vacuum chamber, manufactured from 25 mm thick, 6061 aluminum, served two main purposes. First, it acted as the primary interface between room temperature and the actively cooled components of the cryostat, providing the access ports for the vacuum and cryogenic cooling hardware. It contained one KF 25 vacuum port, one KF 50 vacuum port, a pressure release valve and one 165 mm diameter clearance hole for mounting the combined vibration isolator/PT415

head assembly. Second, the plate functioned as the central mounting point for all of the colder sections contained within the vacuum chamber. Each of the cylindrical sections has a wall thickness of 5 mm and when combined, have an overall height of 0.785 mm. The result is a 140 L cryostat.

These dimensions were chosen to accommodate the internal structure of the cryostat and to sustain a base pressure of $P < 10^{-6}$ Torr. Due to the large volume of the vacuum chamber, two different pumps were used; one designed for high volume and moderate vacuum and one designed for low volume and high vacuum. The pump-down procedure was initiated by attaching an Edwards rotary vane pump to the KF 25 vacuum port on the cryostat. This was done using a bellows assembly and an in-line oil trap filter to minimize any chance of oil migrating into the system. Once this pump reduced the pressure to approximately 0.1 Torr, the turbo pump was turned on. The turbo pump chosen for this application was the Varian Vacuum Technologies TPS-compact [4]. This fully integrated system was configured with the TV301 Navigator Turbomolecular Pump and backed by the Varian 60 L/min IPD-3 Dry Scroll pump. As a result, pressures on the order of 10^{-3} Torr were quickly realized. At this point the PTC could safely be turned on to initiate the cooling cycle. The cooling of the PTC heads provided a cryo-pumping effect that led to base pressures on the order of 10^{-6} Torr within less than an hour.

2.4.4 50K and 4K Stage

The upper plate of the 50 K stage has a radius of 235 mm and was fabricated from 9.525 mm thick, 6061 aluminum. This grade of aluminum was chosen based on a compromise between structural suitability, thermal conductivity and machinability. This plate was directly connected to the first stage of the PT-415 via a thermal link. It has a nominal operating temperature of approximately 50 K and is referred to as the 50 K cold plate. Placed in good thermal contact with the plate was the mating radiation shield that measured 0.615 m in height. As with the vacuum chamber, the radiation shield was segmented into two sections. The role of the plate was to distribute the cooling power of the pulse-tube along the 1.78 mm thick walls of the radiation shield composed of the same material. This acted to minimize radiative and conductive heat loads on the enclosed components.

[4] `http://www.home.agilent.com`

The degree to which a surface is subjected to the effects of radiative heat transfer depends highly on the surface emissivity [113]. It was possible to reduce radiative loading on the 50 K stage by covering in the surface with a multi-layer insulation (MLI) blanket. An MLI blanket typically consists of a series of layers fabricated from a high reflectivity material interleaved with an insulating material such as silk, polyester or nylon. The role of the insulating material was to reduce the flow of heat across the different layers. The high reflectivity material used to wrap our radiation shield was fabricated by depositing a thin layer of aluminum on an ethylene-dimethyl-terepthalate film (i.e. Mylar). Since the heat transfer associated with radiative loading scales inversely with the thickness of the MLI stack (i.e. the number of layers used) [57], 30 layers of the aluminized Mylar were used. Additional regions that were not covered by the MLI blanket were sealed using aluminum tape.

To support the 50 K stage from the top plate of the vacuum chamber, a segmented G10 tube support was used. G10 is a fiberglass epoxy laminate commonly used in circuit board fabrication. It posses a high tensile strength 32000-40000 PSI [5] and a thermal conductivity that drops off exponentially with temperature below 100 K. The result was a support that was both structurally sound and thermally isolated. The G10 tube was divided into 4 equal sections to provide ease of access to the 50 K PTC head and thermometry while still maintaining mechanical support. Each section has a wall thickness of 3.175 mm and when combined they created a tube with an inner radius of 0.440 m. The structure was designed to provided maximum support for loads parallel to the cryostat axis. Lateral loading while significantly reduced from that of the parallel load met operational needs. This cryostat was designed with the intention of being used exclusively for laboratory testing, operating in a vertical orientation. Deviations from this would only occur when accessing the focal plane assembly.

The structural and thermal architecture of the 4 K stage was designed to be very similar to that of the 50 K stage. The 4 K cold plate, measuring 178 mm in radius and 9.525 mm in thickness, was cooled via a direct thermal link to the second stage of the PT-415. An important property of heat transfer considered when dealing with temperatures of 4 K and below, was that the thermal conductivity of certain materials changes. This regime has often been referred to as a gray area when choosing appropriate materials, since heat

[5] http://www.mcmaster.com/#8549kac/=tc3uwb

transfer begins to occur through electrons instead of phonons. To ensure that a uniform temperature gradient was achieved across the entire 4 K cold plate, it was manufactured from OFHC copper. Copper was chosen since it has a higher thermal conductivity than aluminum and has proven to produce desired results in other similar experiments [8]. The surface of the 4 K cold plate was treated with gold electroplating for improved thermal contact. The gold essentially fills any surface imperfections and is soft enough that it allows for better thermal contact to be realized when pressure is applied to a joint.

The 4 K cold plate serves several important functions. Just as the 50 K cold plate does, the 4 K cold plate acts as a thermal intercept for radiative and conductive heat loading from warmer sections of the cryostat. In addition to this role, it serves as both a mechanical and thermal anchor point for different components within the cryostat. Both the $^3\mathrm{He}$ sorption refrigerator and the sub-Kelvin stage assembly that it cools are fixed to this stage. It also serves as the thermal anchor point for the SQUID pre-amplifiers used in the readout chain. Since the SQUID amplifiers will not operate unless they are cooled below 7 K, it is essential that this stage has sufficient thermal performance to ensure this can be achieved. As a result of its critical role this stage is often referred to as the main stage.

The radiation shield that interfaces with the 4 K cold plate was also manufactured from Aluminum 6061 with a wall thickness of 1.78 mm. The cylindrical shield was again segmented into two pieces to accommodate future optical tests and has a total height of 0.365m. Although not as critical as it was at the 50 K stage, due to a smaller incident radiative heat load, the radiation shield was wrapped in 30 layers of MLI.

The 4 K stage was suspended from the 50 K cold plate using a scaled down version of the sectioned G10 support tube which was used between the vacuum chamber and the 50 K stage.

2.5 Sub-Kelvin Stages

The ”sub-Kelvin stages” refer to those that couple the 4 K stage to the detector module. They are arranged in a layered fashion similar to that of a wedding cake. To be consistent with the labeling of the warmer stages, the plates are referred to by their nominal operating temperatures and are shown in figure 2.1. The plates are machined from aluminum 6061 except for the plate directly adjacent to the detectors which is made of OFHC copper.

Cryogenic cooling was provided to the stages via a heat strap connected to the cold

heads of the Chase refrigerator. The first plate of the four-level mK assembly was bolted directly to the cryostats 4 K cold-plate, providing a base structure onto which successive stages could be fastened. A heat exchanger located on the Chase fridge was then used to cool the second plate to approximately 1.5 K. This serves as an anchor point for heat sinking the electrical wiring used to read out the detectors, a potential source of significant thermal loading. Another thermal link was attached between the IC head of the fridge and the "350 mK stage". This acted to buffer the thermally conductive loads from the mechanical supports and also served as an additional point to heat sink wires. The "250 mK stage", referred to as the main stage, was cooled via a connection to the UC head of the Chase fridge. The sole purpose of this stage was to cool the TES bolometers into their superconducting transition.

Mechanical support and thermal isolation was provided by a series of individual Vespel rods arranged in a diagonal truss structure between each of the different temperature stages. Vespel is a highly durable polyimide with exceptional thermal resistance and is available in a variety of different grades. Although more costly than G-10, it provides a solution with an order of magnitude less thermal conductivity. The truss configuration was chosen to maximize the mechanical rigidity of the overall structure while minimizing conductive heat load between stages. By slanting the rods the total thermal path was increased, which aided in reducing the heat load and contributed to a more compact design. The length of the rods was a compromise between thermal and mechanical properties. It was chosen to ensure that the conductive loading did not exceed the available cooling power while still producing a structure that had adequate structural stiffness. The rods were purchased as solid cylinders that were then hollowed out to minimize their cross-sectional area, thus further reducing any conductive loading. A small hole was drilled into each rod section to evacuate any trapped gasses when bringing the cryostat under vacuum. Aluminum flanges, designed with through-holes, were attached to either end of the rods to allow them to be fastened around the perimeter of the cold stages. Sets of connectors were fabricated for each of the rods, providing a mount point for attaching them to the mK plate structure. One end was machined to fit a precision shoulder screw, while the other was threaded. A thermal epoxy (Stycast 2850FT [6]) was applied to the threaded end that was then inserted into the hollowed out rods. Since alignment of the plates with respect to each other was

[6] http://www.ellsworth.com/emerson-cuming/stycast/

critical, a specially designed jig was used to hold the rods while the epoxy cured.

A total of six Vespel supports were used to span each level. Two different grades were used, SP1 and SP22. The connections from 4 K to 350 mK were made using 50.8 mm long rods of Vespel SP-1, the most pure form of the polyimide. For the connection between 350 mK and 250 mK, a graphite enhanced version with lower thermal conductivity was chosen. Each support was hollowed to have a surface area of 6.45 mm^2. A finite element analysis (FEA) of this support structure is shown in 2.3.

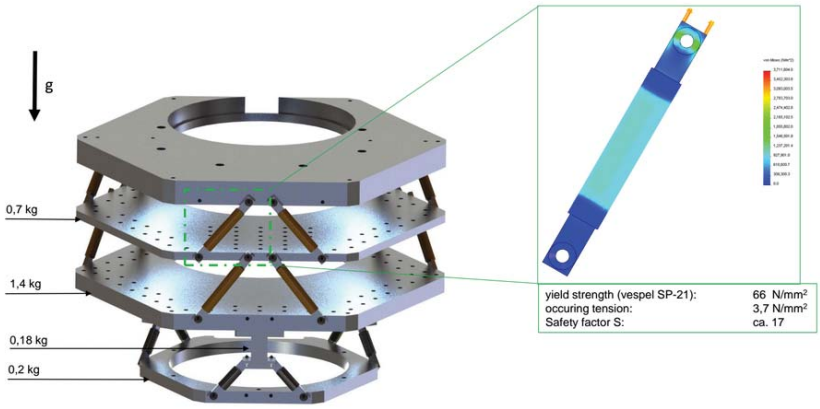

Figure 2.3: FEA for the Vespel support structure. The simulation was done for a single Vespel support and assumes the total force is from the interaction between gravity and the plates as shown. Analytic calculations based on the weight of the plates show the Vespel supports spanning the 4 K to 2 K sections will be subject to the highest force. Since a simulation of the entire structure would have resulted in a less accurate solution (due to the numerical method used in the Solidworks FEA package), a single support subject to the highest force was chosen. Simulation and figure compliments of Philipp Heyne.

2.5.1 Thermal Connections

This section discusses the connections used to establish a thermal link between the cryogenic coolers and the respective cold stages of the cryostat, called ”heat straps”. The same approach was taken for both the sub-Kelvin and 50 K to 4 K sections. In each case, the design challenge was to provide a solution that maximized the thermal conductivity while minimizing the extent of mechanical coupling between the independent components. Both requirements were met using multiple lengths of braided copper speaker wire welded to OFHC copper plates as shown in figure 2.4. The braided nature of the wire ensured a rigid

connection was not present, thereby isolating the vibrations generated by the cooler on the rest of the system. Widespread use of high-purity copper speaker wire in the audio industry made it readily available. To achieve maximum thermal conductivity across the heat straps, an OFHC copper wire (Belden 1311A [7]) with 99.999% purity was used. Values for the thermal conductivity of RRR100 copper at the temperatures of interest are listed in the table below:

Note: Values are from the National Institute for Standards and Technology (NIST) [8]

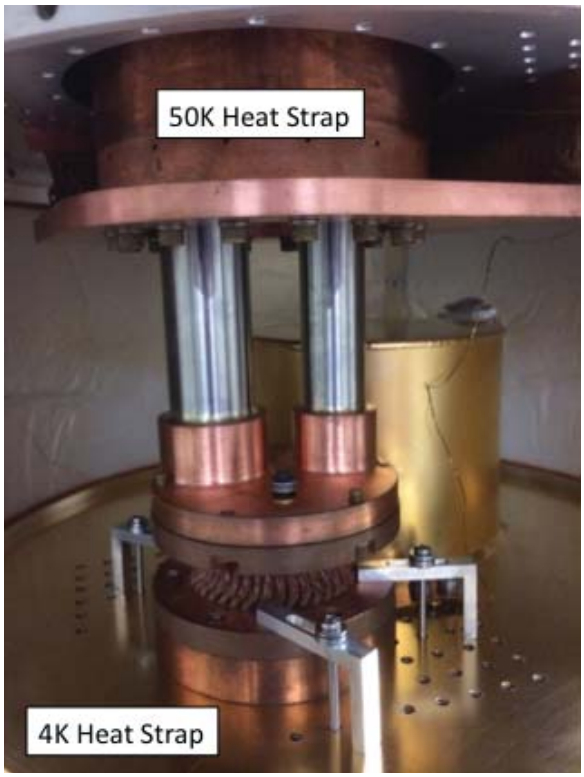

Figure 2.4: 50K and 4K heat straps installed in cryostat.

Given that all wires in a braid may not be in good contact with eachother, it was necessary to assume an effective diameter over which conductivity will occur. The thermal connections in this work used a 14 AWG wire that was fitted into a 1/8" diameter hole in the copper plate. Given this configuration, an effective wire diameter of 1/16" was assumed. From this it was possible to calculate the amount of cooling power that is transferred across the strap using the wire lengths listed above. The surface area of the plate was not considered in this calculation since it is the section composed of braided wire that limits the heat

[7] http://www.belden.com
[8] http://cryogenics.nist.gov

transfer.

Each heat strap was assembled from a number of copper platforms, multiple lengths of speaker wire and a wire holder for each plate. The copper platforms were used to bolt either end of the heat strap to its respective regions and as discussed before, the speaker wire was used as a thermally conductive mechanical isolation. Due to welding constraints a wire holder consisting of a thin block of copper with a series of clearance holes to accommodate the speaker wire was designed. The speaker wire was first welded to the holder and then the holder was welded to the platform. This ensured that the high-temperature welding process did not burn the braided wire before it coalesced to the high mass, copper end-piece. For the connection at 50 K, one end was machined to follow the contours of the PTC head while the other end consisted of two identical triangular pieces. These were attached to opposing sides of the 50K cold stage to increase the likelihood of more uniform cooling across the aluminum section. A total of 56, 2" length wires were used, far exceeding the amount required to achieve sufficient cooling at this stage.

The 4 K heat strap was designed similar to the one used at 50 K except for the platform that attaches to the cold stage of the cryostat. Since the 4 K cold plate was manufactured from gold plated copper and was not as large as its warmer counterpart, uniform cooling was not considered a significant issue. For this reason, a single connection that minimizes the total wire length was selected. A total of 40 wires were used for the 4K connection, each with a length of 2".

To address the issue of differential thermal contraction and subsequent loosening of the attached heat straps, a combination of brass screws and stainless steel Bellville washers were used in conjunction with the copper parts. Brass has a slightly higher thermal expansion coefficient than copper which causes it to contract faster upon cool-down, therefore tightening the connection. Belleville washers provide an additional source of applied force to buffer any effects of contraction not addressed by the brass screw. This is necessary to provide an efficient thermal interface across the strap.

2.5.2 Thermometry

System temperatures were monitored using a combination of silicon diode and germanium resistance temperature detector (RTD) thermometry from Lakeshore Cryotronics. Silicon diodes were used as a general purpose thermometer and were placed on the 50 K and 4

K stages. A diode thermometer was chosen as a result of its intrinsically simple readout and low cost. However, they are not as accurate and do not have as good reproducibility as resistance thermometers. For this reason, colder temperatures (i.e. those less than 4 K) were monitored using a germanium RTD. These types of resistance thermometers function similarly to a semiconductor in that their resistivity decreases non-linearly with increasing temperatures. This property makes them more suitable for low-temperature applications. A major drawback of semiconductor-like thermometers is the need to carefully calibrate each one due to a large variability between sensors. One Germanium RTD used in this application was calibrated at Lakeshore Cryotronics to have optimal sensitivity from 0.3 K to 100 K with an accuracy of +/- 4 mK. The remaining sensors were then calibrated using this as a reference.

A custom temperature readout board fabricated at McGill University (figure 2.5) was used to monitor the sensor output.

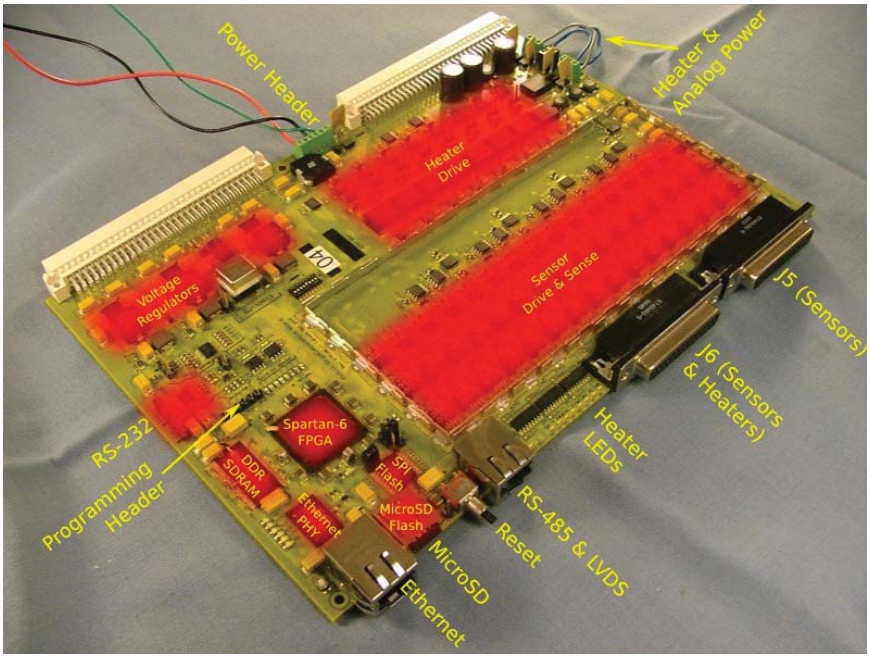

Figure 2.5: Top of the custom temperature readout board with major subsystems and connectors labeled

2.5.3 Results

To measure the thermal performance of the cryostat, the system was cooled from room temperature to 4K using the PTC. Temperature sensors were placed at critical locations,

shown in fig, to confirm that operational requirements were met. With the wireharness and sorption refrigerator installed, the cryostat took about 12-14 hours to achieve stable base temperatures (figure 2.6). This validated that no thermal leaks were present and the sorption refrigerator could be cycled.

Small-scale variations in the base temperature of the 4K stage were found after stabilization (figure 2.7). The period of these fluctuations suggest they originated from the low-frequency pulsing of the PTC. Similar work [8] has shown the same result and concluded that this does not translate into a significant amplitude variation in the temperature of the mK stages.

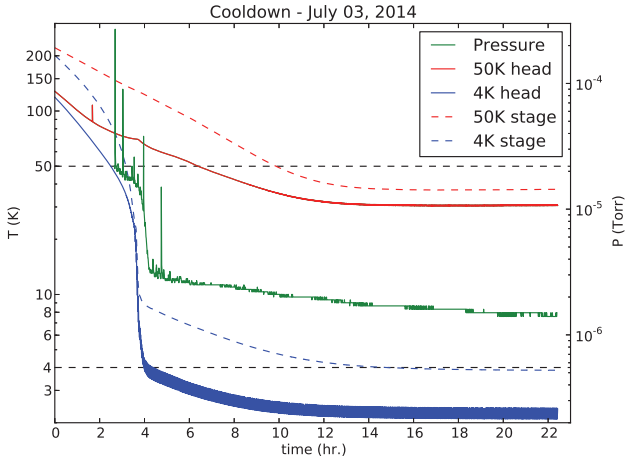

Figure 2.6: Time elapse of critical temperatures beginning at room temperature (t=0)

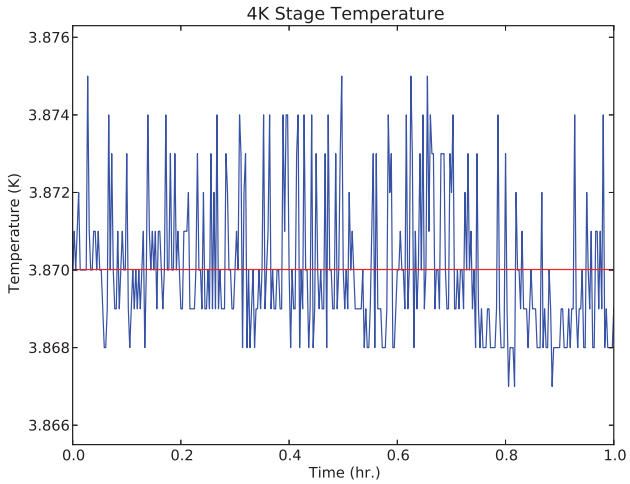

Figure 2.7: Small-scale temperature fluctuations at 4K stage due to PTC.

Chapter 3

The Polarbear Cosmic Microwave Background Polarization Experiment and Field Deployment

This chapter presents the POLARBEAR experiment, which is currently taking polarization measurements of the cosmic microwave background. I begin by providing an overview of the project to motivate the work done in the previous chapter. This is followed by the results of two recent publications by the POLARBEAR collaboration [1, 2] and then shifts towards my specific contributions. I then conclude by outlining my contributions to this work, which mainly consist of taking observations and providing field support for the operations.

3.1 Introduction

POLARBEAR is a ground-based cosmic microwave background (CMB) polarization experiment located high in the Atacama Desert in Chile. While previous experiments have characterized the E-mode polarization pattern, POLARBEAR attempts to characterize the much fainter B-mode polarization over a range of angular scales. The experiment is being deployed in three main phases, each designed to improve the sensitivity of it predecessor. Since the TES detectors have become limited by statistical fluctuations in the arrival rate of photons (i.e. background limited), the most effective way to increase the sensitivity is to increase the optical throughput.

The first generation of the experiment achieved ”first light” in January 2012 and continues to observe the sky at 150 GHz with 1274 antenna-coupled TES bolometers located at the focal plane of a 3.5 m primary off-axis Gregorian-Dragone telescope. The telescope provides a 3.5 arc-minute beam that is well suited for high precision measurements over the necessary range of angular scales. The large focal-plane array provides increased mapping speed over the previous generation of cosmic microwave background experiments. POLARBEAR performs a deep search for the B-mode polarization pattern resulting from

inflationary gravitational waves at angular scales of several degrees with a sensitivity enabling detection of a tensor-to-scalar ratio of $r = 0.025$ with a 95% confidence level, after collecting data for two years. In addition, it searches for B-mode polarization patterns at angular scales of arc minutes resulting from the gravitational lensing of E-mode polarization. When combined with data from the Planck satellite mission, the latter will allow for a constraint on the sum of neutrinos masses to the 100 meV level at a 68% confidence level.

The second generation of the experiment, POLARBEAR-2, will consist of a receiver upgrade, housing a multichroic focal plane of dual-band dual polarization pixels coupled to 7588 antenna-coupled TES bolometers. This design will provide an increased sensitivity over its predecessor, POLARBEAR. POLARBEAR2 will provide a sensitivity that will enable a detection of a tensor-to-scalar ratio of r=0.01 with a 95% confidence level. In addition, it will further constrain the sum of neutrino masses at the 90 meV level and when combined with data from Planck, will provide a constraint at the 40 meV level with a 68% confidence level. POLARBEAR-2 observations plan to begin in 2015.

The final stage of the experiment intends to expand on the POLARBEAR-2 design by observing the CMB with three multi-frequency telescopes. This configuration, referred to as the Simons Array, will enable a precise characterization of the inflationary and gravitational lensing B-mode signals. The Simons array will allow POLARBEAR to distinguish itself from other experiments by efficiently mapping large areas of the sky with more that 20,000 multichroic TES bolometers with unmatched speed and sensitivity.

3.2 Science Goals

Characterization of the CMB anisotropies has played a crucial role in progressing our knowledge of the current universe and the models that govern cosmology. Previous experiments have studied the small-scale temperature anisotropies leading to the precise measurement of the basic parameters that describe our universe. To date, observations support the prevailing cosmological model which describes an expanding universe that originated from a hot and dense state. These observations are also consistent with the idea that the large scale structure we view today resulted from primordial density perturbations that grew through gravitational instability. However, predictions based on the physics of this model suggest a universe that differs from existing data in several aspects. Although the majority of these issues can be solved using inflationary theory, the framework on which it resides is

relatively poorly understood and unconstrained. Thus, it is not sufficient to study the intensity anisotropies alone. Polarization measurements, however, provide unique insight into this process and help break parameter degeneracy. The data can then be used to provide further constraints on cosmological models.

Theories surrounding inflation have yet to be proven, but suggest that the universe underwent a rapid period of exponential expansion 10^{-36} seconds after the initial Big Bang. A direct consequence of this growth is that both scalar and tensor perturbations are predicted to have occurred in the CMB. While the scalar component has been well characterized, the tensor perturbation remains subject to further research. From a scalar perspective, the same process (i.e. tiny density fluctuations in the primordial photon-baryon density fluid) that gave rise to the observed temperature anisotropies is believed to have produced an even parity E-mode polarization in the CMB. On the other hand, the tensor component is thought to have resulted from gravitational waves imprinting an odd-parity B-mode polarization signature in the CMB. This is believed to occur from the waves inducing a stress on the photon-baryon fluid as they propagate through. Using both temperature and E-mode polarization data, the current tensor-to-scalar perturbation ratio (r) is constrained to 0.025. However, as more data becomes available, this limit can be improved upon.

POLARBEAR is designed to measure the tensor B-mode polarization component over a range of angular scales. On large scales, it seeks the unique signature of inflation and sheds light on the nature of a process that would have had to occur on an energy scale that far exceeds the ability of any particle accelerator. On small scales, it probes B-modes that have been converted from E-modes through gravitational lensing, produced from the effect of large-scale structures. By measuring these lensed modes, POLARBEAR attempts to provide insight into various aspects of structure formation, including dark energy, and may potentially constrain the sum of neutrino masses.

Measurements of the B-mode signal require an instrument with a high degree of sensitivity over the frequency range of interest as well as stringent control over systematic errors. Observations of the CMB with a large-format detector array in a high quality millimeter wave site (i.e. one in which the contribution from absorption and emission in the atmosphere is minimized), allow POLARBEAR to maximize measurement sensitivity. Control over systematic errors is made possible through a combination of polarization modulation, a large beam and an optical design with low sidelobe response.

3.3 Scan Strategy

POLARBEAR is currently observing three 3° by 3° CMB patches that were chosen to have minimal foreground contamination from polarized galactic sources, predominately resulting from synchrotron radiation and thermal dust emission. The experiment uses an observing frequency centered at 150 GHz to coincide with the atmospheric water vapour window, - a condition that is necessary for ground based observation. By conveniently choosing patches that overlap with other CMB experiments, POLARBEAR is able to accurately characterize and remove residual foreground contamination. The observation patches that were chosen are shown in 3.1, along with current and future complementary CMB projects and an estimate of galactic dust emission intensity.

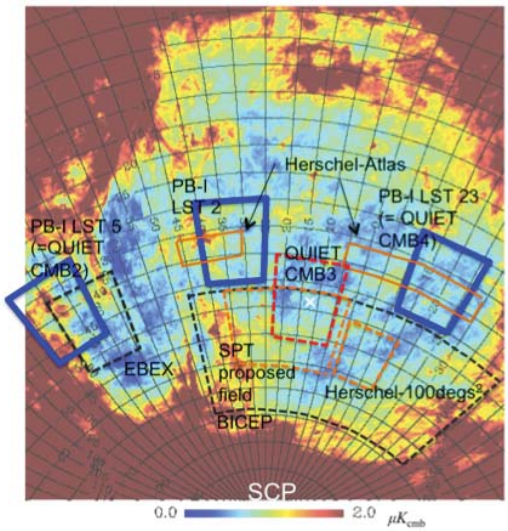

Figure 3.1: POLARBEAR observation patches shown outlined in blue along with theorectical galactic dust intensity. Previously observed and proposed patches of observation from several complimentary experiments also indicated. [61]

Due to limitations in the amount of sky coverage accessible from the ground, observations with POLARBEAR are focused on detecting the gravitational wave signal, which peaks on a larger angular scale (i.e. higher value of l) than the pure B-mode. Since it is not necessary to observe large patches, longer integration times and the high instrument sensitivity can be used to create deep maps.

The patches are referenced by their location on the sky, centered at the following right ascension and declination: ”RA 23” (23h02m, -32.8 deg), ”RA 12” (11h53m, -0.5 deg), and ”RA 4.5” (4h40.2m, -45 deg). Observations began in May of 2012 and involves scanning

each patch at constant elevation for several hours per day. The patches are observed in 15 minute intervals by scanning in the azimuth direction as the patches drift through the telescope's field of view (FOV). Once the interval is complete, the telescope moves in both azimuth and elevation to track the patch. This process repeats from the time the patch rises above the horizon until it sets.

Telescope pointing and detector calibration is accomplished by integrating dedicated observations into the overall process. By observing a combination of bright astrophysical sources and point sources within the patches, Polarbear is able to achieve a pointing accuracy of less than 1 arcminute. To enable a relative calibration of detector gain, the receiver is subject to the radiation produced by a modulated thermal source mounted on the telescope. As a consequence of being a ground-based experiment, an additional gain calibration is necessary. This is facilitated by executing a series of scans in elevation, referred to as "el-nods", to account for variations in the density of the Earth atmosphere. Relative calibration of detector polarization angles is achieved by observing the highly polarized Taurus A (Tau A) supernovae remnant.

The choice of site location plays a major role in the scan strategy that will be adopted. The POLARBEAR experiment is located adjacent to the Atacama Cosmology Telescope (ACT) in the Chilean Andes at the James Ax Observatory on Cerro Toco. At an altitude of 5200 meters, the experiment continually collects science quality data in dry atmospheric conditions with a mean perceptible water vapor (PWV) content of 1.5 mm. While similar conditions are present in the South Pole, the mid-latitude site chosen for this experiment offers access throughout the entire year and sky rotation. The mid-latitude site also becomes very important when deploying a polarization sensitive experiment, since it can be used to modulate the polarization vector of the incoming photons.

3.4 Instrument Overview

To achieve the sensitivity and angular resolution needed to accurately characterize the B-mode polarization signal, it was necessary to develop a new generation of receivers with focal planes that implement thousands of imaging elements. By increasing the pixel count of the imaging device, increased sensitivity and faster mapping speeds were realized. This property is essential when attempting to measure a signal that is at least an order of magnitude fainter than the previously studied E-mode polarization. At this scale, instrumental

errors that can convert E-modes into B-modes (cross-polar response) and intensity into polarization (instrumental polarization) become a significant source of systematic error. Therefore an instrument designed to detect the B-mode polarization must employ both a kilo-pixel focal plane and maintain stringent control over systematic errors to achieve the necessary sensitivity.

POLARBEAR is designed to address the above constraints by using a 1274 element antenna-coupled focal plane integrated with a state-of-the-art millimeter-wave telescope. Each element is a polarization sensitive TES bolometer cryogenically cooled to 0.25 K. The accompanying optics include a series of reimaging lenses and a rotating half-wave plate (HWP). When operated in combination, the bolometer array yields a 2.4 degree field-of-view, which is well matched to the telescope's 3.5 arc-minute full-width half maximum (FWHM) beam at 150 GHz. While this optical configuration produces low levels of systematic error, it is not sufficient to address all of the contamination sources.

Further mitigation of systematic error is achieved by a variety of means. By implementing a rotating HWP on the sky side of the lenses, the polarization introduced by the instrument can be averaged out over multiple, rotational positions of the plate. To reject the off-axis optical response of the telescope, which can result in unwanted signal reaching the detectors when the beam sidelobes scan across high contrast objects (e.g. the Sun, planets, ground etc.), POLARBEAR uses multiple layers of shielding. In addition to the methods mentioned above, both a near-field and far-field calibrator source with known properties to ensure optimal performance of the system.

3.4.1 Huan Tran Telescope

The Huan Tran Telescope, which was built by VertexRSI [1] (now a part of General Dynamics), uses an off-axis Gregorian configuration design to maximize throughput and minimize the effects of cross polarization and sidelobe response. Although the microwave telescope is very similar in appearance to a radio telescope, the HTT has several distinct characteristics, the most significant being a large FOV. This property is necessary when paired with the large focal plane of POLARBEAR in order to optimize system throughput and enable the faint B-mode detection.

The off-axis Gregorian design offers an optically pure configuration with many key

[1] http://www.gdsatcom.com/vertexrsi.php

advantages. By offsetting the mirrors, photons will not be subject to beam blockage due to the support structure of the secondary reflector which can ultimately lead to scattering and diffraction. This clear aperture design limits the performance inhibiting characteristics of an on-axis design. While other CMB polarization experiments have employed a crossed-Dragone telescope, POLARBEAR uses a Gregorian design. The smaller secondary reflector inherent to these systems allows for a more convenient installation of baffling to limit sidelobe response.

An image of the HTT at the James Ax Observatory in Chile is shown in 3.2. The primary reflector consists of an ambient temperature 2.5 m parabolic reflector that was precision machined from a single piece of Aluminum to have a surface accuracy of 53 μm. A lower precision guard ring was then installed to give a total diameter of 3.5 m. The high-precision region produces a 3.5 arcminute beam at 148 GHz (the center of the observing band) capable of probing out to a multipole moment L of 2500 and able to resolve the peak of the gravitational lensing signal at L = 1000. A monolithic primary reflector with high surface accuracy enables POLARBEAR to mitigate errors that commonly occur in polarization experiments that use a segmented mirror [89]. Although measures can be taken to minimize the role of the small gaps between mirror segments, effects such as scattering, diffraction and polarization modulation can still be introduced to the signal. To minimize sidelobe contamination from unwanted sources such as ground reflection, the telescope incorporates a co-moving ground shield and prime focus baffle.

3.4.2 Cryogenic Receiver

When developing an instrument with a large aperture, it is necessary to filter the radiation that lies outside of the frequency band of interest. This reduces the thermal loading on the cryogenic components located in the receiver and helps maximize the performance of the system. As discussed earlier, the goal is to develop an instrument that is background noise limited. In an effort to meet this requirement, POLARBEAR adopts a thermal filter technology in place of the more classic, metal mesh filter. Thermal filtering presents a solution that offers both high optical throughput at desired wavelengths and minimal in-band emission.

POLARBEAR uses several multilayer low-pass filters in combination with a series of single layer IR shaders to remove thermal loads that would otherwise be incident on the

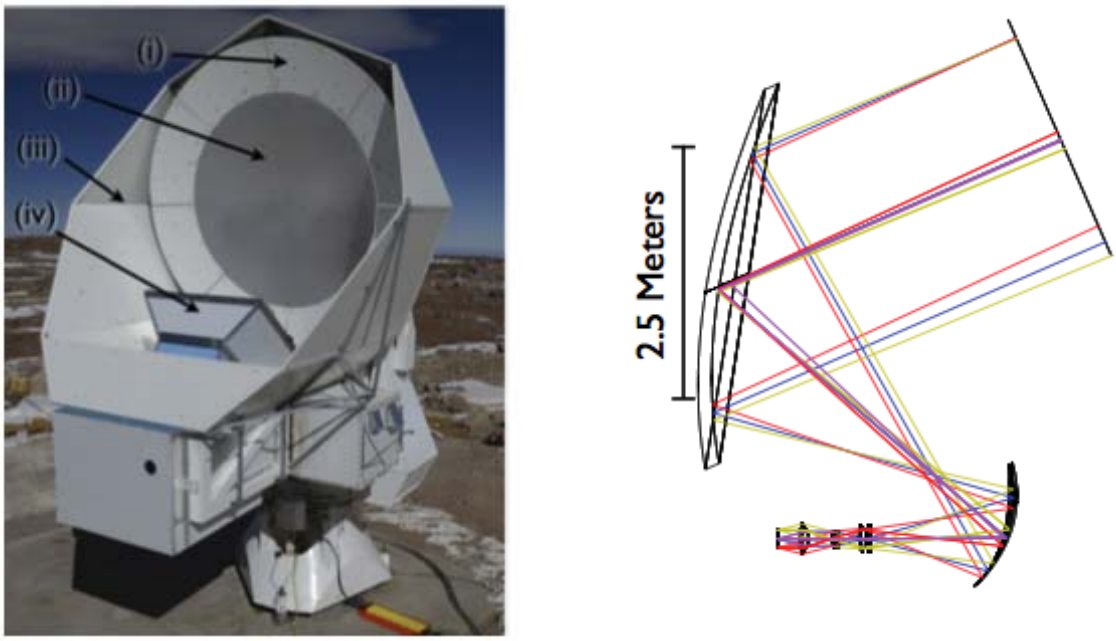

(a) (b)

Figure 3.2: (a) The Huan Tran Telescope as assembled at the Cedar Flat site in the Inyo Mountains of California. Indiciated in the image are (i) primary guard ring, (ii) precision primary mirror surface, (iii) co-moving shield, (iv), and prime focus baffle. (b) A ray-tracing schematic of the telescope optics. The focus created by the primary and secondary mirror is reimaged by the cold re-imaging optics to the focal plane.

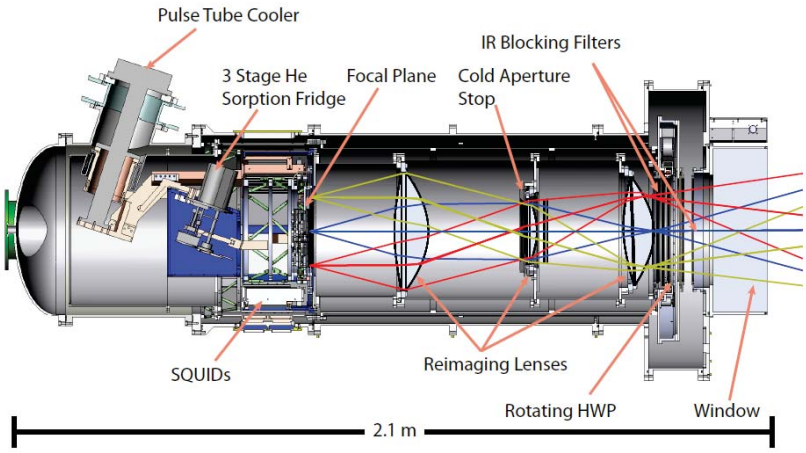

Figure 3.3: A cross-section drawing of the POLARBEAR receiver with components indicated. [61]

cryogenic components. These specific filters were developed at Cardiff University [3].

Polarization Modulation

POLARBEAR uses a combination of sky rotation and a rotating HWP located on the sky side of the receiver to modulate the polarization of the incoming photons. The HWP is machined from a single-crystal sapphire disk, coated with an anti-reflective material to mitigate the generation of undesirable signals from its surface. To minimize its contribution to the systems overall heat budget, the HWP cools via a thermal link to the PTC. Continuous rotation of the HWP allows any signal produced by non-idealities in the instrument to be removed [56], thus improving the overall systematic error.

Cold Reimaging Optics

To efficiently couple the curved focus of the telescope to the planar detection array, an optical chain consisting of three, corrective imaging lenses is integrated in the receiver. Each lens is fabricated from ultra-high molecular weight polyethylene (UHMWPE) and cooled to 6K to reduce thermal emission. Similarly to the HWP, the lens surfaces are coated with an anti-reflective material. The optics are designed to provide the telescope with a 2.3 degree diffraction limited field-of-view for a 19 cm focal plane.

3.4.3 Focal Plane Architecture

Overview

The POLARBEAR focal plane consists of an array of 1274 antenna-coupled bolometers [74] located on 7 hexagonal sub-arrays, each fabricated from a 4" silicon wafer and cooled to 0.25 K. Every detector employs a novel design whereby several features are integrated into a single pixel. Each pixel contains a contacting lens, dual-polarization antenna, "on-chip" frequency filter and a superconducting detector for each of the orthogonal polarization states. Since this configuration is sensitive to both polarization states it is possible to make polarized maps.

Radiation that is incident on the focal plane is coupled from free-space to the antenna by a synthesized elliptical silicon lenslet. The dual-polarization antenna then separates the signal into its orthogonal polarization states before transmitting the individual signals along a pair of superconducting, microstrip waveguides. Spectral band pass filtering, which allows only the desired frequencies to pass, is accomplished "on-chip" by placing a tuned resonant circuit in-line with the microstrip transmission line. This line is terminated by a load resistor that dissipates the optical signal power on a thermally isolated island. An AC biased TES thermistor located on the island is then used to detect the amount of dissipated power by registering a change in the current passing through it.

An image of the POLARBEAR focal plane is shown in 3.4.

Antenna

To achieve dual-polarization sensitivity, the detectors use a dual-slot, dipole antenna [25] directly coupled to the contacting lenslet. The role of the lenslet is to efficiently couple the incoming radiation from the telescopes diffraction-limited optics to the microstrip transmission line. This is accomplished by increasing the directivity of the antenna. Geometrically, an elliptical lenslet fabricated from a dielectric material would provide the desired optical properties. However, the degree of difficulty inherent in machining an ellipse with the required precision in eccentricity precludes this solution. Instead, Polarbear uses a combination of a hemi-spherical lens and a spacer, both made from single-crystal silicon, to synthesize the desired ellipse. This type of configuration has been implemented successfully for a variety applications [38, 88, 122, 38, 42] and posses many beneficial properties.

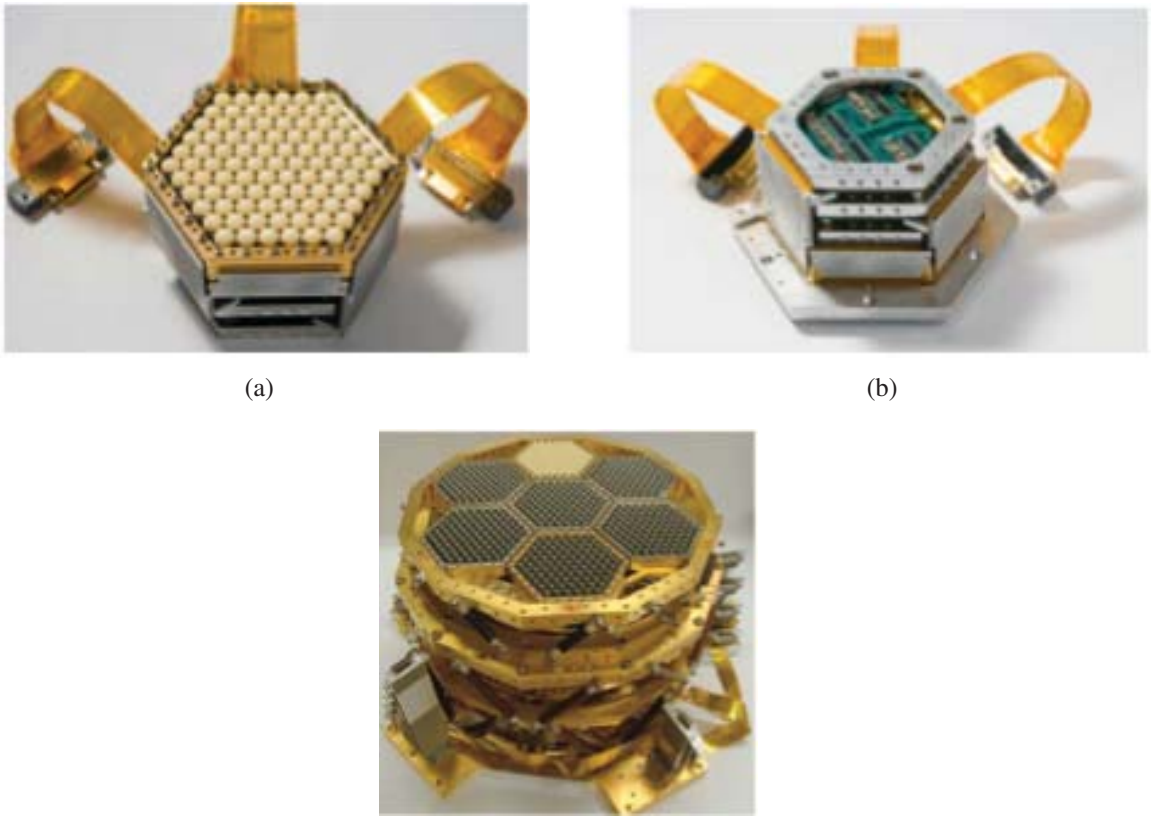

(a) (b)

(c)

Figure 3.4: (a) A single sub-array shown from a sky view perspective. The readout wiring can be seen folding behind the array. (b) A single sub-array shown from a readout view perspective. In addition to the readout wiring, the LC boards can be seen in this image. (c) A picture of the POLARBEAR focal plane. Shown are all 7 hexagonal sub-arrays. The 6 silver sub-arrays use silicon lenslets with Anti-Reflection (AR) coatings, while the single white array uses alumina lenslets, a material with similar optical properties to silicon. The structure extending from behind the array provides both thermal isolation and structural support for the array assembley.

The dielectric lenslet works by acting as a beam-forming element. Without it, rays emanating from the planar antenna would produce a broad Gaussian beam in free space [38]. By placing the lenslet above the antenna, the beam will be formed preferentially in the direction of higher dielectric constant (i.e. towards the lenslet). The result is an increase in the antennas directivity and a higher gain in the preferred direction by reducing the characteristic beam width of the antenna.

Although there are many benefits, issues do arise when using a material with high dielectric constant. Photons incident on the surface of the lenslet will tend to be reflected, therefore limiting the amount of signal reaching the detector. To mitigate this effect, a quarter wavelength anti-reflective (AR) coating composed of a uniform layer of thermoformed polyetherimide was applied to the hemi-spherical surface.

The dual-slot dipole antenna design provides a dual linearly polarized structure that is sensitive to the polarization of the CMB. Photons that are incident on the antenna are separated into orthogonal polarization components and then coupled to individual microstrip transmission lines.

Superconducting Microstrip

Detection of the B-mode polarization signal is already limited by its inherent faintness, and therefore typical transmission methods result in too much loss for this application. Consequently, it is necessary to seek an alternative solution with a low enough impedance to transmit the electromagnetic energy from the antenna to the bolometers with sufficient amplitude for detection. Superconducting microstrip prove to be the ideal candidate, providing minimal loss during transmission.

Photolithography was used for on-chip fabrication of the microstrip transmission line. Three separate layers were employed; two with conductive properties and one dielectric. The first layer was formed by depositing niobium on the silicon wafer substrate, creating a continuous ground plane. An intermediate dielectric layer, composed of silicon dioxide, was then applied to separate the ground plane and the subsequent niobium layer, from which the thin conductive transmission lines were formed.

Niobium was chosen for its low loss properties up to roughly 700 GHz (well above the operational range of the TES detectors) and its high superconducting transition temperature of 9.2 K. In addition, the fabrication process was simplified by using a single element superconductor, instead of using metallic compounds.

Band Defining Microstrip Filters

Traditionally, mm-wave receivers used a relatively large metal-mesh filter to limit the range of frequencies reaching the detectors. They were mounted in front of the imaging elements and posed constraints on the development of larger arrays. The frequency-specific nature

of the filters also hindered the ability to move to multichroic focal planes. Although the antenna used in our application acts to partially define the bandwidth of the detector, the use of a microstrip transmission line enables these off-chip components to be eliminated. Instead, a band-defining filter can be integrated directly into the microstrip to provide enhanced control over the system's bandwidth.

Bolometers

To achieve the high sensitivity necessary to detect the faint B-mode polarization signal, the POLARBEAR focal plane uses a large imaging device similar to the CCD array used in modern digital photography. The key difference lies in the type of detector being used, namely the bolometer. Observations in the far-IR to mm wavelength commonly employ this type of device due to its high sensitivity in these wavelengths. Bolometers are fabricated using standard, optical lithographic techniques and pair well with SQUID technology, which has a large enough bandwidth to ultimately allow the readout signals to be multiplexed [118, 66]. This results in a detector technology that is scalable to large arrays, a fundamental requirement to increasing the detection sensitivity. Current bolometer development has reached the point where it is the statistical fluctuations in the CMB photon arrival rate that limits the system's noise performance, not the intrinsic detector properties. The use of larger arrays also enables higher mapping speeds.

A bolometer is a sensitive detector of electromagnetic radiation. It uses an absorbing material, with heat capacity (C), connected to a heat reservoir via a weak thermal link (G). The absorber is subject to a combination of electrical power intended to bias the detector (P_{bias})and the signal power incident from the desired photons (P_{opt}). Detector biasing at this stage enables the TES to be adjusted mid-way into its superconducting transition where maximum sensitivity is achieved. This yields a temperature of:

$$T = T_0 + \frac{P_{bias} + P_{opt}}{G} > T_0 \tag{3.1}$$

Assuming that the bias power remains constant while the signal power changes, the bolometer will register a change in temperature that can be detected by a thermistor in close thermal contact. It is desirable to use a thermometer material in which the resistivity will change significantly with slight variations in temperature. As a result of the high degree to which this condition is met when superconductors are held in their transition,

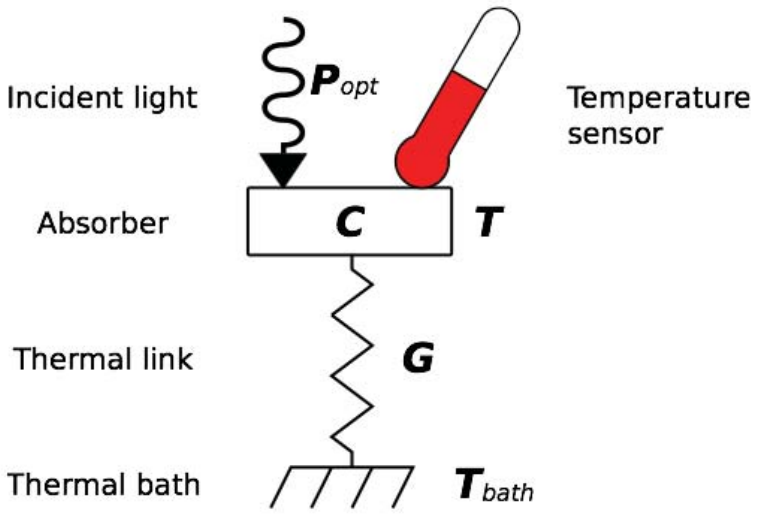

Figure 3.5: Simple bolometer.

they present an ideal choice for this type of application. In this critical regime, a small change in temperature yields a large change in resistance.

Bolometers operate in one of two modes: current biased or voltage biased. Each configuration presents individual strengths and weaknesses. Classically, all bolometers were biased with a constant current and the resistance was found by conducting a voltage measurement. The benefit of this being that the voltage can easily be amplified. In recent years, the advent of SQUID amplifiers has made the use of voltage-biased bolometers feasible. In this mode, the bolometer is supplied with a constant voltage bias and the current is measured. The primary reason for wanting to operate in this mode is the strong electro-thermal feedback (ETF) that the system is capable of exhibiting [68]. In the voltage-biased configuration, an increase of incoming optical power results in an increase to the bolometer temperature. This causes an increase in the resistance, which decreases the bias power. As a result, the feedback compensates for changes in the optical power deposited on the detector, thus keeping the total power and therefore the bolometer's temperature constant.

This electro-thermal feedback is advantageous for a variety of reasons. Since the detector essentially remains in its transition, it is much faster and the use of external feedback systems is not necessary. In addition, the feedback produces a constant ratio between the incident signal power and the amount of power relayed by the detector (i.e. a linear response) for a wide range of incoming power.

The detectors used in POLARBEAR are TES bolometers. This type of detector, which uses a voltage-biased superconductor as the thermistor, is advantageous when detecting a faint signal. Due to the steep temperature dependence of a superconductor operating near its critical transition, even the smallest fluctuations in temperature result in an inherently amplified output. The set-up is such that a weak thermal link is formed between the TES thermistor and the heat reservoir through a silicon nitride suspension. To thermally release the bolometers (a process that is necessary to isolate the component) the silicon substrate is removed below the suspension using a XeF_2 vapor etch. The heat capacity of the bolometer is controlled by depositing a layer of gold on the device. The TES thermistor itself is an aluminum/titanium bi-layer. For this application it is necessary to deposit two separate layers of different materials to control the transition temperature of the thermistor.

Details on the fabrication and optimization of the detection wafers used in POLARBEAR can be found in: [5]

3.4.4 Multiplexing Readout

In moving to large focal plane arrays the issue becomes how to address the wire count spanning from the room temperature electronics to the systems cryogenic stages. Electrical wiring presents a significant source of thermal loading that can easily exceed the available cooling budget of a typical cryogenic fridge. To address this issue, POLARBEAR employs a readout scheme that operates the TES bolometers in concert with a frequency-domain multiplexing module. This is accomplished by biasing each bolometer at a unique frequency, allowing them to be summed prior to the amplification and subsequent readout stage. The process is very similar to the way a radio operates. By separating the signals in frequency, the wire count can be reduced by sending the bias frequencies for multiple detectors on a single pair of wires and reading them out on another. In addition to being necessary from a thermal loading standpoint, benefits also arise through the simplification of cryogenic wiring and reduction in overall cost.

The readout of TES bolometers requires the use of both warm and cold electronics. At the cryogenic stage, N detectors are biased and read out using a single frequency-domain multiplexing (fMUX) module. An image of one such module, developed at UC Berkeley, is shown in figure 3.6. Each TES bolometer (R_{bolo}) is wired in series with a resonant circuit formed by an inductor and a capacitor. Since the inductor used in each circuit is

identical, the capacitor sets the resonant frequency. A series of N fixed amplitude carrier bias currents are generated at room temperature and transmitted to the bolometers on a single pair of wires. The circuit then chooses the appropriate bias current that has been tuned to match its characteristic resonant frequency. Since relatively high resistance wiring inhibits the ability to apply a voltage bias directly to the bolometers, an external, constant bias current is delivered to a shunt resistor within the 4 K chamber. The resistor value is chosen to be considerably less than that of the TES bolometer, thus providing a constant voltage bias to the bolometer.

Sky signal is read out from symmetric sidebands above and below the carrier frequency. Encoding of the signal into the carrier side bands is a result of optical power altering the resistive properties of the bolometer, thus amplitude modulating the current flowing through the detector. Since the signal from each TES bolometer sits at a unique location in frequency space, they can be summed together before being sent to a series array SQUID operating at 4 K. The role of the SQUID is to provide a pre-amplification stage for the current signal from the voltage-biased TES bolometers. The SQUID is wired in series with the detectors and acts as a very sensitive ammeter, by converting the current flowing through its low-impedance input to a magnetic flux using an inductor coil. The magnetic flux produces a voltage across the SQUIDs Josephson junctions, which is then transmitted to the room temperature electronics for further amplification by a standard operational amplifier.

To ensure a linear response over the entire working region, the readout system operates in a feedback mode, referred to as a shunt feedback flux-lock-loop (FLL) [71]. This keeps the SQUID amplifiers at their maximum transimpedance (dV/dI). By shunting the output of the room temperature operational amplifier (op-amp) back to the input coil of the SQUID, it is possible to zero the current through the input coil and create a 'virtual ground'. This solution is far more desirable than using a separate coil to try to zero the flux directly for the feedback. Once the feedback loop is locks at the flux operating point of the SQUID, it acts to cancel any current attempting to flow through the input coil. Since the voltage output of the op-amp is proportional to this current, it is possible to realize a measurement of the bolometer signal. Due to the large bandwidth of the SQUID (approx. 1 MHz), the FLL does not have enough loop gain to zero the current for all channels over the entire range. To address this issue, a separate feedback mechanism is used in conjuction with the FLL to null the carrier currents, thus reducing the dynamic range requirement of the loop.

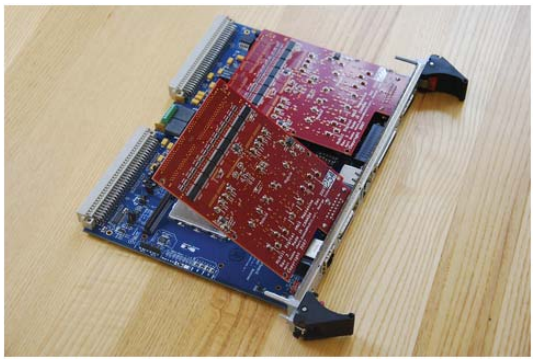

(a)

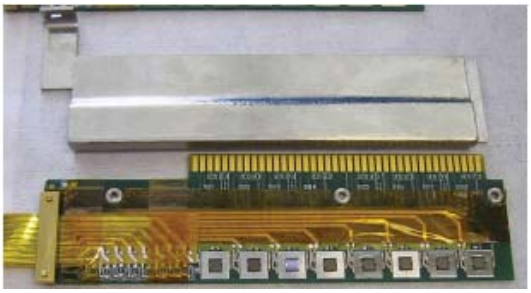

(b)

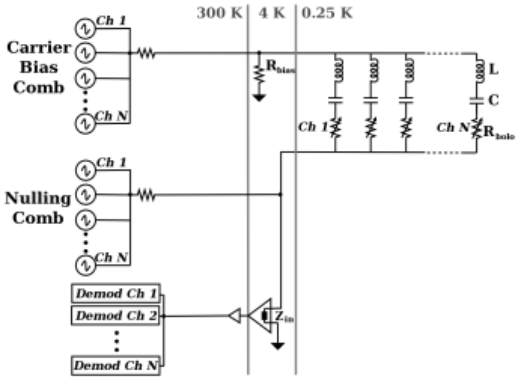

(c)

Figure 3.6: (a) Photograph of a single DfMUX module, consisting of a motherboard (blue) mounted with two mezzanine boards (red). (b) Photograph of a SQUID readout board used for signal amplification at 4K. Shown are eight NIST SQUID series arrays mounted on a Niobium film. The Cryoperm enclosure used for magnetic shielding is pictured above the board. (c) Diagram of the frequency-domain multiplexed readout for N TES detectors.

For more details on the fMUX readout development see: [31, 29, 30, 67]

3.5 Current Status of Polarization Measurements

Many experiments, such as WMAP [98], BICEP [59], and QUIET [32] have already observed the E-mode polarization signal and the results are all consistent with the predicted lambda cold dark matter model of cosmology. Figure 3.7 shows the predicted sensitivty of both POLARBEAR and Panck to the theoretical E and B-mode polarization spectra.

The B-mode polarization signal has commonly been referred to as the smoking gun for inflation, since its detection would support the existence of primordial gravity waves

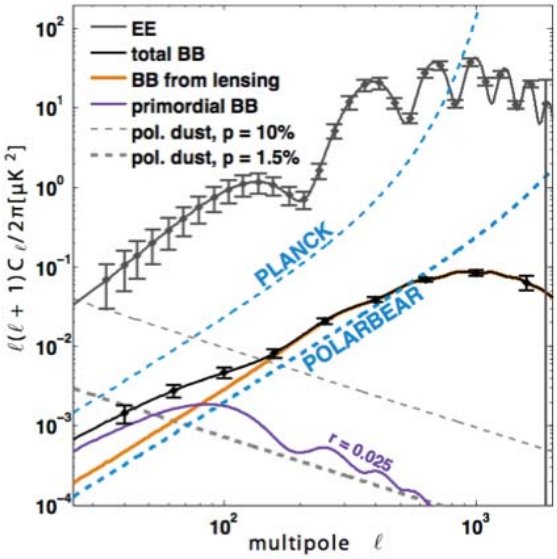

Figure 3.7: Predicted error bars of the POLARBEAR experiment shown with theoretical E and B-mode polarization spectra assuming r=0.025

believed to have been produced from a brief period of rapid expansion.

Although the B-mode polarization signal remains relatively unconstrained, current experiments such as BICEP2 [19], SPTpol [6], Planck [106] and POLARBEAR have been able to constrain the tensor-to-scalar ratio $r < 0.11$ [73]. To date, no experiment has been able to detect the primordial B-mode signal predicted to have originated from the interaction between the CMB and gravitational waves. However, leakage of the E-mode signal into B-mode signal has recently been detected by both the SPTpol and POLARBEAR experiments. The result, which is due to gravitational lensing of the CMB polarization by large-scale structure, manifests itself as a distortion in the polarization spectrum and is consistent between the two experiments.

3.6 Results

Polarization data collected from POLARBEAR has enabled the detection of lensing signals through two different processes. The first was a parallel process to one carried out by the SPT experiment and used a cross-correlation with Cosmic Infrared Background (CIB) maps from the Hershel $500\mu m$ H-ATLAS survey [26]. From the cross-spectra, evidence for gravitational lensing of the CMB polarization with a statistical significance of $4.0 - \sigma$ and evidence for the presence of a lensing B-mode signal at a significance of $2.3 - \sigma$ was

obtained [1]. The results of this cross-correlation are unique in that they are not biased by instrumental and astrophysical systematic errors. To confirm this, a series of null-tests, checks with simulated and real data, and analytical calculations were performed. This measurement of polarization lensing signifies an initial step towards a powerful new probe of both cosmology and astrophysics. However, of particular interest to this work was the reinforcement it provided for the second measurement made by Polarbear via an auto-correlation process. The latter technique used a 4-point correlation function to provide an independent detection of the lensing B-mode.

The second publication [2] represents the first detection made with CMB polarization data alone. A complete explanation of the data analyses carried out on the raw observations and map-making process can be found in [2]. For the purposes of this work, only the key steps will be presented. The initial step in characterizing the effects of gravitational lensing will be to generate polarization maps and then from these maps, calculate the power spectrum of the lensing deflection field.

The map generation process begins by filtering the time series data from the bolometers to remove those affected by spurious instrumental and environmental effects. Orthogonal polarization channels from each pixel are then summed or differenced to derive the Stokes parameters (I, Q, and U), which represent the temperature and polarization data respectively. These data are then co-added into maps and the Q/U maps are transformed into E/B-mode maps.

By applying the two estimators in equations 1.6 and 1.7 to the co-added maps it is possible to reconstruct the lensing field. The Fourier coefficients (C_l^{EE}, C_l^{BB}, $\tilde{C}_l^{EE}$) and theoretical deflection power spectrum used in these estimators are calculated using the CAMB (Code for Anisotropies in the Microwave Background) software [69]. Due to the requirement that B-mode information be included when calculating the power spectrum, there are two estimates of the lensing power spectrum: $< d_{EE} d^*_{EB} >$ and $< d_{EB} d^*_{EB} >$. The first is referred to as the cross-lensing estimator and is free from the Gaussian bias. The second is not and requires a removal of this bias. The unbiased, reconstructed lensing power spectrum is calculated as follows:

$$C_L^{dd} = (< d(\mathbf{L}) d^*(\mathbf{L}) > - N_L^{(0)})/T_L \tag{3.2}$$

Where the Gaussian bias $N_L^{(0)}$ and the transfer function T_L are calculated using simulations.

Under the assumption that the CMB polarization is indeed lensed, the two lensing estimators make a correlated measurement of the lensing power spectrum. The two lensing estimators are combined using correlation information derived from Monte Carlo simulations and simulated lensing reconstructions for each lensing estimator, for each patch.

The polarization lensing power spectrum measurements for each of the three POLARBEAR patches and the two B-mode estimators $< EEEB >$ and $< EBEB >$ are shown in figure 3.8. The uncertainties in these band-powers do not include sample variance. Figure 3.9 shows the patches co-added, and the estimators $< EEEB >$ and $< EBEB >$ combined.

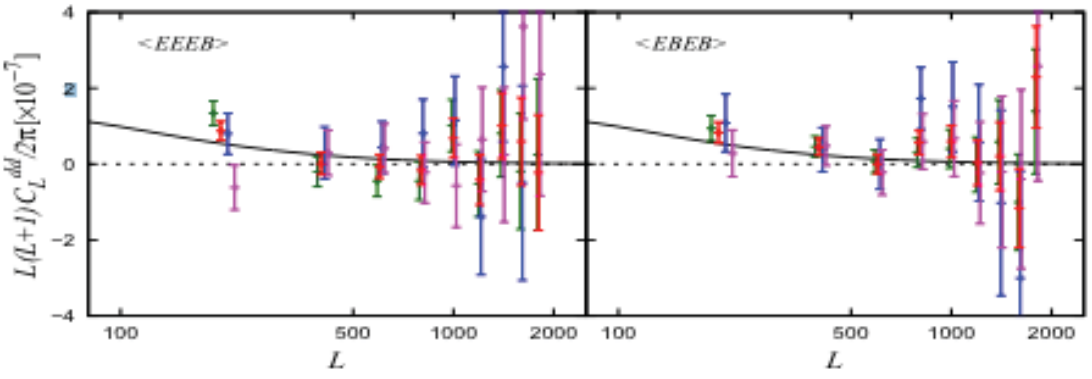

Figure 3.8: Measured polarization lensing power spectra for each of the three POLARBEAR patches, for both lensing estimators $< EEEB >$ (left) and $< EBEB >$ (right). The lensing signal predicted by the CDM model is shown as the solid black curve. The measured lensing power spectra are shown for each patch in dark green (RA23), blue (RA12) and magenta (RA4.5), respectively and are offset in L slightly for clarity. The patch-combined lensing power spectrum is shown in red. [2]

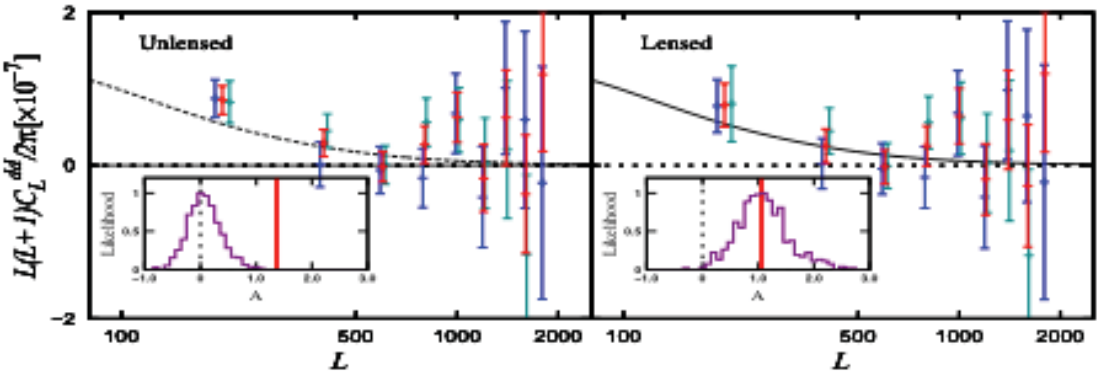

Figure 3.9: Polarization lensing power spectra co-added from the three patches and two estimators are shown in red. The lensing signal predicted by the CDM model is shown as the dashed black curve in the left panel and the solid black curve in the right panel, respectively. The polarization lensing power spectrum $< EEEB >$ is in blue and $< EBEB >$ dark green. Left: A 4.2-σ rejection of the null hypothesis of no lensing. Right: The same data, assuming the existence of gravitational lensing to calculate error bars, including sample variance and including the covariance between $< EEEB >$ and $< EBEB >$.

3.7 Deployment

To accommodate both the operation and maintenance of the POLARBEAR experiment, the telescope requires a variety of personnel to be on site. During typical observing conditions, the personnel complement consists of a systems engineer and a technician, along with one or two scientists. This number varies depending on the workload, peaking during periods when new hardware is being installed and tested.

A combination of professors and graduate student researchers from the collaborating institutions are tasked with staffing the scientist positions. Deployment is scheduled on a rotation basis during which individuals will progress from a novice observer ('trainee') to expert observer ('trainer'). The role of the trainee is to provide basic support to the project while learning as much as possible from the expert observer. By the end of the training period the trainee is capable of running the daily operations (i.e. observing scripts and general software/hardware debugging) at both the high altitude observing site and the off-site control station.

Shortly after POLARBEAR achieved first light, I deployed to the Chilean project site along with other members of the experiment to prepare for the first season of observations.

In contrast to many of the mature experiments located in the Chilean Andes that can be operated remotely from a low-altitude location, running POLARBEAR involved regular trips to the high-altitude observing site. A typical day in the field would begin by checking the current weather observations and weekly forecast for high winds and precipitation. To safely operate the telescope, winds had to be less than a threshold value (sustained wind ¡ 27 m/s) determined by the mechanical properties of the telescope structure and no measurable amounts of precipitation could be forecast. Once it was verified that the telescope could be safely operated, the next step was to check the perceptible water vapor (PWV) content of the atmosphere. To collect science quality data, this value had to be less than 4 mm. If it was determined that the PWV condition was met and normal operations could proceed, observations were queued on a dedicated control computer.

Observations were commonly scheduled for a 36-hour time period beginning with cycling the helium sorption fridge. During this process the detector stage would be warmed above the transition temperature of the TES bolometers and then cooled back down to a base temperature of 0.25 K. After the fridge cycle was completed, the detectors were tuned to lie in the steep part of their transition by slowing adjusting the incident bias power to lower the temperature of the bolometers.

After the detector tuning procedure, the next step was to characterize the bolometer response (change in current) to a given source. This was accomplished by scanning planets with well-known properties. However, since planets were not always available for observation, the bolometers were also subject to a local source of radiation to calibrate the temperature of the sensor, called a stimulator. Following these calibrations, a series of elevation nods were performed to characterize the effect of changes in the atmospheric loading on the bolometers.

Once all of the tuning and foreground characterization processes were complete, observations of the CMB could begin. These science scans consisted of observing the three patches outlined in section 3.3 at a constant elevation, with the telescope only adjusting in elevation once the patch moved out of its FOV.

As an observation leader trainee, I was responsible for everything from checking the initial weather conditions and forecasts to queuing the observing scripts when operating in a normal mode. This role was essential as a link between members in the field and those providing support remotely.

The most important responsibility of this role was to continuously monitor the current state of the telescope to verify that the cryogenics were performing correctly, the detector yield was within reason, the telescope was responding to the commands sent by the scripts and therefore positioned correctly, and checking that data was being outputted and stored correctly. To monitor these conditions a webpage was setup to stream and record outputted data in real time. In the event that an issue did arise, it was necessary to notify the rest of the team and respond immediately. There were several instances in which critical errors occurred during the middle of the night that required driving to the high-altitude observing site for attention.

In addition to regular observing duties, there was a list of tasks that needed attending to when time permitted. Since I deployed very early on in the project, I was involved in many of the action items necessary to prepare the experiment for the first observing season. Examples of my contributions include the following:

- I worked in a small group tasked with performing photogrammetric and theodolite measurements of the telescopes reflectors to ensure alignment between the primary mirror, secondary mirror and the telescope. In response to these measurements, the receiver was repositioned. The alignment process was an iterative one that involved making minor adjustments using precision-machined shims, followed by more measurements to verify the accuracy of the positioning.

- I installed a CCD camera on the boom of the telescope that was developed at UCSD to take optical images of planets, stars, and galaxies to help position the telescope on the sky.

- I worked with the technicians to install shielding around the primary mirror of the telescope to reduce the signal from unwanted sources that were showing up in the data.

- I helped install a prototype dielectric sheet calibrator (DSC), which uses a rotating dielectric sheet to measure polarization orientation. More details on this system can be found in [105].

- As a consequence of the low oxygen levels at high altitude, it was necessary to create an oxygenation system for the control center. This project proved to be more of

a challenge than initially thought due to the oxygen concentrator units that were purchased for this purpose not working at high altitude. I worked on modifying these units, eventually operating them in a series configuration that allowed them to work under the unusual atmospheric conditions.

- Due to the harsh weather environment at the site, the telescope needed to be electrically grounded against lightening strikes. I worked on creating a conductive pathway that was favorable for the lightning and was electrically isolated from the sensitive parts of the telescope.

- I worked on modifying the observing scripts as necessary to maximize the time spent scanning the CMB patches and to account for changes in the availability of calibration sources on the sky. This also involved working closely with members of the data analysis team to ensure that the quality of the science data was maximized.

- Since the atmospheric conditions change with the time of the year, the amount of loading on the bolometers from the atmosphere also changes. To account for this, it was necessary to modify the fridge tuning script to maximize the hold time. I was involved in this procedure on multiple occasions.

- I helped install the HWP and implement new scripts to characterize its operation.

- I also participated in the daily task of refueling the generators with diesel.

- I continue to participate in a series of weekly teleconferences between the personnel at the site and the rest of the project. These are designed to address any issues and keep everyone informed of the day-to-day operations.

Inherent to any project in its initial stages was the need to address many unforeseen issues. Due to the remote location of the experiment, this required the use and modification of the sometimes very limited local resources. This next section will outline some of the specific issues that I was involved in while deployed.

One of the most critical parameters to monitor was the cryogenic refrigerator performance to verify that the bolometer array was operating at an ideal temperature. One afternoon, during a normal observation cycle, I noticed a 10-PSI drop in one of the compressed helium lines that feed the pulse tube cooler. This prompted an in depth test for leaks in the

helium lines that run throughout the telescope. The issue was found to have resulted from the lines being exercised beyond their maximum dynamic radius when moving through a cable wrap located in the base of the telescope.

Over the next few days I took preventative measures to try and minimize the leak and start observing again. This involved proposing a solution to fill the empty space in the cable wrap to limit the maximum bend radius, temporarily repositioning the pressurized lines to minimize their dynamic radius of curvature and recharging our pulse tube system to bring it back to normal operating conditions. My role in this process was to perform the leak tests, recharge the pulse tube system with helium and help design the structure to be installed in the base of the telescope. The latter involved me producing a computer-aided design (CAD) model and drawings of the structure for presentation to the collaboration and the fabrication company.

On another occasion, I worked with members from both the site and remotely to debug an electrical issue that prevented the control computer from being able to command the telescope. My role involved electrical testing of various circuit components on the telescopes central control unit (CCU) to determine where the signal was being interrupted. The issue was found to be a chip that had been destroyed in one of the amplifying circuits during a severe lightning storm at the site. Since a new chip had to be ordered and shipped to the site, I worked on creating a temporary solution with components that were available at the site. Once the new chips arrived and were installed, I worked on replacing all the copper connections to the CCU with optical fiber to prevent further damage.

3.8 Polarbear-2 Project Overview

POLARBEAR2 will consist of a receiver upgrade to the current POLARBEAR project. The instrument is planning on being deployed in late 2014 and will contain several improvements over its predecessor, most notably in detector technology. To increase the overall sensitivity, a focal plane containing 7588 Al-Ti TES bolometers with multi-chroic (i.e. multiple wavelength) capability will be mounted on a telescope identical to the HTT. A sinuous antenna will allow the array to simultaneously collect signal over a two-octave band with observing frequencies centered at 95 GHz and 150 GHz. On-chip filter banks will then separate the broadband signal into multiple frequency bands, each to be detected by a separate bolometer. The implementation of such a system will enable POLARBEAR to

(a)

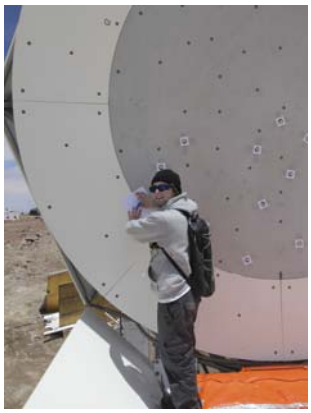

(b)

(c)

Figure 3.10: (a) Installing electrical ground for lightning protection. (b) Installing photogrammetry targets for receiver alignment. (c) Modified oxygen concentrator set-up.

be sensitive to an r of 0.01 at a 95% confidence level.

A more detailed description of the experiment can be found in [108].

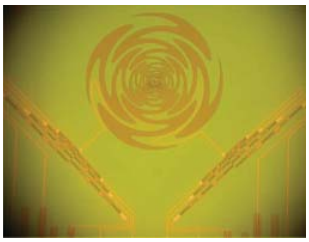

(a)

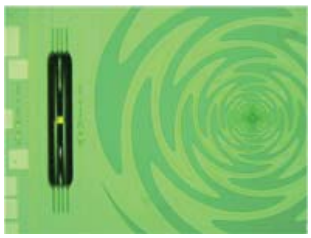

(b)

(c)

Figure 3.11

Chapter 4

A survey of gas and dust in $z > 2$ protoclusters [II]: the SEDs and gas-to-dust ratios in galaxies lying at $z = 2.84$ in the H1549+19 field

The format of the following sections is that of a paper to be submitted for publication in the Monthly Notices of the Royal Astronomical Society (MNRAS) journal. Therefore I have included sections regarding work carried out by my collaborators (i.e. *S.C. Chapman, M. Gurwell, M. Aravena, A.W. Blain, J. Geach, R.,J. Ivison, N. Reddy, Ian Smail, C.C.Steidel*), such as the data reduction and map-making processes, for the purpose of completeness. I joined this project at a high-level to gain some experience analyzing submm wave data and my contributions are outlined in section 4.3.

Abstract

High-resolution interferometric imaging data of the core regions of the protoclusters in the H1549 field ($z = 2.84$) and the H1700 field ($z = 2.30$) is presented. The observations are made at $\sim 870\ \mu m$ with the Submillimetre Array (SMA), following deep SCUBA2 maps of these fields. Our high-resolution submm imaging clearly detects at least three galaxies, and possibly a fourth, in continuum at $\geq 4\ \sigma$ as single compact (size ≤ 2 arcsec or ≤ 16 kpc) point sources with an absolute position to $\sim$ 0.4-arcsec accuracy. These sources are clearly associated to known $CO(3-2)$ line emitters in the H1549 field, identified in our blind survey of this overdense region. At these redshifts, the $24\ \mu m$-to-submm flux density ratios suggest that all of these protocluster galaxies have Arp 220-type spectral energy distributions (SEDs) dominated in the far-IR by starbursts. However, Q1549 has an exceptionally large $24\ \mu m$ (rest-frame $\sim 5-6\ \mu m$) luminosity, exceeding the expected value given the star formation rate (SFR) inferred from far-IR observations. This result is consistent with a hot dust torus around the quasar. Gas-to-dust ratios are measured for all CO-emitters identified in the protocluster, with a median of 143 in solar units, and a dispersion of only 39, dominated by the outliers, MD17 and MD12. High apparent gas-to-dust ratios (> 150) can indicate the bulk of dust mass is cold in some of the objects, while the tight gas-to-dust ratio found overall can be used to argue for a constant conversion between CO and H_2 gas mass. The CO and submm continuum maps in the core region of H1549 have helped to reveal how the large cold gas reservoirs, yet typical gas to dust ratios is likely driving the reversal in the SF-environmental density relation found in high$-z$ protoclusters. This complex mix of star-formation and AGN activity in multi-component sources may be common in the high redshift ultraluminous galaxy population, and highlights the need for precise astrometry from high resolution interferometric imaging for a more complete understanding.

4.1 Introduction

A key goal of modern cosmology is to understand how gravitationally bound structures, namely galaxies and galaxy clusters, and their constituent star populations formed from an initially uniform gas and how they have evolved since then. To answer this question, cosmologists seek to obtain data from all observable wavebands, and in combination with numerical simulations, attempt to derive a solution.

Recent advances in IR/mm-wave detector technology over the past decade enable field surveys to be wider and deeper than previously thought feasible at these wavelengths (e.g. [24, 111, 50]) and open a new window into the distant Universe. A result of this advancement is the discovery of a cosmologically significant population of high-redshift, highly star-forming galaxies that are bright at submillimetre (sub-mm) wavelengths. These sub-mm galaxies (SMGs) exhibit far-infrared luminosities on the order of 10^{12} - 10^{13} $L_{\odot}$, implying enhanced star formation rates of 10^{3} $M_{\odot}$/year [24] and as a result, tend to be heavily enshrouded in dust. Therefore observations at these wavelengths provide insight into properties that are not readily discernable at optical wavelengths, such as star formation activity at high-redshift ([16]). Another benefit of performing studies at these wavelengths is that the shape of the redshifted spectral energy distribution (SED) counteracts the effect of the increasing luminosity distance to provide an unbiased view of dust obscured star formation out to high redshift ([120, 17]). Therefore, distant dusty galaxies play a key role in developing an unbiased understanding of star formation and galaxy evolution over a wide range of redshifts.

Initial studies at these wavelengths were made feasible by the commissioning of the Submillimetre Common User Bolometer Array (SCUBA) [49] camera located on the James Clerk Maxwell Telescope (JCMT) in Hawaii. More detailed studies using these types of instruments have been hindered by their poor resolution, which was coarser than the sub-arcsec resolution of optical and near-IR cameras. As a result, there was a high degree of ambiguity in the multi-wavelength counterpart identification. It was not until deep radio continuum surveys were performed, which allowed radio and submm emission to be correlated [53, 52], that follow-up optical and CO spectroscopy [22, 23, 104, 103] was possible. This confirmed that the SMGs lie at high-redshift and are mostly young, gas rich galaxies undergoing major mergers [120]. CO spectroscopy has the additional benefit of line measurements which are useful in determining physical conditions within the galaxy and allow

for an absolute identification of a source by tying together the optical and submm redshift at the position of the galaxy [23].

Even though the radio-submm association is regarded as applying at high-z, and the near/mid-IR imaging allows for the determination of submm counterpart identification, each comes with an inherent bias and therefore leaves some ambiguity in source identification. It is therefore necessary to observe these sources using high-resolution interferometery. This is currently made possible by sensitive interferometers such as the Submillimetre Array [48], the Plateau de Bure Interferometer (PdBI), and the Caltech Millimeter Array (CARMA) which provide an order of magnitude sensitivity over single dish experiments and permit unambiguous identification of multi-wavelength counterparts [121].

As a result of being selected at 850 μm, SMGs have the intrinsic property that they contain both large cold dust masses [72] and significant molecular gas reservoirs (10^{10} $M_{\odot}$; [43]). Observations of this cold molecular phase in the interstellar medium (ISM) can elucidate questions such as what drives these extremely luminous systems and provides unique insight into their physics and behavior.

Understanding the dust properties of a galaxy and the associated absorption and emission process is essential since some fraction of the stellar energy output will be absorbed and re-radiated in the mid-IR to millimeter wavelength range [64]. This will determine the shape of the galaxies Spectral Energy Distribution (SED).

The ability to address the evolution of molecular gas content with redshift has been historically limited by poor redshift coverage. It is not until recently that studies (e.g. [18]) attempted to address this issue. Measuring the evolution of molecular gas density is important since it will help elucidate the process of star formation in galaxies. To accomplish this, it is beneficial to compose a sample that is free from selection biases, and perform blind surveys of the sky. This allows the molecular gas content in a CO flux limited sample to be measured as a function of redshift and luminosity (e.g. observations in the local Universe and simulations by [60, 77, 76, 65, 40]). With the advent of sensitive interferometers such as the SMA, PdBI, ALMA, and CARMA, these type of studies are now possible.

Current observations and simulations suggest that there has been a strong evolution in the molecular gas fractions in star-forming disk galaxies at $z = 1 - 2$ compared to similar objects at $z < 0.5$ [41, 4] However, the gas supplies, star formation efficiencies, and starburst modes (merger driven versus quiescent disk) may vary significantly as a function

of their local density. Galaxy evolution should be accelerated in regions of strong overdensity. Recent work with *Spitzer* and *Herschel* has demonstrated enhanced star formation rates (SFRs), and a reversal of the star formation (SF)-environmental density relation, at z>1.5 in galaxy clusters [34, 35, 110]. Exceptionally high levels of star formation have been found in cluster cores, reaching >2000 $M_{\odot}$/yr Mpc^{-2}. The reversal of the z<1 trend in SF vs environmental density implies that at $z\sim$2 massive cluster galaxies are still forming a substantial fraction of their stars in protoclusters. These high$-z$ protoclusters are where the morphology-density relation may be established.

The following work was derived from a project (the *Galaxy Overdensity Gas Survey*) that was initiated to perform blind surveys of the gas and dust in $z > 2$ galaxy overdensities, or protoclusters, to provide a solid constraint on the evolving CO luminosity function in comparison with the field. A unique aspect of this program was the selection of the protoclusters from the 24 survey fields of the Keck Baryonic Structure Survey (KBSS; [85]), a well calibrated field galaxy survey at $z > 2$. Several of these fields show strong galaxy overdensities (e.g [101, 100]), providing a complete, unbiased census of protoclusters. H1549+19 (Figs. 2,3) contained the strongest KBSS overdensity (at $z\sim$2.84), with over 5 times the typical surface density of Lyman-α emitters (LAEs) found in the field. In fact, it may represent the richest LAE field ever observed, at any redshift.

4.2 Observations and Data Reduction

4.2.1 The H1549 Field

The H1549 field was initially discovered as a result of the Keck Baryonic Structure Survey (KBSS: e.g. [85]), a large spectroscopic survey of continuum-selected galaxies in fields surrounding hyper-luminous ($L > 10^{14}\ L_{\odot}$) quasi-stellar objects (QSOs) between redshift 2.6 and 2.8. This survey was designed to investigate the interaction between galaxies and their inter-galactic medium (IGM). The KBSS observed several fields with strong galaxy overdensities ([100]) that together, represented an unbiased population of galaxy overdensities in a well-calibrated field survey. This specific field is the most dense galaxy cluster known at z>2 from the 24 survey fields of the KBSS (*Chapman et al. 2014, submitted*) and possibly the universe. The proto-cluster region, which lies at a redshift of 2.84, is surrounded by an extremely luminous QSO and was found to have 5 times the surface density

of Lyman Alpha emitters (LAEs) when compared with other fields covered to a similar depth *Chapman et al. 2014, submitted.* Since the radiation field of a QSO in the presence of dense HI gas can induce Lyman alpha emission, this field clearly demonstrated that it was both a very dense and gas rich cluster.

The H1549 field benefits from multiple factors that make it an ideal region to study. As a result of the strong clustering, especially along the line of sight, numerous galaxies can be studied in one instrument pointing. This allows for an experiment that is less expensive in observing time since it typically takes multiple pointings to gain the same amount of information in a less dense region. The combination of the overdensity and the bright QSO also present an ideal climate to study environmental effects, such as the response of the intergalactic medium (IGM) to a source of ionizing radiation greater than that of the UV background [99].

One of the key properties of the H1549 field was the extensive data coverage that ranged from the optical to mm-wavelengths. Observations in the visible band were performed at 0.3-1.0 μm using ground based imaging and spectroscopy available at the Keck Observatory located on Mauna Kea in Hawaii. Infrared data was collected at $4.5\ \mu m$ and $24\ \mu m$ to 5-σ depths of 11.3 μJy and 71 μJy respectively (e.g. [91, 119]) by the Infrared Array Camera (IRAC: [37]) and the Multiband Imaging Photometer for Spitzer (MIPS: [84]) on board the *Spitzer Space Telescope*.

4.2.2 Sample Selection

As a result of the strong galaxy overdensity field found by the optical imaging and subsequent spectroscopy in the KBSS [109], a blind 3mm (230 GHz) search for CO J = 3-2 molecular gas was performed on the $z = 2.84$ galaxies to gain insight into their gas properties. The spectroscopic measurements were carried out by the Plateau de Bure Interferometer (PdBI), a radio interferometer located in the French Alps consisting of 6 antennas with 0.5 arcsecond resolution at the observing frequency of 230 GHz. The PdBI pointing was tuned to redshifted CO(3-2) since this transition had minimal excitation requirements and therefore provided the best illustration of the mass and distribution of star forming gas in a range of galaxy types and luminosities. This study yielded a total of eight sources known to be at $z = 2.84$ with significant CO (3-2) emission line detections, all with an associated optical counterpart (Chapman et al. 2013?) from the KBSS and a potential ninth source

with no optical counterpart. A search algorithm was run on the spectra in this study and was constrained to detect emission lines with a physically reasonable linewidth of 100 to 1000 km/s. The selection criterion was then based on the signal-to-noise ratio (SNR) of the candidate lines which resulted in five line detections with a SNR>5 and three with an SNR>3, yielding a total of 8 strong CO emission sources. Based on similar studies (e.g. [18, 102, 28]), the fraction of galaxies with large CO masses was greater than expected and led researchers to believe that this overdense region is in the process of transforming gas into stars at a tremendously high rate.

4.2.3 SCUBA-2 850 μm Imaging

Observations were conducted in Band 2 weather conditions (τ225 GHz < 0.05) over 7 nights between 23rd January and 20th May 2012 totalling 11 hours of on-sky integration. The mapping centre of the SCUBA-2 H1549+19 field is α = $15^{\mathrm{h}}51^{\mathrm{m}}53.3^{\mathrm{s}}$. A standard 3 arcmin diameter daisy mapping pattern was used, which keeps the pointing centre on one of the four SCUBA2 sub-arrays at all times during exposure. The final map RMS$_{>3''}$ for 850μm is $\sigma_{850\mu\mathrm{m}} = 0.8$ [mJy], while the RMS$_{>3''}$ for 450μm is $\sigma_{450\mu\mathrm{m}} = 5.2$ [mJy] (significantly below the confusion limit of Herschel-SPIRE at 500μm). Refer to Table 1 for position of multi-source detection in other wavelengths.

Map making

Individual 30 minute scans are reduced using the dynamic iterative map-maker of the SMURF package [55, 21]. Raw data are first flat-fielded using ramps bracketing every science observation, scaling the data to units of pW. The signal recorded by each bolometer is then assumed to be a linear combination of: (a) a common mode signal dominated by atmospheric water and ambient thermal emission; (b) the astronomical signal (attenuated by atmospheric extinction); and finally (c) a noise term, taken to be the combination of any additional signal not accounted for by (a) and (b). The dynamic iterative map maker attempts to solve for these model components, refining the model until convergence is met, an acceptable tolerance has been reached, or a fixed number of iterations has been exhausted (in this case, 20). This culminates in time-streams for each bolometer that should contain only the astronomical signal, corrected for extinction, plus noise. The signal from each bolometer's time stream is then re-gridded onto a map, according to the scan pattern, with

the contribution to a given pixel weighted according to its time-domain variance (which is also used to estimate the χ^2 tolerance in the fit derived by the map maker).

The sky opacity at JCMT has been obtained by fitting extinction models to hundreds of standard calibrators observed since the commissioning of SCUBA-2 (Dempsey et al. 2012). The optical depth in the 450μm band was found to scale with the Caltech Submillimetre Observatory (CSO) 225 GHz optical depth as: $\tau_{450} = 26.0(\tau_{225} - 0.0196)$. Note that this scaling is slightly different from the original SCUBA relations (see Archibald et al. 2002; Dempsey et al. 2012).

Filtering of the time-series is performed in the frequency domain, with band-pass filters equivalent to angular scales of $2'' < \theta < 120''$ (i.e. frequencies of $f = v/\theta$, where v is the scan speed). The reduction also includes the usual filtering steps of spike removal ($>10\sigma$ deviations in a moving boxcar) and DC step corrections. Throughout the iterative map making process, bad bolometers (those significantly deviating from the model) are flagged and do not contribute to the final map. Maps from independent scans are co-added in an optimal stack using the variance of the data contributing to each pixel to weight spatially aligned pixels. Finally, since we are interested in (generally faint) extragalactic point sources, we apply a beam matched filter to improve point source detectability, resulting in a map that is convolved with an estimate of the 450μm beam. The average exposure time over the nominal 3 arcminute daisy mapping region (in practice there is usable data beyond this) is approximately 10 ksec per $2'' \times 2''$ pixel.

Flux calibration

The flux calibration of SCUBA–2 data has been examined by analysing all flux calibration observations since summer 2011 until the date of observation. The derived beam-matched flux conversion factor (FCF) has been found to be reasonably stable over this period, and the average FCFs agree (within error) to those derived from the subset of standard calibrators observed on the nights of the observations presented here. Therefore we have adopted the canonical calibration of $\mathrm{FCF}_{450} = 540 \pm 65\,\mathrm{Jy\,beam^{-1}\,pW^{-1}}$ here. A correction of $\sim$10% is included in order to compensate for flux lost due to filtering in the blank-field map. This is estimated by inserting a bright Gaussian point source into the time stream of each observation to measure the response of the model source to filtering.

4.2.4 SMA 890 μm Imaging

As a result of the SCUBA-2 instruments large beam size, it was necessary to perform follow-up interferometery with the SMA to resolve the 850-μm emission. The SMA observations were performed in three tracks using the compact array conguration at 345 GHz (full bandwidth ~ 4 GHz from the combined sidebands) on March 01 and March 29 2013. A synthesized beam size of $\sim$2 arcsec was achieved using all eight antennas, with baselines ranging from 16 to over 76-meters. The weather was generally excellent ($\tau_{225\mathrm{GHz}} \leq 0.08$), with a typical rms noise level of 0.8 mJy per track with a total of 18 hours of on-source integration. The phase reference of the array was set using the position . The visibility data were reduced and calibrated using the mir software package [93], modied for the SMA. During the reduction, visibility points with clearly deviating phases and/or amplitudes were flagged. Complex gain calibration was performed using the calibrator sources 1549+026 and 1540+147. The passband calibration was done using available strong calibrator sources, primarily 1924-292. The absolute flux scale was set using observations of the planet Neptune and other sources with stable flux densities such as mwc349a. We estimate a typical flux accuracy of better than 20 $\%$. The calibrated visibility data were then imaged using the miriad software package [92] from which the positions and fluxes of the h1549 sources were derived. Each continuum map was deconvolved down to the 1-σ theoretical rms noise level using the miriad *clean* routine.

4.3 Results

4.3.1 Line luminosities

In this section we present the relevant calculations used in deriving line luminosities.

For the purposes of this paper, we have adopted the derivation for line luminosity presented in [114]. A complete derivation can be found in [97].

A line refers to a specific CO transition (i.e. CO(3-2) or CO(1-0)) and the resulting luminosity can be calculated in one of two forms.

One solution is to calculate the luminosity in terms of $L_{\odot}$:

$$L_{line} = 1.04 \times 10^{10} S_{line} \Delta v \nu_{rest} (1+z)^{-1} {D_L}^2 \tag{4.1}$$

An alternative is to calculate the luminosity in units of $Kkms^{-1}pc^2$:

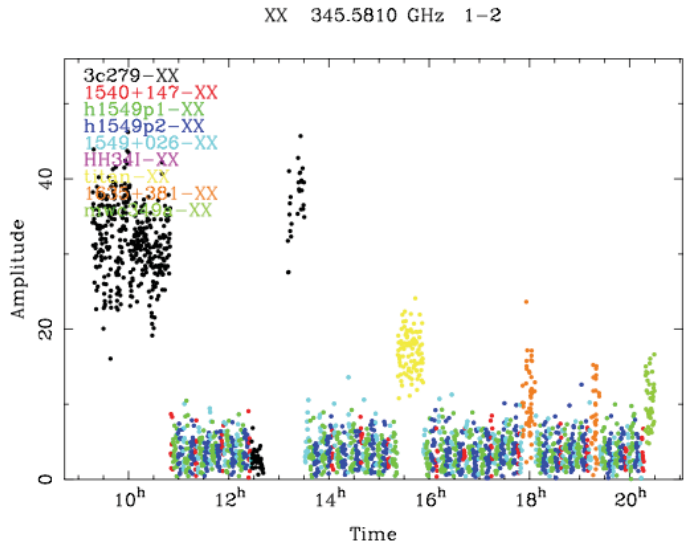

Figure 4.1: Observation Summary: Shown in an example of an observation summary for the combined SMA tracks. A summary is produced for each of the baselines in the configuration and is defined for the upper or lower receiver sideband. The plot shows the amplitude of the observed signal as a function of time for the 3 SMA tracks (green, blue and turquoise) as well as the calibrator sources.

$$L_{line} = 3.25 \times 10^7 S_{line}\Delta v \nu_{obs}^{-2} {D_L}^2 (1+z)^{-3} \tag{4.2}$$

where,

$S_{line}\Delta v$: *velocity integrated flux* ($Kkms^{-1}$)

$\nu_{obs} = \nu_{rest}(1+z)$: *rest frequency (GHz)*

D_L: *luminosity distance (MPc)*

z: *redshift*

We have calculated $L_{CO(3-2)}$ for our sources using the second formulation.

4.3.2 Molecular gas and dust masses

Measurements of the CO emission originating from high-redshift galaxies play an essential role in determining the size of the underlying molecular gas reservoir. Although this reservoir is composed of gas that is mainly in the form of H_2, the rotational symmetry of

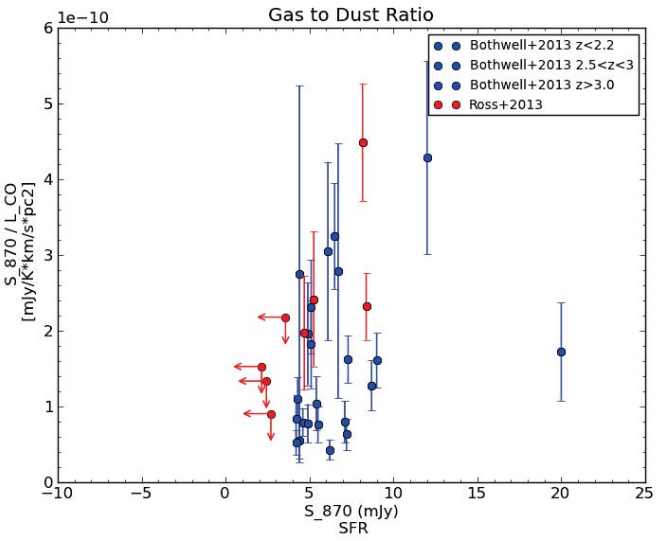

Figure 4.2: Gas-to-dust ratios plotted versus the 870 flux (SF) for our 8 SMA sources (red) and Bothwell sources (blue). Data points with arrows represent a 3-σ upper limit.

this molecule makes it necessary to infer its properties from the more easily detected CO measurement. As a result, it is possible to probe the raw material that acts to fuel future star formation.

To estimate the mass of H_2 in a given system, it is first necessary to reduce the measured luminosities that originate from higher transitions to an equivalent luminosity using a brightness ratio. The brightness ratios used in this study were calculated in the Bothwell et al. 2012 study.

An example of this step and the associated error can be seen below:

$$L_{1-0} = \frac{L_{3-2}}{0.54}\ [Kkms^{-1}pc^2]$$

$$\Delta L_{1-0} = \frac{L_{1-0}}{SNR}\ [Kkms^{-1}pc^2]$$

$$\frac{m_{gas}}{m_{dust}} + \Delta\frac{m_{gas}}{m_{dust}} = \frac{S_{870} + \Delta S_{870}}{L_{1-0} + \Delta L_{1-0}} \tag{4.3}$$

4.3.3 Stacking Analysis

In this section we present the stacking analysis that was performed on the 870μm SMA continuum observations. The use of a stacking routine was necessitated as a result of the intrinsically faint nature of sub-mm selected galaxies at high-z. The methods employed in a stacking routine provide a means to raise the sensitivity of a class of faint sources (i.e. it acts as a sensitivity booster) and have been applied to a variety of studies ranging in wavelength (insert references). It has been only recently that these techniques have been applied to sub-mm observations (e.g. R. Declari et al. 2013).

The routine used in this study follows the same basic principles as outlined in R. Declari et al. and is as follows:

1) Sources were selected based on:

2) The offset of each source with respect to the pointing center of the SMA observations was computed and then used to model the primary beam (PB) correction.

Mathematically this is expressed using the taper correction:

$$= exp(\frac{offset^2}{2\sigma_{PB}^2}) \tag{4.4}$$

where,

$$\sigma_{PB} = \frac{PB}{2\sqrt{2ln2}} \tag{4.5}$$

An equivalent operation to computing the offset and subsequent taper correction as shown above is to produce a gain map. This step was completed by using a gain map in this study.

3) A copy of each source was produced at its astronomic reference position in the SMA map and then each one was translated to an arbitrary center at RA=00:00:00 DEC=00:00:00.

ID	RA	DEC	S870 [mJy]	S450 [mJy]	S24 [mJy]	S3mm [mJy]	SCO [Jy km/s]	z_{CO}	comments
q1549	15:51:52.470	19:11:03.900	6.8	650	20946.4	0.327	0.778	2.847	
MD17	15:51:53.750	19:11:09.970	7.8	440	230.1	0.904	0.528	2.856	
nb63	15:51:53.980	19:10:41.800	2.7	1000	51.3	0.327	0.505	2.841	SCUBA-2 data
Q15nbr	15:51:52.520	19:11:04.000	2.3	270	10.0	0.327	0.229	2.839	
D14	15:51:53.250	19:11:01.010	5.5	460	440.8	0.582	0.325	2.853	
MD12	15:51:51.870	19:10:41.020	2.4303	880	13.7	0.448	0.530	2.847	
M15	15:51:51.260	19:11:05.580	2.142	250	33.3	0.100	0.247	2.853	
NB133	15:51:54.760	19:11:06.300	3.57	290	10.0	0.100	0.215	2.847	

Table 4.1: Properties of the galaxies detected as CO(3-2) emitters

This procedure was carried out by reading the flux values directly from our map.

4) Finally, all of the copies were realigned, scaled according to their taper correction and weight averaged. The weight average can be computed as the squared inverse of the taper correction, or statistically as $\frac{\sum S/N^2}{\sum 1/N^2}$.

4.3.4 CO Detections

The multi-wavelength data, including the PdBI, SCUBA-2 and high-resolution SMA imaging for the 8 CO detections is summarized in Table 1.

Spectral energy distribution (SED) templates derived from [82] were used to fit the sources. The templates remain fixed in z, but extend over a variety of dust temperatures. A root-mean-square (rms) method was used to determine the best fit to observations. The results are presented in Appendix A.

4.4 Discussion and Conclusions

Understanding the history of the universe is a complex problem that relies on our ability to continue pushing the limits of technology to observe greater distances. It is clear that nearby galaxies differ from those at high redshift, meaning they have gone through a period of evolution. A key question that continues to be the subject of many studies is the details concerning galaxy evolution, from the initial quantum sized fluctuations in the CMB to the large-scale structure we see today. One of the most important factors contributing to the evolutionary process is the amount of gas present in the galaxy. Of particular interest is the available supply of atomic hydrogen (H_2) gas, since it is fuels star formation. However, as

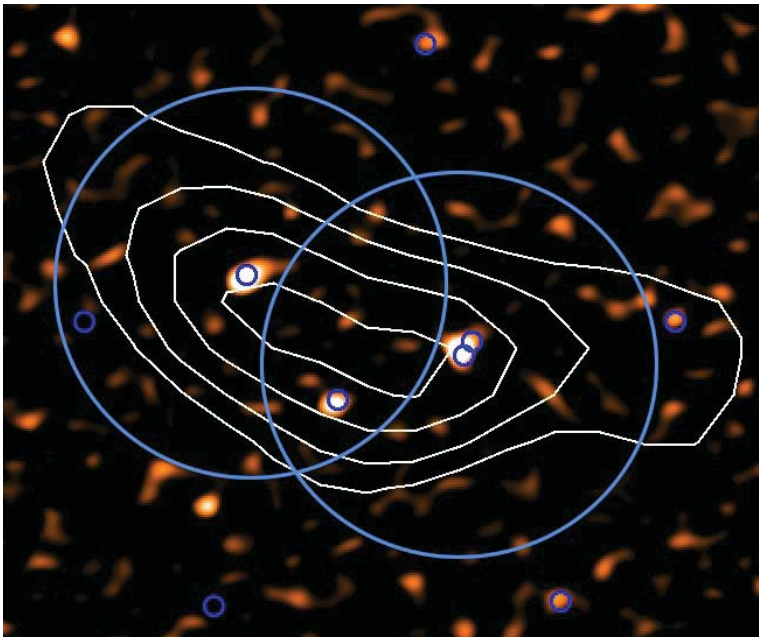

Figure 4.3: SMA 870μm map (40″ by 30″) of the $z\sim$2.84 H1549 protocluster field. CO-emitters from the PdBI map are shown as blue squares, while the SCUBA2 contours are shown overlaid (white). The SMA has effectively detected at least 5 of the CO emitters at 870μm continuum, clearly explaining the unresolved SCUBA-2 emission, and allowing for far-IR SEDs to be fit to individual CO-emitting galaxies, and gas/dust ratios to be estimated precisely. We will constrain their ISM properties and elucidate the effect of the large overdensity on the gas supplies, stellar masses, and star formation modes relative to the field population.

a result of its atomic structure, H_2 cannot be directly observed. Therefore, the molecular gas (usually CO) content is measured and then converted to an H_2 equivalent.

Studies of nearby galaxies show there exists a relationship between their properties and environment. In general, galaxies with enhanced star formation rates are found to reside in low-density regions. Observations also indicate that all of the gas supplies in the core regions of the larger galaxy clusters have been used up and star formation is no longer occurring.

The H1549 field has proven to be an interesting region to study for two main reasons. First, it represents one of the highest density clusters (i.e. a region with many galaxies concentrated into a small volume) that have been studied to date. The significance of this lies in our ability to study the effect of such a large overdesnity on the evolution of galaxies in this type of environment and how they compare to the field (i.e. how they differ from similar galaxies in less dense regions that are more representative of the average population). An overdensity of this size would have originated in one of the highest overdensities in the CMB, thus H1549 represents a region where accelerated galaxy evolution is occurring.

Secondly, the higher than average density of galaxies facilitated a single frequency setting of the Plateau de Bure interferometer (PdBI) of 4 GHz bandwidth, tuned to a 345 GHz line (i.e. CO(3-2)) at z=2.85. Therefore, studying this field did not require time intensive observations, making for an efficient data collection process.

Blind surveys of the H1549 field performed with PdBI revealed a population of at least seven galaxies with statistically significant CO(3-2) line emission, namely, q1549, D14, MD17, nb63, MD12, M15 and NB133. There remains some uncertainty over a possible eighth source, since the proximity of this potential galaxy to the luminous quasar did not allow for a clear detection.

A 40 arcsecond by 30 arcsecond map of the 870 μm SMA data is shown in Figure 4.3 with the 850 μm continuum emission from SCUBA-2 contoured and the individual CO sources labeled. This figure clearly illustrates the need for follow-up studies with the higher resolution SMA. Initial SCUBA-2 maps revealed an extended region of emission focused in the centre of the image, while the SMA data enabled for a clear detection (i.e. greater than 4-σ) of at least three sources, each with an associated CO counterpart (i.e. q1549, D14 and MD17). These three sources represent a population of highly dust-obscured star forming galaxies with large molecular gas masses.

The 870 μm SMA map also reveals many fainter galaxies that were not able to be detected with a high enough signal-to-noise ratio to be considered significant. For this reason, a stacking procedure was used on the SMA data to enable a detection of an average of a fainter galaxy in the field. The process works by reducing the effective noise in the H1549 field by combining the weaker signal of all the fainter galaxies into one stronger signal. This average signal can then be detected above the background noise.

Combining the CO line luminosities and 850 μm continuum measurements for the 3 sources that were detected in both, allowed us to derive the gas-to-dust ratio for each galaxy and use it as an astrophysical diagnostic. These values were then compared to a catalogue of sources from Bothwell et al., which are more representative of the field population.

The result of this comparison is shown in figure 4.2, which plots the gas-to-dust ratios for the H1549 sources along with the Bothwell et al. sources. The SMGs from the H1549 field appear to have comparable gas-to-dust ratios to the upper 50% of the *Bothwell et al. 2013* SMGs. This suggests that the ISM conditions may be biased in the protocluster SMGs, with either higher 850 μ m fluxes per unit L_{CO} or lower L_{CO} per 850 μ m flux. The first indicates that either more of the dust in the SMGs is illuminated or the presence of colder dust temperatures, while the second is a potential result of several factors. These are a lower excitation of the CO(3-2), a lower conversion of CO to H_2, or more efficient star formation.

Comparing the properties of these gas-rich (CO detected), 850 μm bright (dusty) star forming galaxies with the average properties of the field, derived from the stacking routine, reveals that there is a large enhancement in the star formation occurring in the core of these galaxies (at least as large as 13x overdensity of typical galaxies found in the region). Given that typical gas-to-dust ratios are found, it suggests that the core of the cluster is in the process of forming.

Acknowledgements

The SMA is a joint project between the Smithsonian Astrophysical Observatory and the Academia Sinica Institute of Astronomy and Astrophysics and is funded by the Smithsonian Institution and the Academia Sinica. This work is based in on observations made with the *Spitzer Space Telescope*, which is operated by the Jet Propulsion Laboratory, California Institute of Technology, under contract 1407, and data collected at Subaru Telescope,

which is operated by the National Astronomical Observatory of Japan. The James Clerk Maxwell Telescope is operated by The Joint Astronomy Centre on behalf of the Science and Technology Facilities Council of the United Kingdom, the Netherlands Organisation for Scientific Research, and the National Research Council of Canada. IS acknowledges support from the Royal Society.

Chapter 5

Conclusions

In summary, I was able to successfully develop a cryostat to facilitate the increasing need for detector testing with the expansion of the POLARBEAR experiment. My role in the overall POLARBEAR collaboration has been to provide field support for both the commissioning of the telescope and regular observations. Along with the efforts of others, this has helped enable Polarbear to provide the first independent measurement of the B-mode signal from gravitational lensing.

Since my work with the POLARBEAR collaboration did not include any data analysis, I joined a project led by my supervisor, Dr. Scott Chapman, and his colleagues to gain experience working with submm wavelengths data. My work included analyzing high-resolution data from the SMA, showing that overdense galaxy regions tentatively distinguish themselves from the field population.

Appendix A

Spectral Energy Distributions

More detailed work on multi-wavelength follow-up is warranted in these H1549 SMGs to better understand any biases of the population in the protocluster relative to the field population.

While the photometric data is fairly sparse at present, fits of template SMGs with different dust temperatures are shown here as a guide to how the data is beginning to constrain the properties of these SMGs. Within the limited data, it is possible to conclude that the H1549 SMGs are fairly typical of the SMG population. However, obtaining additional data points over the peak of the dust grey-body (modified black body for the emissivity of the dust) will allow more detailed comparisons and fits to be made.

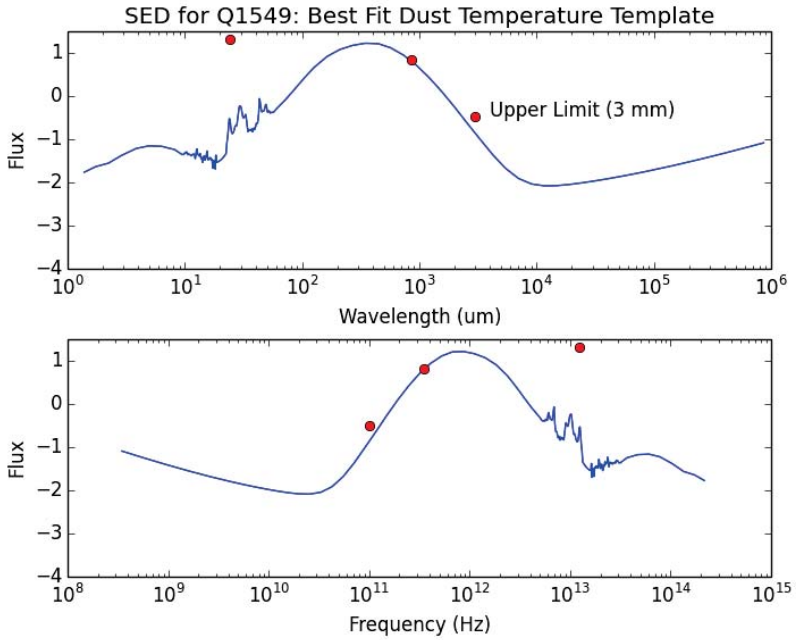

Figure A.1: Q1549: Spectral energy distribution with best fit dust temperature shown.

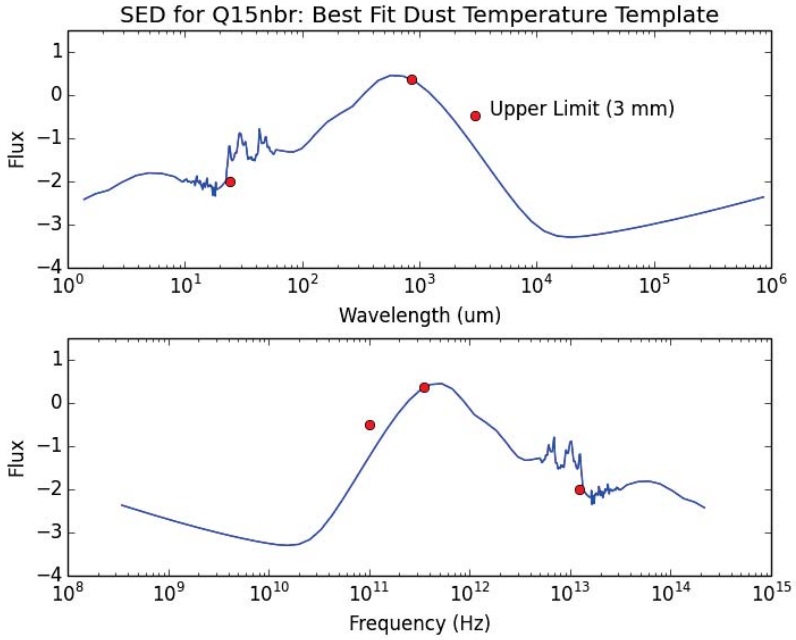

Figure A.2: Q15nbr: Spectral energy distribution with best fit dust temperature shown.

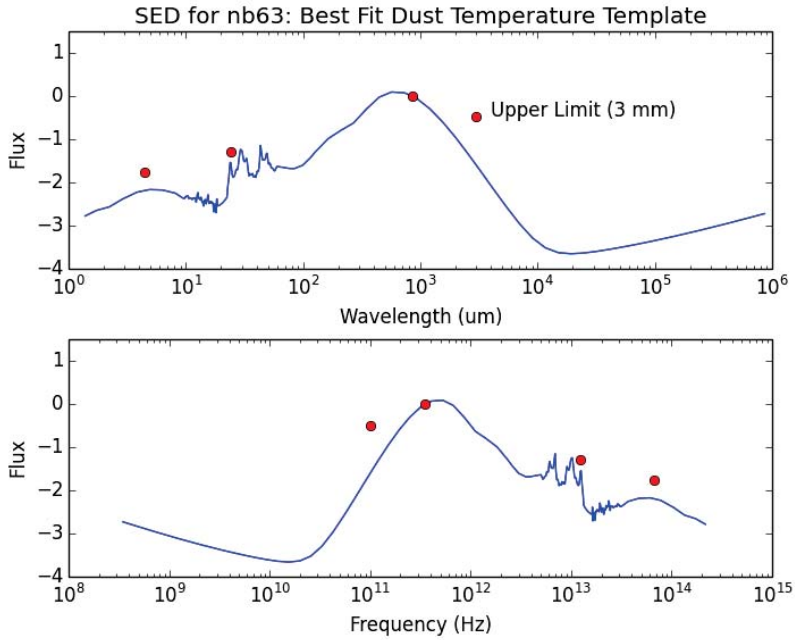

Figure A.3: nb63: Spectral energy distribution with best fit dust temperature shown.

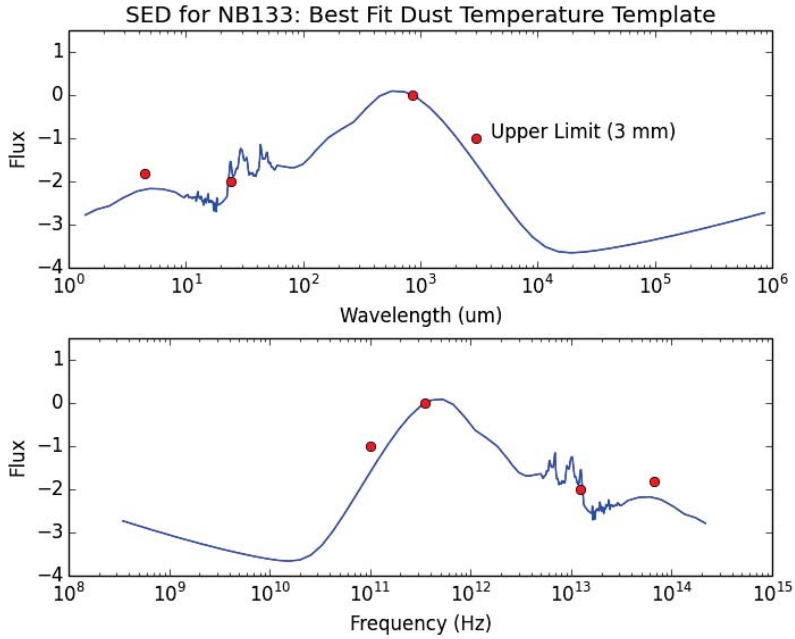

Figure A.4: NB133: Spectral energy distribution with best fit dust temperature shown.

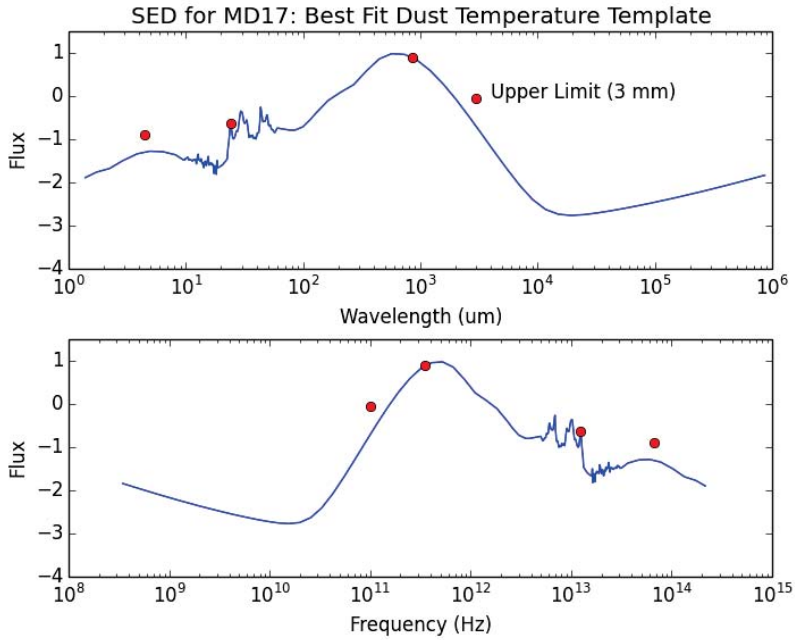

Figure A.5: MD17: Spectral energy distribution with best fit dust temperature shown.

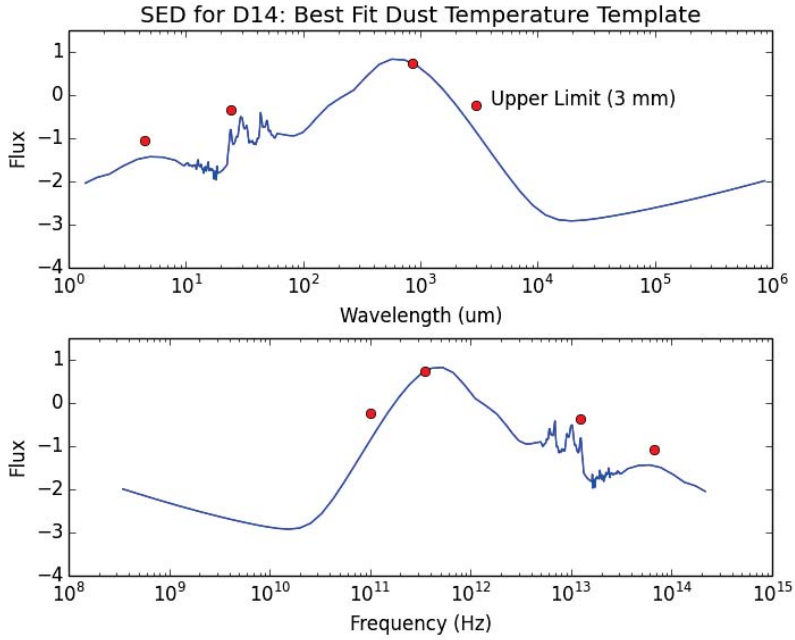

Figure A.6: D14: Spectral energy distribution with best fit dust temperature shown.

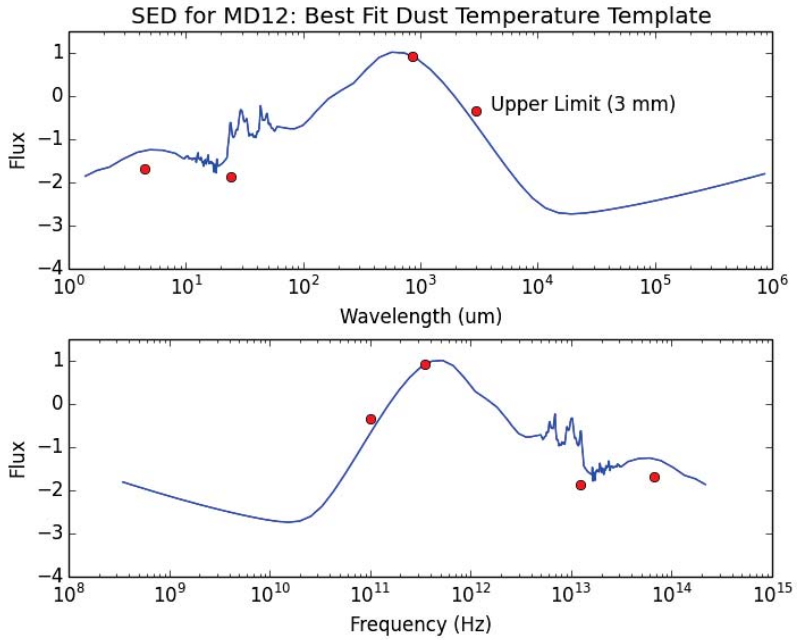

Figure A.7: MD12: Spectral energy distribution with best fit dust temperature shown.

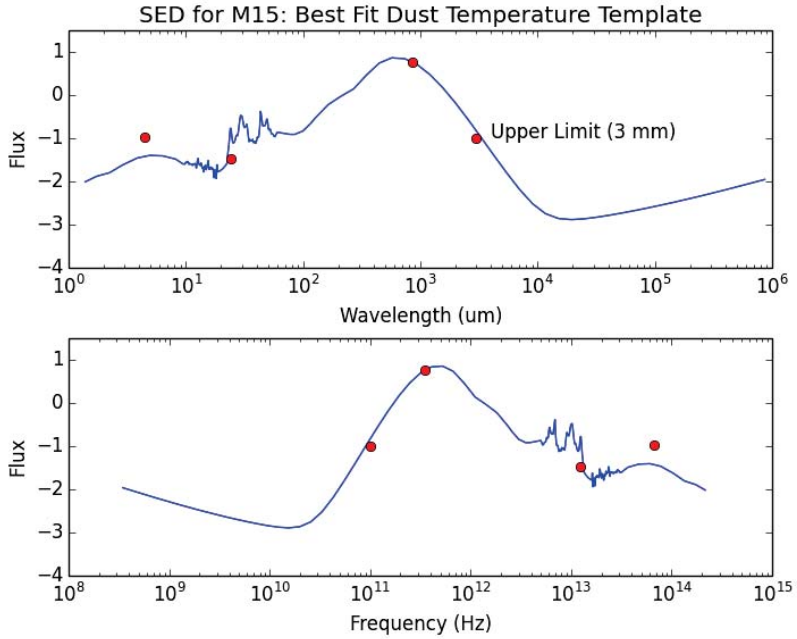

Figure A.8: M15: Spectral energy distribution with best fit dust temperature shown.

Bibliography

[1] PAR Ade, Y Akiba, AE Anthony, K Arnold, M Atlas, D Barron, D Boettger, J Borrill, C Borys, S Chapman, et al. Evidence for gravitational lensing of the cosmic microwave background polarization from cross-correlation with the cosmic infrared background. *Physical review letters*, 112(13):131302, 2014.

[2] PAR Ade, Y Akiba, AE Anthony, K Arnold, M Atlas, D Barron, D Boettger, J Borrill, S Chapman, Y Chinone, et al. Measurement of the cosmic microwave background polarization lensing power spectrum with the polarbear experiment. *Physical review letters*, 113(2):021301, 2014.

[3] Peter AR Ade, Giampaolo Pisano, Carole Tucker, and Samuel Weaver. A review of metal mesh filters. In *Astronomical Telescopes and Instrumentation*, pages 62750U–62750U. International Society for Optics and Photonics, 2006.

[4] Manuel Aravena, Jeff Wagg, PP Papadopoulos, and IJ Feain. Unveiling the mask on the ulirg-to-qso transition object [h89] 1821+ 643 at z= 0.3: A gas-poor/gas-rich galaxy merger and the implications for co-based dynamical mass estimates. *The Astrophysical Journal*, 737(2):64, 2011.

[5] Kam Stahly Arnold. *Design and deployment of the POLARBEAR cosmic microwave background polarization experiment*. 2010.

[6] Jason E Austermann, KA Aird, JA Beall, Dan Becker, Amy Bender, BA Benson, LE Bleem, Joe Britton, JE Carlstrom, CL Chang, et al. Sptpol: an instrument for cmb polarization measurements with the south pole telescope. In *SPIE Astronomical Telescopes+ Instrumentation*, pages 84521E–84521E. International Society for Optics and Photonics, 2012.

[7] AJ Barger, LL Cowie, DB Sanders, E Fulton, Y Taniguchi, Y Sato, K Kawara, and H Okuda. Submillimetre-wavelength detection of dusty star-forming galaxies at high redshift. *Nature*, 394(6690):248–251, 1998.

[8] Darcy Barron, Matt Atlas, Brian Keating, Ron Quillin, Nathan Stebor, and Brandon Wilson. Performance of a 4 kelvin pulse-tube cooled cryostat with dc squid amplifiers for bolometric detector testing. *arXiv preprint arXiv:1301.0860*, 2013.

[9] CM Baugh, CG Lacey, CS Frenk, GL Granato, L Silva, A Bressan, AJ Benson, and S Cole. Can the faint submillimetre galaxies be explained in the λ cold dark matter model? *Monthly Notices of the Royal Astronomical Society*, 356(3):1191–1200, 2005.

[10] Dominic J Benford, Min S Yun, Todd R Hunter, Peter M Bryant, and Thomas G Phillips. Multitransition submillimeter co observations of ultraluminous iras galaxies. In *CO: Twenty-Five Years of Millimeter-Wave Spectroscopy*, volume 170, page 8P, 1996.

[11] CL Bennett, AJ Banday, KM Gorski, G Hinshaw, P Jackson, P Keegstra, A Kogut, GF Smoot, DT Wilkinson, and EL Wright. Four-year cobe dmr cosmic microwave background observations: maps and basic results. *The Astrophysical Journal Letters*, 464(1):L1, 1996.

[12] A Benoit and S Pujol. Dilution refrigerator for space applications with a cryocooler. *Cryogenics*, 34(5):421–423, 1994.

[13] RS Bhatia, ST Chase, SF Edgington, J Glenn, WC Jones, AE Lange, B Maffei, AK Mainzer, PD Mauskopf, BJ Philhour, et al. A three-stage helium sorption refrigerator for cooling of infrared detectors to 280 mk. *Cryogenics*, 40(11):685–691, 2000.

[14] Frank Bigiel, Adam Leroy, Fabian Walter, Elias Brinks, WJG De Blok, Barry Madore, and Michele D Thornley. The star formation law in nearby galaxies on sub-kpc scales. *The Astronomical Journal*, 136(6):2846, 2008.

[15] Andrew W Blain, SC Chapman, Ian Smail, and Rob Ivison. Clustering of submillimeter-selected galaxies. *The Astrophysical Journal*, 611(2):725, 2004.

[16] Andrew W Blain, Ian Smail, RJ Ivison, J-P Kneib, and David T Frayer. Submillimeter galaxies. *Physics Reports*, 369(2):111–176, 2002.

[17] AW Blain and MS Longair. Submillimetre cosmology. *Monthly Notices of the Royal Astronomical Society*, 264(2):509–521, 1993.

[18] MS Bothwell, Ian Smail, SC Chapman, R Genzel, RJ Ivison, LJ Tacconi, S Alaghband-Zadeh, F Bertoldi, AW Blain, CM Casey, et al. A survey of molecular gas in luminous sub-millimetre galaxies. *Monthly Notices of the Royal Astronomical Society*, 429(4):3047–3067, 2013.

[19] JA Brevik, RW Aikin, M Amiri, SJ Benton, JJ Bock, JA Bonetti, B Burger, CD Dowell, L Duband, JP Filippini, et al. Initial performance of the bicep2 antenna-coupled superconducting bolometers at the south pole. In *SPIE Astronomical Telescopes+ Instrumentation*, pages 77411H–77411H. International Society for Optics and Photonics, 2010.

[20] Caitlin M Casey, Desika Narayanan, and Asantha Cooray. Dusty star-forming galaxies at high redshift. *Physics Reports*, 2014.

[21] Edward L Chapin, David S Berry, Andrew G Gibb, Tim Jenness, Douglas Scott, Remo PJ Tilanus, Frossie Economou, and Wayne S Holland. Scuba-2: iterative map-making with the sub-millimetre user reduction facility. *Monthly Notices of the Royal Astronomical Society*, 430(4):2545–2573, 2013.

[22] SC Chapman, AW Blain, RJ Ivison, and Ian R Smail. A median redshift of 2.4 for galaxies bright at submillimetre wavelengths. *Nature*, 422(6933):695–698, 2003.

[23] SC Chapman, AW Blain, Ian Smail, and RJ Ivison. A redshift survey of the submillimeter galaxy population. *The Astrophysical Journal*, 622(2):772, 2005.

[24] SC Chapman, RJ Ivison, IG Roseboom, R Auld, J Bock, D Brisbin, D Burgarella, P Chanial, DL Clements, A Cooray, et al. Herschel-spire, far-infrared properties of millimetre-bright and-faint radio galaxies. *Monthly Notices of the Royal Astronomical Society: Letters*, 409(1):L13–L18, 2010.

[25] Goutam Chattopadhyay and Jonas Zmuidzinas. A dual-polarized slot antenna for millimeter waves. *IEEE Transactions on Antennas and Propagation*, 46(5):736–737, 1998.

[26] DL Clements, E Rigby, S Maddox, L Dunne, A Mortier, C Pearson, A Amblard, R Auld, Maarten Baes, D Bonfield, et al. The herschel-atlas: Extragalactic number counts from 250 to 500 microns. *arXiv preprint arXiv:1005.2409*, 2010.

[27] NG Czakon, A Vayonakis, J Schlaerth, MI Hollister, S Golwala, PK Day, J-S Gao, J Glenn, H LeDuc, PR Maloney, et al. Microwave kinetic inductance detector (mkid) camera testing for submillimeter astronomy. In *AIP Conference Proceedings*, number 1185, pages 172–175. American Institute of Physics, 2009.

[28] E Daddi, F Bournaud, F Walter, H Dannerbauer, CL Carilli, M Dickinson, D Elbaz, GE Morrison, D Riechers, M Onodera, et al. Very high gas fractions and extended gas reservoirs in z= 1.5 disk galaxies. *The Astrophysical Journal*, 713(1):686, 2010.

[29] MA Dobbs, M Lueker, KA Aird, AN Bender, BA Benson, LE Bleem, JE Carlstrom, CL Chang, H-M Cho, J Clarke, et al. Frequency multiplexed superconducting quantum interference device readout of large bolometer arrays for cosmic microwave background measurements. *Review of Scientific Instruments*, 83(7):073113, 2012.

[30] Matt Dobbs, Eric Bissonnette, and Helmuth Spieler. Digital frequency domain multiplexer for millimeter-wavelength telescopes. *Nuclear Science, IEEE Transactions on*, 55(1):21–26, 2008.

[31] Matt Dobbs, Mark Halpern, Kent D Irwin, Adrian T Lee, JAB Mates, and Benjamin A Mazin. Multiplexed readout of cmb polarimeters. In *Journal of Physics: Conference Series*, volume 155, page 012004. IOP Publishing, 2009.

[32] Robert Dumoulin. First results from the quiet telescope. In *Bulletin of the American Astronomical Society*, volume 43, page 43213, 2011.

[33] Jack Ekin. *Experimental Techniques for Low-Temperature Measurements: Cryostat Design, Material Properties and Superconductor Critical-Current Testing: Cryostat Design, Material Properties and Superconductor Critical-Current Testing*. Oxford University Press, 2006.

[34] D Elbaz, E Daddi, D Le Borgne, M Dickinson, DM Alexander, RR Chary, JL Starck, WN Brandt, M Kitzbichler, E MacDonald, et al. The reversal of the star formation-density relation in the distant universe. *arXiv preprint astro-ph/0703653*, 2007.

[35] D Elbaz, M Dickinson, HS Hwang, T Díaz-Santos, G Magdis, B Magnelli, D Le Borgne, F Galliano, M Pannella, P Chanial, et al. Goods-herschel: an infrared main sequence for star-forming galaxies. *arXiv preprint arXiv:1105.2537*, 2011.

[36] C. Enss and S. Hunklinger. *Low-Temperature Physics*. SpringerLink: Springer e-Books. Springer, 2005.

[37] GG Fazio, JL Hora, LE Allen, MLN Ashby, P Barmby, LK Deutsch, J-S Huang, S Kleiner, M Marengo, ST Megeath, et al. The infrared array camera (irac) for the spitzer space telescope. *The Astrophysical Journal Supplement Series*, 154(1):10, 2004.

[38] Daniel F Filipovic, Steven S Gearhart, and Gabriel M Rebeiz. Double-slot antennas on extended hemispherical and elliptical silicon dielectric lenses. *Microwave Theory and Techniques, IEEE Transactions on*, 41(10):1738–1749, 1993.

[39] DJ Fixsen, ES Cheng, JM Gales, John C Mather, RA Shafer, and EL Wright. The cosmic microwave background spectrum from the full cobe firas data set. *The Astrophysical Journal*, 473(2):576, 1996.

[40] James E Geach and Padelis P Papadopoulos. Molecular and atomic line surveys of galaxies. i. the dense, star-forming gas phase as a beacon. *The Astrophysical Journal*, 757(2):156, 2012.

[41] James E Geach, Ian Smail, Sean M Moran, Tommaso Treu, and Richard S Ellis. The nature of dusty starburst galaxies in a rich cluster at z= 0.4: the progenitors of lenticulars? *The Astrophysical Journal*, 691(1):783, 2009.

[42] Gaël Godi, Ronan Sauleau, and Daniel Thouroude. Performance of reduced size substrate lens antennas for millimeter-wave communications. *Antennas and Propagation, IEEE Transactions on*, 53(4):1278–1286, 2005.

[43] TR Greve, F Bertoldi, Ian Smail, R Neri, SC Chapman, AW Blain, RJ Ivison, R Genzel, A Omont, P Cox, et al. An interferometric co survey of luminous submillimetre galaxies. *Monthly Notices of the Royal Astronomical Society*, 359(3):1165–1183, 2005.

[44] S Guilloteau and R Lucas. Imaging at the iram plateau de bure interferometer. In *Imaging at Radio through Submillimeter Wavelengths*, volume 217, page 299, 2000.

[45] Kevin N Hainline, Alice E Shapley, Jenny E Greene, and Charles C Steidel. The rest-frame ultraviolet spectra of uv-selected active galactic nuclei at z˜ 2-3. *The Astrophysical Journal*, 733(1):31, 2011.

[46] D Hanson, S Hoover, A Crites, PAR Ade, KA Aird, JE Austermann, JA Beall, AN Bender, BA Benson, LE Bleem, et al. Detection of b-mode polarization in the cosmic microwave background with data from the south pole telescope. *Physical review letters*, 111(14):141301, 2013.

[47] Ryan C Hickox, JL Wardlow, Ian Smail, AD Myers, DM Alexander, AM Swinbank, ALR Danielson, JP Stott, SC Chapman, KEK Coppin, et al. The laboca survey of the extended chandra deep field-south: clustering of submillimetre galaxies. *Monthly Notices of the Royal Astronomical Society*, 421(1):284–295, 2012.

[48] Paul TP Ho, James M Moran, and Kwok Yung Lo. The submillimeter array. *The Astrophysical Journal Letters*, 616(1):L1, 2004.

[49] Wayne S Holland, EI Robson, Walter K Gear, Colin R Cunningham, John F Lightfoot, Tim Jenness, Rob J Ivison, Jason A Stevens, Peter AR Ade, MJ Griffin, et al. Scuba: a common-user submillimetre camera operating on the james clerk maxwell telescope. *Monthly Notices of the Royal Astronomical Society*, 303(4):659–672, 1999.

[50] WS Holland, D Bintley, EL Chapin, Antonio Chrysostomou, GR Davis, JT Dempsey, WD Duncan, M Fich, P Friberg, M Halpern, et al. Scuba-2: the 10 000 pixel bolometer camera on the james clerk maxwell telescope. *Monthly Notices of the Royal Astronomical Society*, 430(4):2513–2533, 2013.

[51] David H Hughes, Stephen Serjeant, James Dunlop, Michael Rowan-Robinson, Andrew Blain, Robert G Mann, Rob Ivison, John Peacock, Andreas Efstathiou, Walter Gear, et al. High-redshift star formation in the hubble deep field revealed by a submillimetre-wavelength survey. *nature*, 394(6690):241–247, 1998.

[52] RJ Ivison, TR Greve, JS Dunlop, JA Peacock, E Egami, Ian Smail, E Ibar, E Van Kampen, I Aretxaga, T Babbedge, et al. The scuba half degree extragalactic survey–iii. identification of radio and mid-infrared counterparts to submillimetre galaxies. *Monthly Notices of the Royal Astronomical Society*, 380(1):199–228, 2007.

[53] Rob J Ivison, Thomas R Greve, Ian Smail, James S Dunlop, Nathan D Roche, Susie E Scott, Mat J Page, Jason A Stevens, Omar Almaini, Andrew W Blain, et al. Deep radio imaging of the scuba 8-mjy survey fields: submillimetre source identifications and redshift distribution. *Monthly Notices of the Royal Astronomical Society*, 337(1):1–25, 2002.

[54] William S Janna. *Engineering heat transfer*. CRC Press, 1999.

[55] Tim Jenness, David Berry, Ed Chapin, Frossie Economou, Andy Gibb, and Douglas Scott. Scuba-2 data processing. *arXiv preprint arXiv:1011.5876*, 2010.

[56] BR Johnson, J Collins, ME Abroe, PAR Ade, J Bock, J Borrill, A Boscaleri, P De Bernardis, S Hanany, AH Jaffe, et al. Maxipol: cosmic microwave background

polarimetry using a rotating half-wave plate. *The Astrophysical Journal*, 665(1):42, 2007.

[57] Wesley Johnson. Thermal analysis of low layer density multilayer insulation test results. In *ADVANCES IN CRYOGENIC ENGINEERING: Transactions of the Cryogenic Engineering Conference-CEC, Volume 57*, volume 1434, pages 1519–1526. AIP Publishing, 2012.

[58] Kenichi Karatsu, Masato Naruse, Tom Nitta, Masakazu Sekine, Yutaro Sekimoto, Takashi Noguchi, Yoshinori Uzawa, Hiroshi Matsuo, and Hitoshi Kiuchi. Development of 1000 arrays mkid camera for the cmb observation. In *SPIE Astronomical Telescopes+ Instrumentation*, pages 84520Q–84520Q. International Society for Optics and Photonics, 2012.

[59] Brian G Keating, Peter AR Ade, James J Bock, Eric Hivon, William L Holzapfel, Andrew E Lange, Hien Nguyen, and Ki Won Yoon. Bicep: a large angular scale cmb polarimeter. In *Astronomical Telescopes and Instrumentation*, pages 284–295. International Society for Optics and Photonics, 2003.

[60] Dusan Keres, Min S Yun, and JS Young. Co luminosity functions for far-infrared- and b-band-selected galaxies and the first estimate for ωhi+ h2. *The Astrophysical Journal*, 582(2):659, 2003.

[61] Zigmund D Kermish, Peter Ade, Aubra Anthony, Kam Arnold, Darcy Barron, David Boettger, Julian Borrill, Scott Chapman, Yuji Chinone, Matt A Dobbs, et al. The polarbear experiment. In *SPIE Astronomical Telescopes+ Instrumentation*, pages 84521C–84521C. International Society for Optics and Photonics, 2012.

[62] Arthur Kosowsky. The atacama cosmology telescope. *New Astronomy Reviews*, 47(11):939–943, 2003.

[63] Mark R Krumholz, Christopher F McKee, and Jason Tumlinson. The star formation law in atomic and molecular gas. *The Astrophysical Journal*, 699(1):850, 2009.

[64] Guilaine Lagache, Jean-Loup Puget, and Hervé Dole. Dusty infrared galaxies: sources of the cosmic infrared background. *arXiv preprint astro-ph/0507298*, 2005.

[65] Claudia del P Lagos, Carlton M Baugh, Cedric G Lacey, Andrew J Benson, Han-Seek Kim, and Chris Power. Cosmic evolution of the atomic and molecular gas contents of galaxies. *Monthly Notices of the Royal Astronomical Society*, 418(3):1649–1667, 2011.

[66] TM Lanting, Hsiao-Mei Cho, John Clarke, Matt Dobbs, Adrian T Lee, M Lueker, PL Richards, AD Smith, and HG Spieler. Frequency domain multiplexing for bolometer arrays. *Nuclear Instruments and Methods in Physics Research Section A: Accelerators, Spectrometers, Detectors and Associated Equipment*, 520(1):548–550, 2004.

[67] Trevor Michael Lanting. Multiplexed readout of superconducting bolometers for cosmological observations. 2006.

[68] Shih-Fu Lee, Jan M Gildemeister, Warren Holmes, Adrian T Lee, and Paul L Richards. Voltage-biased superconducting transition-edge bolometer with strong electrothermal feedback operated at 370 mk. *Applied Optics*, 37(16):3391–3397, 1998.

[69] Antony Lewis and Anthony Challinor. Camb: Code for anisotropies in the microwave background. *Astrophysics Source Code Library*, 1:02026, 2011.

[70] Malcolm S Longair. *Theoretical concepts in physics: an alternative view of theoretical reasoning in physics*. Cambridge University Press, 2003.

[71] Martin Lueker, CL Reichardt, KK Schaffer, O Zahn, PAR Ade, KA Aird, BA Benson, LE Bleem, JE Carlstrom, CL Chang, et al. Measurements of secondary cosmic microwave background anisotropies with the south pole telescope. *The Astrophysical Journal*, 719(2):1045, 2010.

[72] B Magnelli, D Lutz, P Santini, A Saintonge, S Berta, M Albrecht, B Altieri, P Andreani, H Aussel, F Bertoldi, et al. A herschel view of the far-infrared properties of submillimetre galaxies. *Astronomy & Astrophysics/Astronomie et Astrophysique*, 539, 2012.

[73] Michael J Mortonson and Uroš Seljak. A joint analysis of planck and bicep2 b modes including dust polarization uncertainty. *arXiv preprint arXiv:1405.5857*, 2014.

[74] Michael J Myers, William Holzapfel, Adrian T Lee, Roger OBrient, PL Richards, Huan T Tran, Peter Ade, Greg Engargiola, Andy Smith, and Helmuth Spieler. An antenna-coupled bolometer with an integrated microstrip bandpass filter. *Applied Physics Letters*, 86(11):114103, 2005.

[75] Desika Narayanan, Christopher C Hayward, Thomas J Cox, Lars Hernquist, Patrik Jonsson, Joshua D Younger, and Brent Groves. The formation of high-redshift submillimetre galaxies. *Monthly Notices of the Royal Astronomical Society*, 401(3):1613–1619, 2010.

[76] D Obreschkow, D Croton, G De Lucia, S Khochfar, and S Rawlings. Simulation of the cosmic evolution of atomic and molecular hydrogen in galaxies. *The Astrophysical Journal*, 698(2):1467, 2009.

[77] D Obreschkow and S Rawlings. H2/hi ratio in galaxies (obreschkow+. *VizieR Online Data Catalog*, 739:41857, 2009.

[78] JB Oke, JG Cohen, M Carr, J Cromer, A Dingizian, FH Harris, S Labrecque, R Lucinio, W Schaal, H Epps, et al. The keck low-resolution imaging spectrometer. *Publications of the Astronomical Society of the Pacific*, pages 375–385, 1995.

[79] A Orlando, RW Aikin, M Amiri, JJ Bock, JA Bonetti, JA Brevik, B Burger, G Chattopadthyay, PK Day, JP Filippini, et al. Antenna-coupled tes bolometer arrays for bicep2/keck and spider. *arXiv preprint arXiv:1009.3685*, 2010.

[80] Paul Oxley, Peter A Ade, C Baccigalupi, Hsiao-Mei Cho, Mark J Devlin, Shaul Hanany, BR Johnson, T Jones, Adrian T Lee, T Matsumura, et al. The ebex experiment. In *Optical Science and Technology, the SPIE 49th Annual Meeting*, pages 320–331. International Society for Optics and Photonics, 2004.

[81] Frank Pobell. *Matter and methods at low temperatures*, volume 2. Springer, 1996.

[82] Alexandra Pope, Douglas Scott, Mark Dickinson, Ranga-Ram Chary, Glenn Morrison, Colin Borys, Anna Sajina, David M Alexander, Emanuele Daddi, David Frayer, et al. The hubble deep field-north scuba super-map–iv. characterizing submillimetre galaxies using deep spitzer imaging. *Monthly Notices of the Royal Astronomical Society*, 370(3):1185–1207, 2006.

[83] Dominik A Riechers, CM Bradford, DL Clements, CD Dowell, I Pérez-Fournon, RJ Ivison, C Bridge, A Conley, Hai Fu, JD Vieira, et al. A dust-obscured massive maximum-starburst galaxy at a redshift of 6.34. *Nature*, 496(7445):329–333, 2013.

[84] GH Rieke, ET Young, CW Engelbracht, DM Kelly, FJ Low, EE Haller, JW Beeman, KD Gordon, JA Stansberry, KA Misselt, et al. The multiband imaging photometer for spitzer (mips). *The Astrophysical Journal Supplement Series*, 154(1):25, 2004.

[85] Gwen C Rudie, Charles C Steidel, Ryan F Trainor, Olivera Rakic, Milan Bogosavljević, Max Pettini, Naveen Reddy, Alice E Shapley, Dawn K Erb, and David R Law. The gaseous environment of high-z galaxies: Precision measurements of neutral hydrogen in the circumgalactic medium of z˜ 2-3 galaxies in the keck baryonic structure survey. *The Astrophysical Journal*, 750(1):67, 2012.

[86] John Ruhl, Peter AR Ade, John E Carlstrom, Hsiao-Mei Cho, Thomas Crawford, Matt Dobbs, Chris H Greer, William L Holzapfel, Trevor M Lanting, Adrian T Lee, et al. The south pole telescope. In *Astronomical Telescopes and Instrumentation*, pages 11–29. International Society for Optics and Photonics, 2004.

[87] MC Runyan, PAR Ade, M Amiri, S Benton, R Bihary, JJ Bock, JR Bond, JA Bonetti, SA Bryan, HC Chiang, et al. Design and performance of the spider instrument. In *SPIE Astronomical Telescopes+ Instrumentation*, pages 77411O–77411O. International Society for Optics and Photonics, 2010.

[88] David B Rutledge and Michael S Muha. Imaging antenna arrays. *Antennas and Propagation, IEEE Transactions on*, 30(4):535–540, 1982.

[89] John Ruze. Antenna tolerance theory–a review. In *IEEE Proceedings*, volume 54, pages 633–642, 1966.

[90] Barbara Sue Ryden. *Introduction to cosmology*, volume 523. Addison-Wesley Reading, 2003.

[91] David B Sanders, S-COSMOS Collaboration, et al. Properties of luminous infrared galaxies in the spitzer-cosmos survey. In *Bulletin of the American Astronomical Society*, volume 39, page 152, 2007.

[92] Robert J Sault, Peter J Teuben, and Mel CH Wright. A retrospective view of miriad. In *Astronomical Data Analysis Software and Systems IV*, volume 77, page 433, 1995.

[93] NZ Scoville, JE Carlstrom, CJ Chandler, JA Phillips, SL Scott, RPJ Tilanus, and Z Wang. The relational database and calibration software for the caltech millimeter array. *Publications of the Astronomical Society of the Pacific*, pages 1482–1494, 1993.

[94] AT Serlemitsos, M SanSebastian, and E Kunes. Design of a spaceworthy adiabatic demagnetization refrigerator. *Cryogenics*, 32(2):117–121, 1992.

[95] Ian Smail, RJ Ivison, and AW Blain. A deep submillimeter survey of lensing clusters: A new window on galaxy formation and evolution. *The Astrophysical Journal Letters*, 490(1):L5, 1997.

[96] Vernesa Smolčić, Manuel Aravena, Felipe Navarrete, Eva Schinnerer, Dominik A Riechers, Frank Bertoldi, Chiara Feruglio, Alexis Finoguenov, Mara Salvato, Mark Sargent, et al. Millimeter imaging of submillimeter galaxies in the cosmos field: redshift distribution. *Astronomy & Astrophysics/Astronomie et Astrophysique*, 548, 2012.

[97] PM Solomon, D Downes, and SJE Radford. Warm molecular gas in the primeval galaxy iras 10214+ 4724. *The Astrophysical Journal*, 398:L29–L32, 1992.

[98] David N Spergel, Licia Verde, Hiranya V Peiris, E Komatsu, MR Nolta, CL Bennett, M Halpern, G Hinshaw, N Jarosik, A Kogut, et al. First-year wilkinson microwave anisotropy probe (wmap) observations: determination of cosmological parameters. *The Astrophysical Journal Supplement Series*, 148(1):175, 2003.

[99] Charles Steidel. Illuminating the hi structure of a proto-cluster region at z= 2.84. In *HST Proposal*, volume 1, page 11638, 2008.

[100] Charles C Steidel, Kurt L Adelberger, Alice E Shapley, Dawn K Erb, Naveen A Reddy, and Max Pettini. Spectroscopic identification of a protocluster at z= 2.300: environmental dependence of galaxy properties at high redshift. *The Astrophysical Journal*, 626(1):44, 2005.

[101] Charles C Steidel, Kurt L Adelberger, Alice E Shapley, Max Pettini, Mark Dickinson, and Mauro Giavalisco. Lyα imaging of a proto-cluster region at z= 3.09. *The Astrophysical Journal*, 532(1):170, 2000.

[102] LJ Tacconi, R Genzel, R Neri, P Cox, MC Cooper, K Shapiro, A Bolatto, N Bouché, F Bournaud, A Burkert, et al. High molecular gas fractions in normal massive star-forming galaxies in the young universe. *Nature*, 463(7282):781–784, 2010.

[103] LJ Tacconi, R Genzel, I Smail, R Neri, SC Chapman, RJ Ivison, A Blain, P Cox, A Omont, F Bertoldi, et al. Submillimeter galaxies at z˜ 2: evidence for major mergers and constraints on lifetimes, imf, and co-h2 conversion factor. *The Astrophysical Journal*, 680(1):246, 2008.

[104] LJ Tacconi, R Neri, SC Chapman, R Genzel, I Smail, RJ Ivison, F Bertoldi, A Blain, P Cox, T Greve, et al. High-resolution millimeter imaging of submillimeter galaxies. *The Astrophysical Journal*, 640(1):228, 2006.

[105] Yuki D Takahashi, PAR Ade, Denis Barkats, John O Battle, Evan M Bierman, JJ Bock, H Cynthia Chiang, C Darren Dowell, Lionel Duband, Eric F Hivon, et al. Characterization of the bicep telescope for high-precision cosmic microwave background polarimetry. *The Astrophysical Journal*, 711(2):1141, 2010.

[106] Jan Alexander Tauber, Nazzareno Mandolesi, J-L Puget, T Banos, Marco Bersanelli, François R Bouchet, Reginald Christopher Butler, J Charra, G Crone, J Dodsworth, et al. Planck pre-launch status: The planck mission. *Astronomy & Astrophysics*, 520:A1–1, 2010.

[107] Klaus D Timmerhaus and Richard P Reed. *Cryogenic engineering*. Springer, 2007.

[108] Takayuki Tomaru, Masashi Hazumi, Adrian T Lee, Peter Ade, Kam Arnold, Darcy Barron, Julian Borrill, Scott Chapman, Yuji Chinone, Matt Dobbs, et al. The polarbear-2 experiment. In *SPIE Astronomical Telescopes+ Instrumentation*, pages 84521H–84521H. International Society for Optics and Photonics, 2012.

[109] Ryan F Trainor and Charles C Steidel. The halo masses and galaxy environments of hyperluminous qsos at z 2.7 in the keck baryonic structure survey. *The Astrophysical Journal*, 752(1):39, 2012.

[110] Kim-Vy H Tran, Casey Papovich, Amélie Saintonge, Mark Brodwin, James S Dunlop, Duncan Farrah, Keely D Finkelstein, Steven L Finkelstein, Jennifer Lotz, Ross J McLure, et al. Reversal of fortune: Confirmation of an increasing star formation–density relation in a cluster at z= 1.62. *The Astrophysical Journal Letters*, 719(2):L126, 2010.

[111] JD Vieira, TM Crawford, ER Switzer, PAR Ade, KA Aird, MLN Ashby, BA Benson, LE Bleem, M Brodwin, JE Carlstrom, et al. Extragalactic millimeter-wave sources in south pole telescope survey data: source counts, catalog, and statistics for an 87 square-degree field. *The Astrophysical Journal*, 719(1):763, 2010.

[112] JD Vieira, DP Marrone, SC Chapman, C De Breuck, YD Hezaveh, A Weiβ, JE Aguirre, KA Aird, M Aravena, MLN Ashby, et al. Dusty starburst galaxies in

the early universe as revealed by gravitational lensing. *Nature*, 495(7441):344–347, 2013.

[113] Axel von Starck, Alfred Mühlbauer, and Carl Kramer. *Handbook of thermoprocessing technologies: fundamentals, processes, components, safety*. Vulkan-Verlag GmbH, 2005.

[114] Fabian Walter, Axel Weiss, Dennis Downes, Roberto Decarli, and Christian Henkel. A survey of atomic carbon at high redshift. *The Astrophysical Journal*, 730(1):18, 2011.

[115] JL Wardlow, Ian Smail, KEK Coppin, DM Alexander, WN Brandt, ALR Danielson, B Luo, AM Swinbank, F Walter, A Weiß, et al. The laboca survey of the extended chandra deep field-south: a photometric redshift survey of submillimetre galaxies. *Monthly Notices of the Royal Astronomical Society*, 415(2):1479–1508, 2011.

[116] Tony Wong and Leo Blitz. The relationship between gas content and star formation in molecule-rich spiral galaxies. *The Astrophysical Journal*, 569(1):157, 2002.

[117] Alwyn Wootten and A Richard Thompson. The atacama large millimeter/submillimeter array. *Proceedings of the IEEE*, 97(8):1463–1471, 2009.

[118] Jongsoo Yoon, John Clarke, JM Gildemeister, Adrian T Lee, MJ Myers, PL Richards, and JT Skidmore. Single superconducting quantum interference device multiplexer for arrays of low-temperature sensors. *Applied Physics Letters*, 78(3):371–373, 2001.

[119] Joshua D Younger, Giovanni G Fazio, Jia-Sheng Huang, Min S Yun, Grant W Wilson, Matthew LN Ashby, Mark A Gurwell, Alison B Peck, Glen R Petitpas, David J Wilner, et al. The aztec/sma interferometric imaging survey of submillimeter-selected high-redshift galaxies. *The Astrophysical Journal*, 704(1):803, 2009.

[120] Joshua D Younger, Giovanni G Fazio, David J Wilner, Matthew LN Ashby, Raymond Blundell, Mark A Gurwell, Jia-Sheng Huang, Daisuke Iono, Alison B Peck, Glen R Petitpas, et al. The physical scale of the far-infrared emission in the most luminous submillimeter galaxies. *The Astrophysical Journal*, 688(1):59, 2008.

[121] Joshua D Younger and Philip F Hopkins. A physical model for the origin of the diffuse cosmic infrared background and the opacity of the universe to very high energy γ-rays. *Monthly Notices of the Royal Astronomical Society*, 410(4):2180–2192, 2011.

[122] Jonas Zmuidzinas and HG LeDuc. Quasi-optical slot antenna sis mixers. *Microwave Theory and Techniques, IEEE Transactions on*, 40(9):1797–1804, 1992.